Mechanically Tunable RF/Microwave Filters: from a MEMS Perspective

by

Dong Yan

A thesis
presented to the University of Waterloo
in fulfillment of the
thesis requirement for the degree of
Doctor of Philosophy
in
Electrical and Computer Engineering

Waterloo, Ontario, Canada 2007

I hereby declare that I am the sole author of this thesis.

I understand that this thesis may be made available to other institutions or individuals for the purpose of scholarly research.

Dong Yan

Abstract

RF/microwave tunable filters are widely employed in radar systems, measurement instruments, and communication systems. By using tunable filters, the frequency bandwidth is utilized effectively and the system cost and complexity is reduced. In the literature, various tuning techniques have been developed to construct tunable filters. Mechanical tuning, magnetic tuning, and electrical tuning are the most common. In terms of quality factor, power handling capability, and linearity, mechanical tuning is superior to the other two tuning techniques. Unfortunately, due to their bulky size, heavy weight, and low tuning speed, mechanically tunable filters have limited applications. MicroElectroMechanical Systems (MEMS) technology has the potential to produce highly miniaturized tunable filters; however, most of the MEMS tunable filters reported so far have a relatively low quality factor. The objective of the research described in this thesis is to investigate the feasibility of using MEMS technology to develop tunable filters with a high quality factor. The integration of MEMS tuning elements with a wide range of filter configurations is explored, from micromachined filters to traditional dielectric resonator filters, from planar filters to cavity filters. Both hybrid integration and monolithic integration approaches are carried out.

To achieve tunability, MEMS tuning elements are embedded within RF and microwave filters. Tuning is accomplished by disturbing the electromagnetic fields of resonators with nearby MEMS tuning elements, which in turn change the resonant frequency of the resonators. First, the proposed tuning concept is experimentally demonstrated by integrating a surface micromachined planar filter with MEMS thermal actuators as the tuning elements. Then, a novel micromachined ridge waveguide filter embedded with similar MEMS tuning elements is proposed and constructed by using the EFAB$^{\text{TM}}$ micromachining technique. A power handling analysis is performed for the newly devised 3D micromachined filter, and potential failure mechanisms such as air breakdown are identified.

For the first time, a tunable dielectric resonator bandpass filter, incorporating vertical long-throw MEMS thermal actuators as tuning elements, is developed to achieve a wide tuning range, high quality factor, and large power handling capability. Several prototype tunable filter units are fabricated and tested. The experimental results reveal that the tunable filters maintain a relatively high quality factor value over a wide tuning range.

In addition to the hybrid integration approach, a monolithic integration approach is investigated. A novel surface micromachining process is developed to allow monolithic integration of MEMS tuning elements into micromachined filters. Due to a stress mismatch, MEMS actuators fabricated by this process obtain a vertical deflection of several hundred microns, resulting in a wide tuning range.

Various latching mechanisms are created, based on the micromachining processes that are used to fabricate the MEMS tuning elements. These out-of-plane latching mechanisms with multi-stable states have the potential to be adopted not only for tunable filter applications but also for switches and phase shifters.

Acknowledgements

It has been an enjoyable journey over my cherished years at the University of Waterloo. There are many people I want to thank for their help and support not only in my professional development, but also in my personal development. I would like to deeply thank my advisor, Dr. Raafat Mansour, for all he has done for me. If it wasn't for his rich knowledge, close guidance and endless support, I would never have finished. I would also like to thank my examination committee members: Dr. Pierre Blondy, Dr. Jan Paul Huissoon, Dr. Amir Khajepour, Dr. Safieddin Safavi-Naeini, and Dr. Siva Sivoththaman, for reviewing my thesis and providing valuable feedbacks and suggestions. I am also appreciative of the comments from Dr. Patricia M. Nieva during my research seminar.

It was such a fortune for me to be a member of the Centre for Integrated RF Engineering (CIRFE) group, a unique research group has attracted many talents. Many thanks shall be paid to Bill Jolley for teaching me how to think as a practical engineer and many tricks on device assembly. He always made me feel working in the lab is as enjoyable as playing soccer on columbia ice field. I am also indebted to Roger Grant for his valuable suggestions on process development and great training on operating cleanroom equipment. I would like to thank Louise Green for helping me to track down my advisor and taking care of all the paper work. In addition, her beautiful smile can really calm me down during MTT crisis. There are many wonderful, multi-talented grad students who have become my friends during my grad study. Their kindness and support have contributed a great part to my grad student life.

I would like to acknowledge the essential financial supports for my research project from Natural Sciences and Engineering Research Council of Canada (NSERC) and COM DEV International Ltd. Without their continuous support, this project would not have been possible.

It would not be a completed acknowledgement without saying thank you to my family. I want to express my deepest appreciation to my parents and my sister. Their support, love and encouragement made all of this possible.

Contents

List of Tables

List of Figures

Chapter 1

Introduction

1.1 Motivation

The continuing demands for highly portable, more reliable, superior power efficient, and above all, low cost wireless systems require that future wireless devices (such as cell phones and PDAs) must be compatible with different communication protocols and capable of operating over a wide frequency range. In addition, as wireless devices become more and more compact, the development of inexpensive and miniaturized tunable filters with a great performance is crucial.

Bandpass and bandstop filters are key components in many communication systems, either as band select or image-reject units. For the applications of multi-band receivers, filter banks are relied on to execute the filter requirements for all the receiving bands due to the limited coverage of a single fixed filter. By replacing filter banks with a low-loss tunable bandpass filter, the complexity of the overall system is significantly reduced and the reliability is substantially increased due to fewer components. In today's wireless communication systems, the majority of tunable filters are realized by varactor diodes or by ferromagnetic materials. Due to their nonlinearity, varactor diode tuned filters are prone to poor power handling; due to the ferromagnetic materials, filters' power consumption and physical size restrict wider applications of such tunable filters.

To maximize the data transfer, modern communication systems are forced to operate in higher frequencies. For example, most satellites currently operate in the 4-12 GHz range. To overcome the saturation problems, the next generation satellites will operate in the 20-30 GHz

range and in the 50-60 GHz range. At such high frequencies, traditional filter techniques will be abandoned due to fabrication limitations, and low quality factors, which will considerably effect the performance of filters.

MicroElectroMechanical System (MEMS) technology has the potential to provide a major impact on existing communication systems through reducing size, cost, weight and power dissipation. With the use of MEMS fabrication techniques, hundreds of filters can be batch-produced on the same wafer, and simultaneously, the filters and the tuning elements can be manufactured. Therefore, no post assembly process is needed. Furthermore, the filters can be tuned electronically instead of expensive manually tuning. Latching mechanisms will be featured with these tuning elements to secure the tuning position and the performance of the tuned filter.

1.2 Objectives

The purpose of this thesis is to investigate the feasibility of utilizing MEMS technology to design, fabricate, and analyze microwave and millimeter-wave miniaturized tunable filters with high quality factor. This research topic is divided into four tasks.

- **Investigation of using MEMS for fine tuning of filters:** Various micromachining techniques, including surface micromachining and bulk micromachining, are assessed for manufacturing miniaturized tunable filters. The development of techniques to fine tune micromachined filters by employing MEMS actuators as embedded tuning elements is also explored.

- **Application of MEMS actuators as tuning elements for high quality factor tunable bandpass filters:** A tunable dielectric resonator coupled bandpass filter, embedded with MEMS tuning elements, is studied. A traditional thermal actuator with large out-of-plane deflection that is used to power MEMS tuning elements is improved. Issues such as the power handling capability and loss mechanisms are discussed.

- **Monolithic integration of MEMS tuning elements with tunable bandstop filters:** The feasibility of tunable bandstop filter that is monolithically integrated with

MEMS tuning elements is examined. For such an integration, a unique surface micromachining process that is favorable to RF applications is created.

- **Development of multi-stable latching mechanisms for tunable filters:** Various micromachined multi-stable latching mechanisms are proposed. To obtain a wide tuning range for tunable filters, the latching mechanisms require a large travel range. With the aid of DC control signals, it is possible to switch between the different stable positions of these mechanisms.

1.3 Thesis Outline

Following the motivation and objectives outlined in Chapter 1, Chapter 2 presents an overview of the available technologies to realize tunable bandpass and bandstop filters, with a focus on MEMS technology. Furthermore, various micromachined latching mechanisms are addressed. In Chapter 3, two types of filters that are amenable to MEMS fabrication techniques are investigated. Chapter 4 is dedicated to a tunable bandpass filter with a high quality factor. The development of a dielectric tunable bandpass filter embedded with MEMS tuning elements is carried out. In Chapter 5, a solution to monolithically integrate a bandstop filter with MEMS tuning elements is provided; and a novel tri-layer (metal-dielectric-metal) MEMS process is introduced. Chapter 6 is devoted to the development of micromachined latching mechanisms that are suitable for out-of-plane structures. In Chapter 7, the research contributions of this thesis and suggestions for future work are provided.

Chapter 2

Literature Survey

2.1 Tunable Bandpass Filter

Tunable bandpass filters are a critical component in modern radar and communication systems, especially in multiband communication systems such as the Joint Tactical Radio System (JTRS) [29]. By employing tunable bandpass filters, the complexity and cost are mitigated, and the overall performance is improved. Over the last few decades, tunable bandpass filters have been realized by many technologies. A comprehensive review on this subject up to the early nineties can be found in the literature [30]. With the development of micromachining techniques, tunable bandpass filters based on MEMS technology have attracted a great deal of interest during the last 20 years. Since the number of applicable technologies is extremely large, only the most important innovations are included here.

Based on their tuning mechanisms, most tunable bandpass filters presented in the literature fall into three basic types: mechanical tuning, electronical tuning, or magnetic tuning. Tunable bandpass filters, based on MEMS technology, are categorized as a fourth category due not only to their multi-discipline tuning mechanism, but also to their potential use in the next generation multiband communication systems.

2.1.1 MEMS Tuning Method

Various MEMS components, such as MEMS contact switches, MEMS capacitive switches, and MEMS varactors, have been implemented in tunable bandpass filters. The most straight forward

way to design tunable bandpass filters by employing MEMS technology is to replace traditional multiport switches with their MEMS counterparts in a switched filter bank [1, 31]. This type of architecture is easily scalable to broader the tuning ranges and the only limitations are the bandwidth of the MEMS switches and the physical space. Fig. 2-1 exhibits a three-channel filter bank with two SP3T MEMS switches. Each channel has a fixed three-pole end-coupled bandpass filter. The three fixed bandpass filters are connected to the input and output ports through SP3T MEMS switches. The test results show a tuning range of 17.7% and an insertion loss from 1.7 dB to 2 dB.

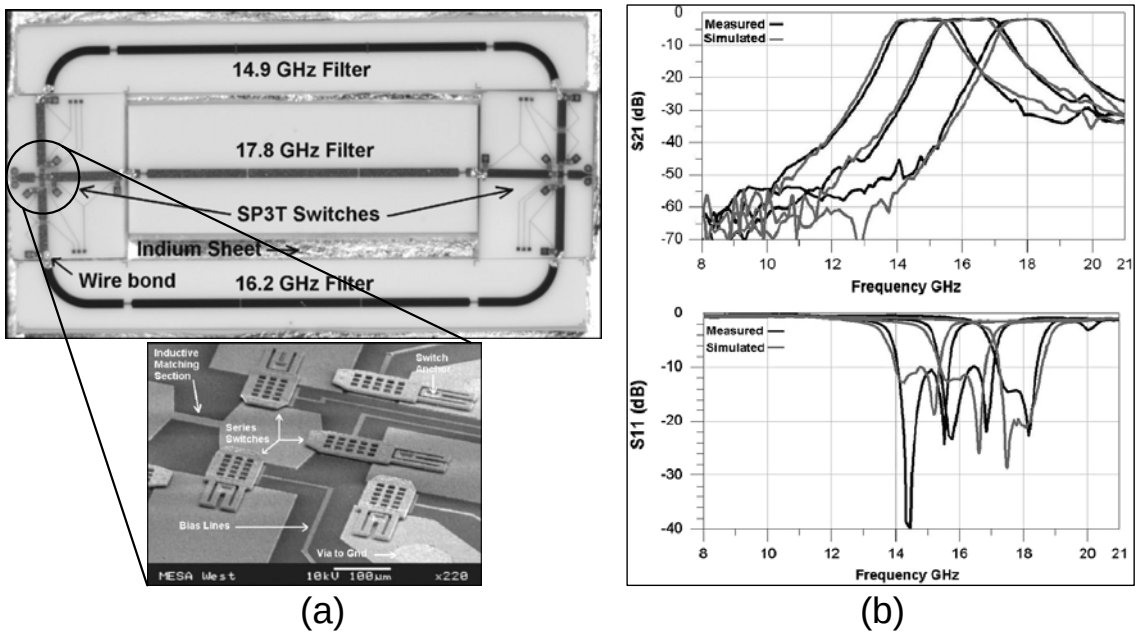

Figure 2-1: (a) The layout of the switched filter bank, and (b) the measured results of the switched filter bank [1].

The design procedure for a switched filter bank is fairly easy, since each channel's filter can be designed individually. However, the switched filter bank topology is not suitable for low frequency applications due to space limitation. Besides the use of a filter bank to achieve a tunable filter function, a single bandpass filter can also be tuned by directly adjusting the physical size of the resonators [2, 32] or changing the capacitive loading of the resonators [33, 34].

Fig. 2-2 depicts a 2-bit tunable bandpass filter by using MEMS DC contact switches [2].

The filter consists of two half-wavelength microstrip resonators, fabricated on a high resistivity silicon substrate. Each resonator connects two capacitive loads, the rectangular metal boxes in Fig. 2-2 (a), by MEMS switches. When DC bias voltages are applied, the MEMS switches close the connection between the resonator and capacitive loads. Therefore, the resonant frequency is shifted due to the extra capacitive loading. A frequency range from 12.2 GHz to 15.07 GHz has been covered by four discrete tuning states with an insertion loss better than 3 dB for all the states.

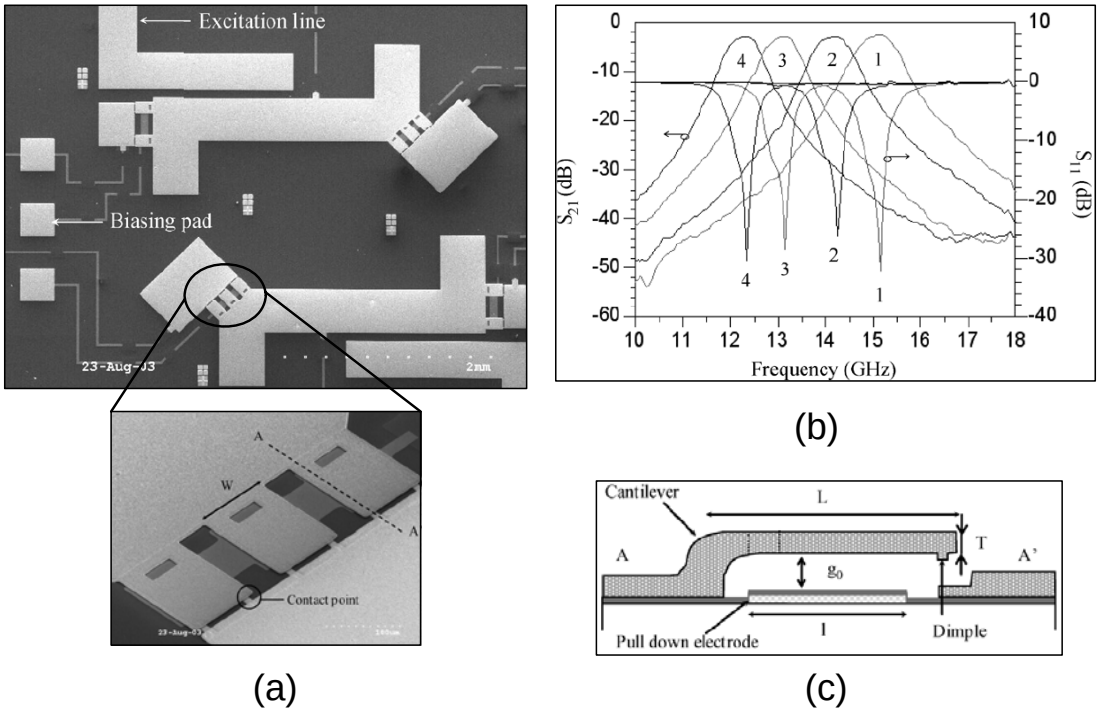

Figure 2-2: (a) SEM of the 2-bit tunable bandpass filter with DC contact switches, (b) the measured results of the four different states, and (c) a cross section of the MEMS switch [2].

Besides MEMS DC contact switches, MEMS capacitive switches are also applied to realize a tunable bandpass filter [32, 34, 35]. Instead of a metal to metal contact, a dielectric layer is deposited between the cantilever and the bottom electrode. The fatigue issues associated with DC contact switches are eliminated by using capacitive switches. However, for capacitive switches, dielectric charging is one of the intrinsic problems that requires further work since the charging can increase the DC bias voltage and cause stiction problems for the moving parts.

Electrostatic actuation is very popular in tunable bandpass filters with embedded MEMS switches. This is due to a low power consumption and well characterized behavior. However, for high power applications, MEMS switches, based on thermal actuation, are preferred. Thermal actuators can generate enough force to move the large metal contact pads that are usually required for high power applications. A tunable bandpass filter with thermally actuated MEMS relays has been reported for a power handling capability as high as 25W [36].

Although tunable bandpass filters with MEMS switches can achieve a wide tuning range, the frequency tuning is not continuous. To increase the frequency resolution and to obtain a near-continuous frequency tuning, multi-bit varactors, constructed by MEMS capacitive switches, have been developed in [4, 3, 37]. Fig 2-3 illustrates a three-pole resonator coupled tunable bandpass filter [3]. Each coplanar-waveguide (CPW) resonator is loaded with a multi-bit varactor that consists of four pairs of MEMS switched capacitors. These MEMS switched capacitors are periodically placed along the CPW resonators. A circuit model and physical realization of a unit cell of mult-bit varactor is conveyed in Fig. 2-3 (b).

Fig. 2-4 signifies the measured insertion loss and return loss of a 12-18 GHz tunable filter for 16 states. The insertion loss varies from 5.5 dB to 8.2 dB across the whole tuning range and the return loss is better than 10 dB for all the states. Also, the experimental filter has also demonstrated an excellent linearity with the measured third order input intercept point (IIP_3) level better than 37 dBm for Δf >200KHz. However, the absolute bandwidth is increased as the centre frequency is increased due to the lack of tuning mechanisms for the couplings between the inner resonators and the input and output couplings. This is solved by employing tunable capacitors as coupling units between the resonators [4]. As shown in Fig. 2-5 (a), a 4-bit varactor is placed between two resonating units as coupling mechanisms. Then, the coupling value is tuned by changing the capacitance of the varactor. The same coupling mechanism has also been applied to the input and output coupling. The measured results in Fig. 2-6 indicate a tuning range from 885 MHz to 986 MHz with a constant bandwidth of 180 MHz. The insertion loss is changed from 6.6 dB to 7.3 dB over the entire tuning range. The relatively high insertion loss is attributed to the low quality factor of on-chip inductors. For applications where a high quality factor filter is required, multi-bit MEMS varactors, in conjunction with high temperature superconductor filters, can be used to solve the problem [38].

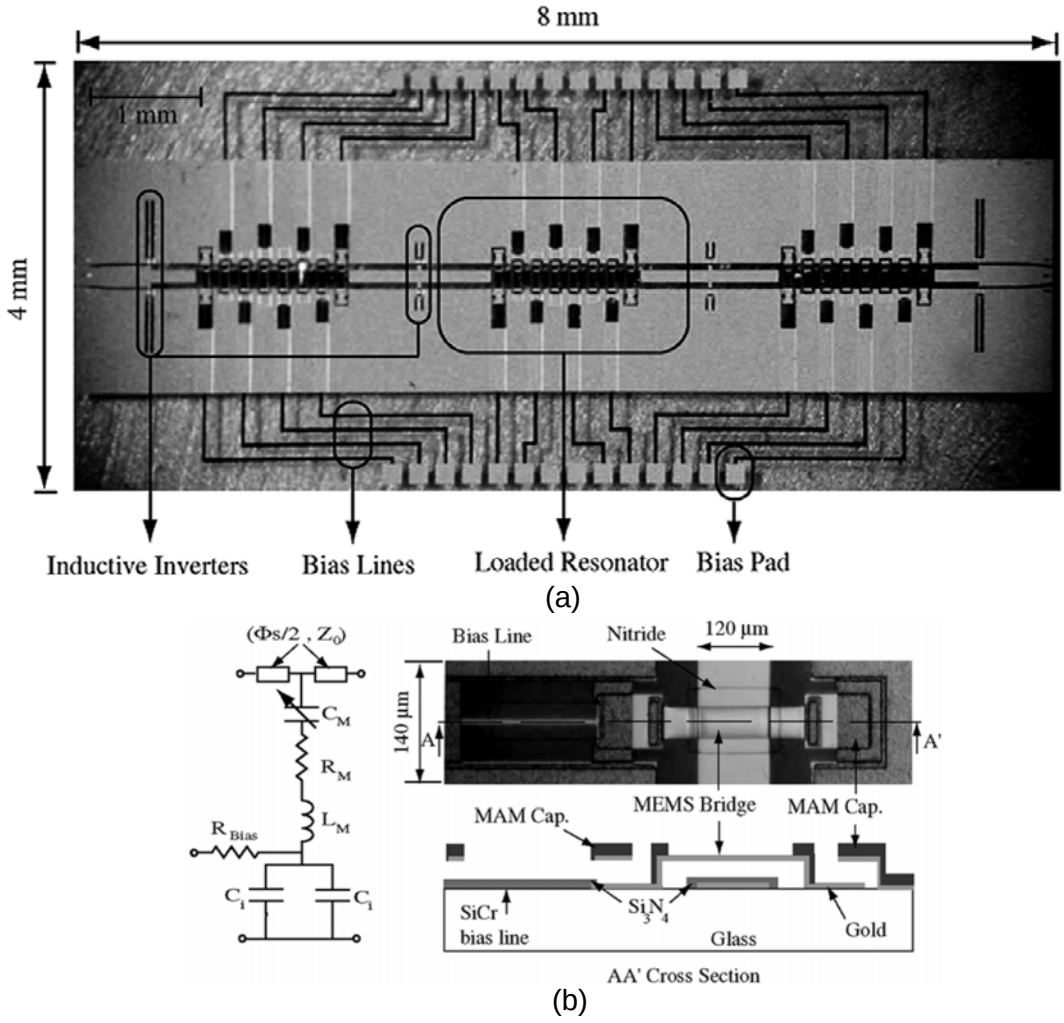

Figure 2-3: (a) The fabricated 12-18 GHz tunable bandpass filter on a glass substrate and (b) a circuit model and practical realization of a unit cell of a mult-bit varactor [3].

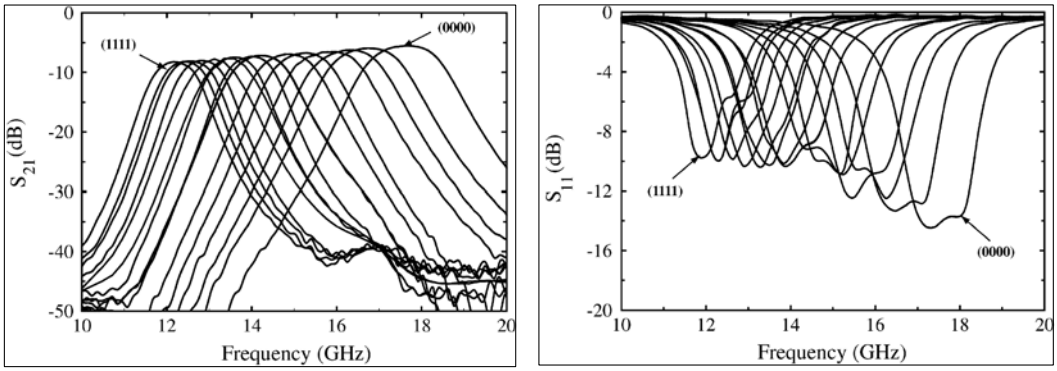

Figure 2-4: The measured results of the 12-18 GHz tunable filter [3]: (a) insertion loss and (b) return loss.

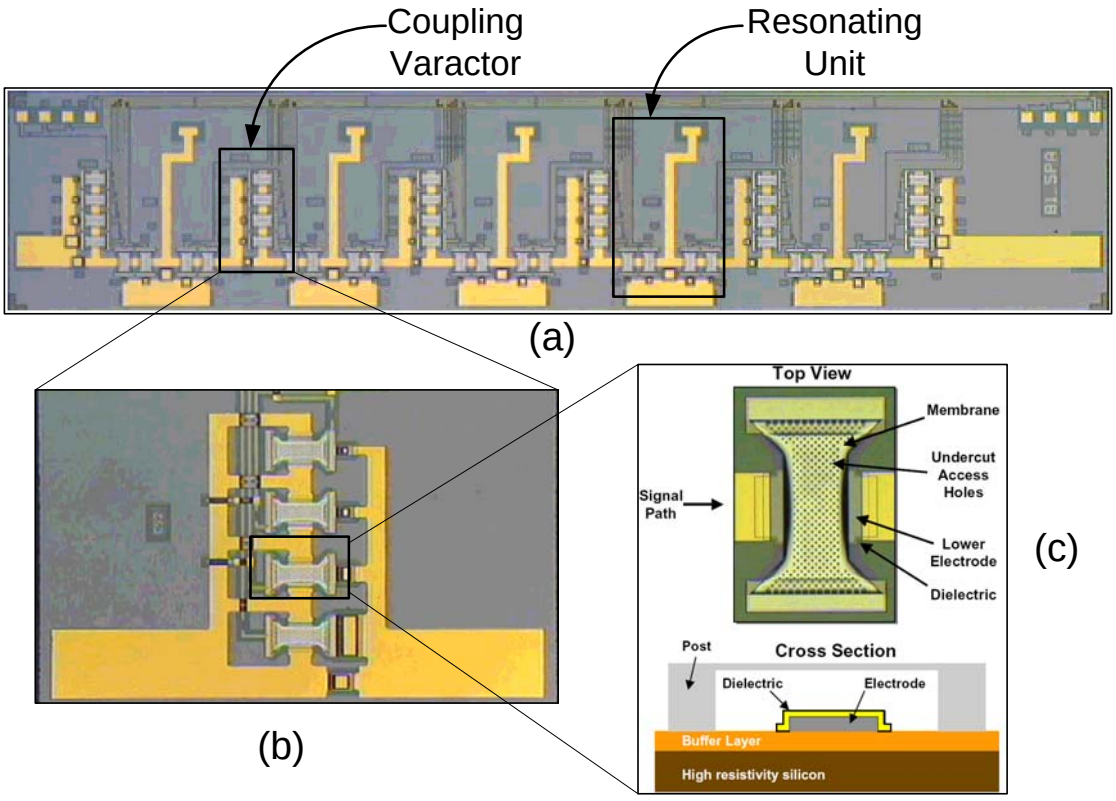

Figure 2-5: (a) The layout of the UHF five-pole tunable filter, (b) a multi-bit varactor with MEMS switches, and (c) views of the MEMS capacitive switch [4].

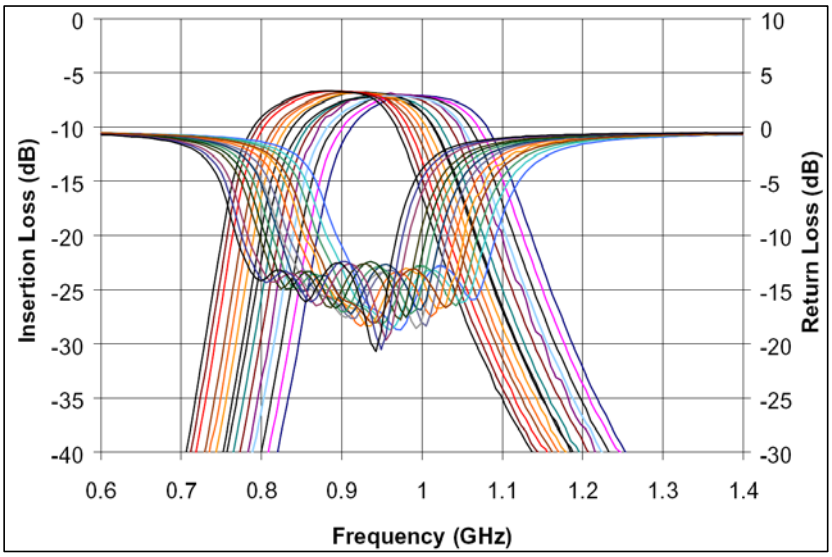

Figure 2-6: Measured results of the UHF five-pole tunable filter [4].

Tunable bandpass filters with embedded MEMS switches provide a wide tuning range. The frequency resolution is increased, but at the expense of increasing the number of MEMS components. A tunable bandpass filter with a large number of MEMS tuning elements can cause reliability issues, since a failure of any MEMS element results in the degradation of the overall filter performance. Consequently, MEMS analog varactors should be the optimal solution, when a wide tuning range is not a strict requirement. Fig. 2-7 demonstrates a two-pole tunable UHF filter where the tuning is achieved by using comb-drive MEMS analog varactors. The varactor maintains a quality factor greater than 100 from 225 MHz to 400 MHz with a capacitance from 1.4 to 11.9 pF. The filter can be continuously tuned over a range from 225 MHz to 400 MHz with an insertion loss that is better than 6.2 dB. Also, tunable bandpass filters based on MEMS analog varactors have also been demonstrated at K band [39] and V band [40]. In [39], a tuning range from 18.6 to 21.4 GHz has been achieved with an insertion loss better than 4.5 dB over this range. In [40], the tunable bandpass filter can be continuously tuned from 59 to 65.5 GHz with an insertion loss better than 3.5 dB.

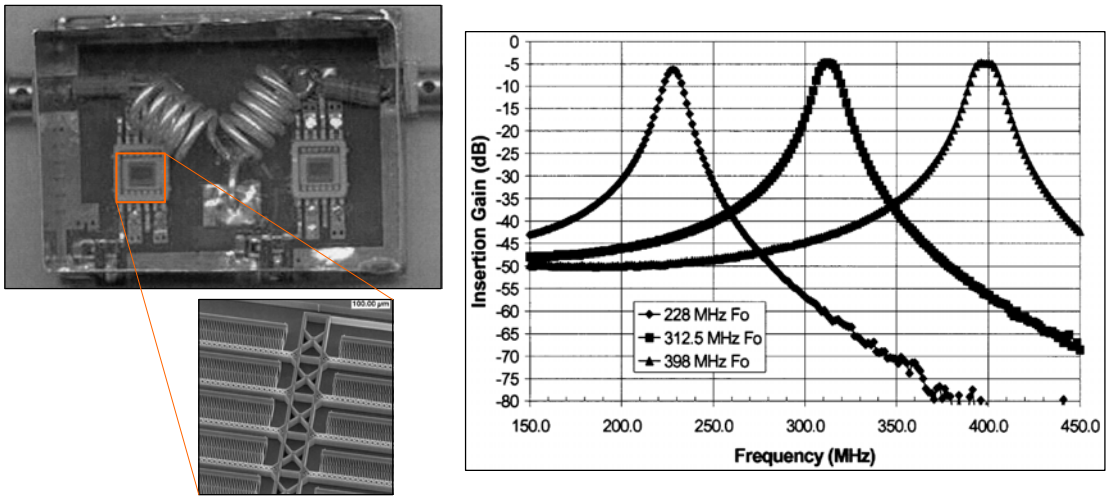

Figure 2-7: (a) The physical realization of a two-pole tunable UHF filter and (b) measured responses [5].

2.1.2 Electronical Tuning Method

Electrical tunable bandpass filters, realized by varactor diodes, offer a very fast tuning speed over a wide tuning range. They are compact in size and light in weight. When a reverse (negative) DC voltage is applied to a varactor diode, the variation of its capacitance alters the resonant frequency of the resonator that is connected to the varactor diode. Fig. 2-8 displays a typical varactor-tuned bandpass filter, implemented by combline resonators. The tuning mechanism of the filter is fairly simple and is readily adopted by different types of filters such as microstrip line [41], suspended strip line [42, 43], and finline waveguide structure [44]. A constant bandwidth with a substantial tuning range is possible by employing step-impedance microstrip lines [45, 46] or implementing special matching networks for the input and output couplings [41].

The key drawbacks of varactor-tuned bandpass filter are a relatively large insertion loss and a low power handling capability, which are attributed to the varactor didoes's low quality factor and nonlinearity, respectively. Virdee *et al.* has reported varactor tuned dielectric resonators that exhibit a much higher quality factor at the expense of a reduced tuning range [47, 48]. They are good candidates to construct a varactor-tuned dielectric resonator bandpass filter with

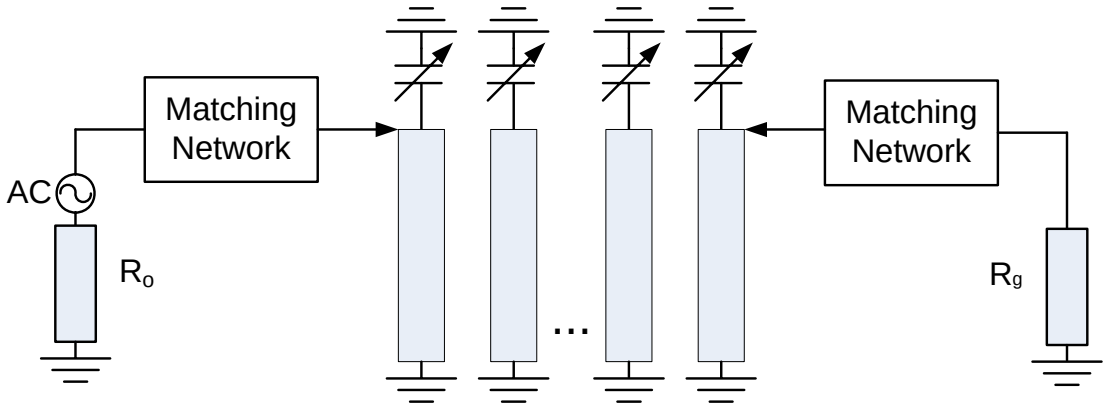

Figure 2-8: A schematic of a varactor-tuned combline filter.

a fast tuning speed and high quality factor.

Another solution to increase the insertion loss and power handling capability of varactor-tuned bandpass filters without a tuning range reduction is to replace varactor diodes with thin-film ferroelectric varactors such as Barium-Strontium-Titanate (BST) varactors. The capacitance of BST varactors can be varied by changing the dielectric constant of the ferroelectric material with the aid of an external DC bias voltage. BST varactors can be fabricated either in a parallel plate (metal-insulator-metal) fashion or an interdigitated configuration. Fig. 2-9 illustrates a typical interdigitated BST varactor and its characteristics [6].

Typically, tunable bandpass filters, based on the hybrid integration of BST varactors and planar filters, reach an insertion loss from 3 dB to 7 dB with a centre frequency from 0.2 GHz to 3 GHz [49, 50, 51]. The linearity characterization of the filter by Nath *et al.* reveals a third-order intercept point (IP3) of 41 dBm under the conventional two-tone intermodulation test [49]. Due to the compatibility of the fabrication process of BST varactors with a traditional semiconductor process, a monolithic integration of BST varactors with lumped element bandpass filter has also been demonstrated [52].

2.1.3 Mechanical Tuning Method

Although a compact size, light weight, and fast tuning speed have been the driving force for modern communication systems, mechanically tunable bandpass filters still attract attention

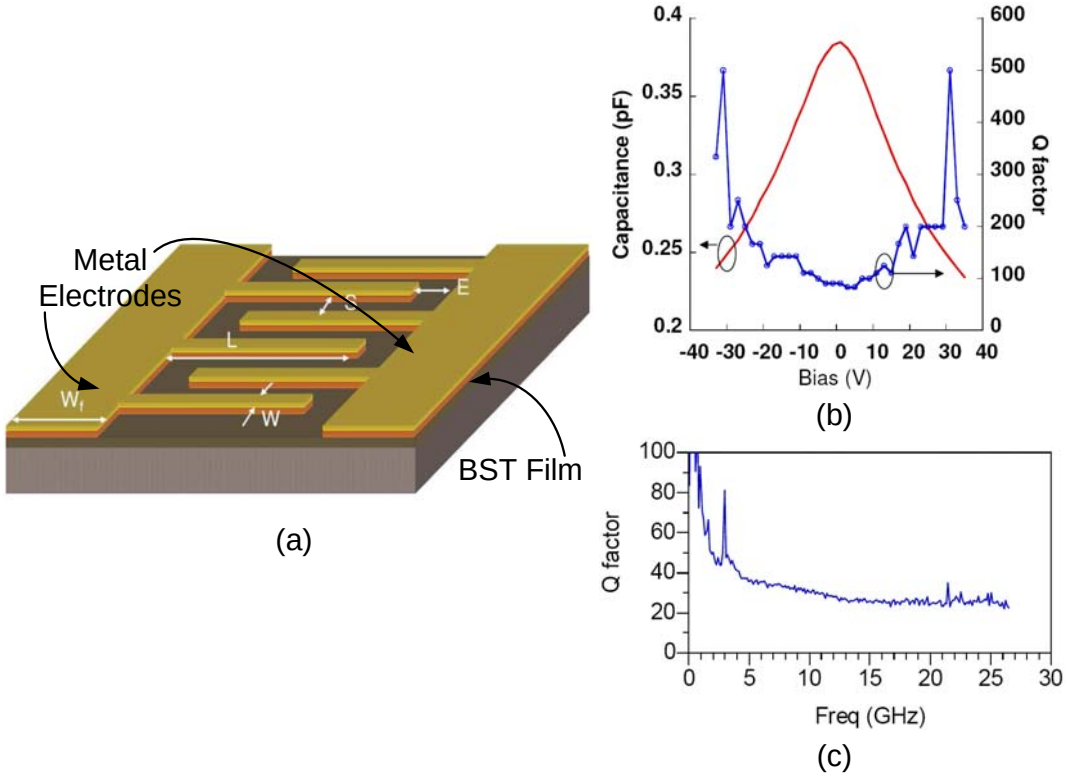

Figure 2-9: (a) A typical interdigitated BST varactor, (b) the measured C vs. V at 1 MHz, and (c) the measured Q factor vs. frequency [6].

due to their unbeatable power handling capability and high quality factor. Mechanically tunable bandpass filters have been realized in coaxial and waveguide configurations [30]. The tuning of such mechanically tunable bandpass filters is accomplished by human labors or electronic motors.

To further reduce the filter size without sacrificing too much of the quality factor, a tunable bandpass filter, loaded with dielectric resonators, has been developed [7, 53, 8]. Fig. 2-10 (a) illustrates a four-pole dielectric resonator loaded tunable bandpass filter. Two dielectric resonators, resonating at a hybrid (HEH_{11}) mode, are employed to construct the bandpass filter, and the other two dielectric resonators serve as tuning disks. By moving the tuning disk close to the hybrid mode resonators, the resonant frequency is reduced due to the extra loading effect of the dielectric tuning disks. The filter can be tuned continuously from 4.6 GHz to 4.8 GHz without significant changes in its return loss or bandwidth as shown in Fig. 2-10 (b). The insertion loss is varied between 0.85 dB and 1.15 dB, corresponding to the unloaded Q of 5200 and 4700, respectively over a 200-MHz tuning range. A more detailed analysis of the tuning properties of such type configuration can be found in [53].

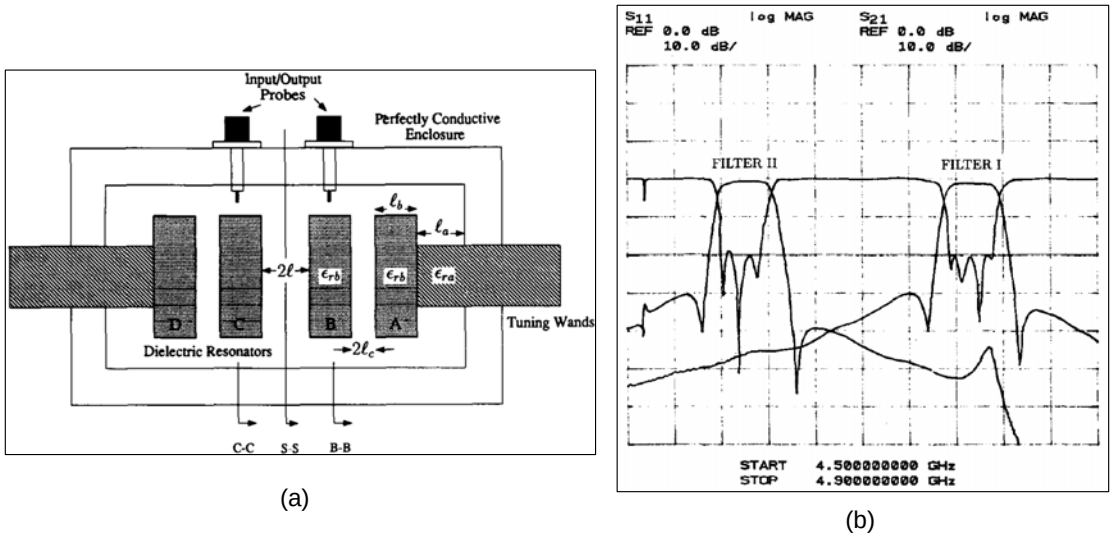

Figure 2-10: (a) The configuration of a four-pole tunable dielectric resonator loaded filter and (b) the measured results of the filter tuned at different centre frequencies [7].

The dielectric tunable bandpass filter presented by Zaki *et al.* [7] has displayed good tuning

properties in terms of the filter size, tuning range, and loss. However, the filter's tuning speed is very low due to the tuning screw-like configuration. Fig. 2-11 (a) is a schematic view of a tunable dielectric resonator with a tuning speed in the millisecond range [8]. The tunable dielectric resonator comprises three basic components: a dielectric resonator operating at the TE_{01} mode, a metal disk consisting of a number of radial-arranged quarter-wave slotline resonators, and piezoelectrically actuated switches for each slotline resonator. The tunability is achieved by controlling the intermodular coupling between the dielectric resonator and slotline resonators. As portrayed in Fig. 2-11 (b), when the switches are in the OFF state, each slotline resonator possesses a strong magnetic coupling with the dielectric resonator. This leads to an increase of the effective size of the resonator and results in a decrease of the resonant frequency of the TE_{01} mode. When the switch is in the ON state, the slotline becomes a half-wave resonator. Due to the sign change of the magnetic field in the middle of the slotline, the coupling between the slotline and the dielectric resonator is much weaker, and the resonant frequency of the the TE_{01} mode remains almost unchanged.

The test results reveal a tuning range of 5 MHz at approximately 2 GHz with a discrete frequency step of 0.25 MHz. This tunable dielectric resonator maintains an unloaded quality factor larger than 12000 over the entire tuning range. For a fast tuning speed, piezoelectric actuators are employed as switches to close the slotline resonators and post-switching oscillation decay within 1 ms, after the piezoelectric actuators are triggered.

Mechanical tuning methods have been implemented not only in cavity tunable filters, but also in planar tunable filters such as microstrip line filters [9], LTCC filters [54], and HTS filters [55]. One example of mechanically tuned planar bandpass filters is shown in Fig. 2-12 [9]. A dielectric perturber, which is attached to a piezoelectric actuator, is suspended above a microstrip bandpass filter. When voltage is applied to the piezoelectric actuator, it can move the perturber up or down along the Z axis. When the dielectric perturber is moved close to the filter, the dielectric constant of the substrate is effectively increased, which in turn, lowers the centre frequency of the filter.

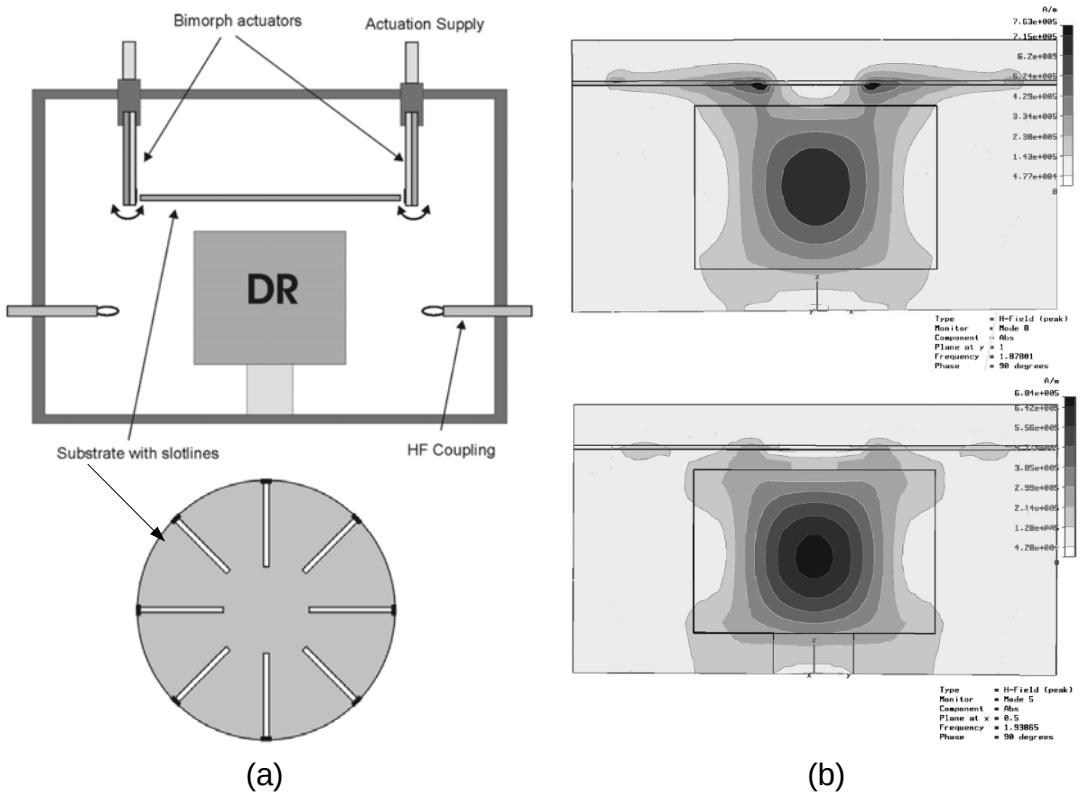

Figure 2-11: (a) A schematic view of the test setup for the discrete tuning of a dielectric resonator and (b) the axial magnetic field contours of the resonator for all the slots being in the open state (top) and the closed state (bottom) [8].

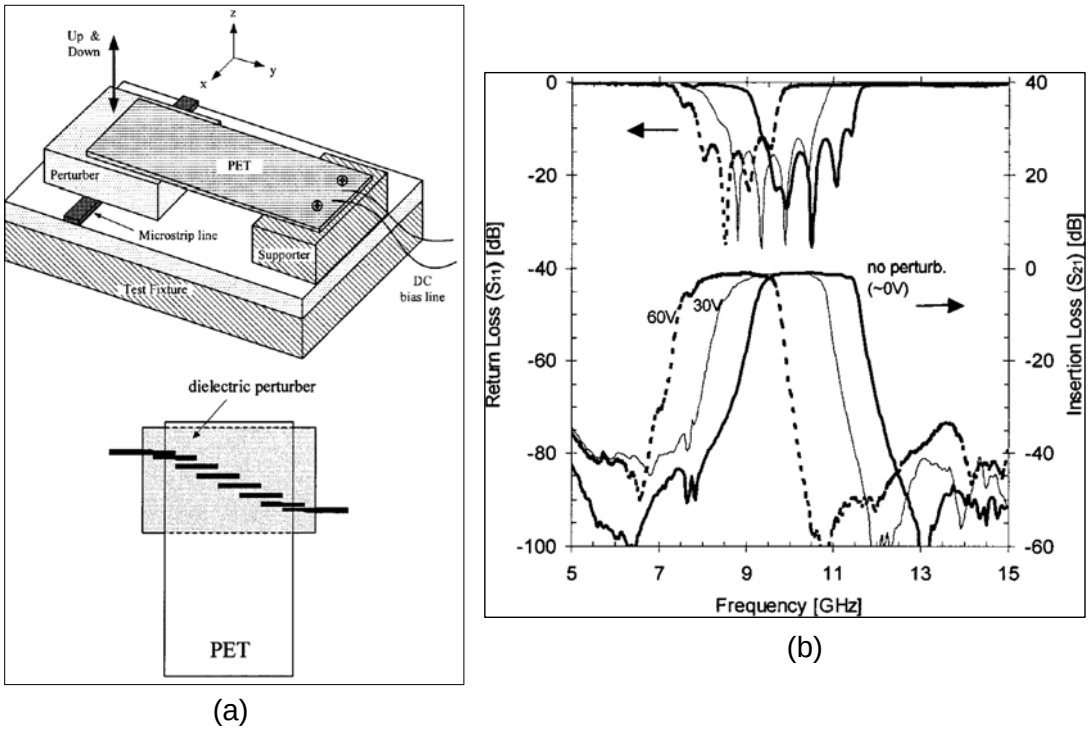

Figure 2-12: (a) A schematic view of the test setup for a mechanically tuned planar bandpass filter and (b) the measured results [9].

2.1.4 Magnetical Tuning Method

Magnetically tunable filters such as the YIG filter still play a dominant role in applications, where an ultra-wideband tuning range is required. Also, magnetically tunable filters are compact, and have a spurious free response and high selectivity [30]. However, magnetically tunable bandpass filters are usually associated with a large power consumption and low power handling capability.

Fig. 2-13 illustrates two configurations of magnetically tunable dielectric resonators in conjunction with ferrite materials [10]. The tunability can be realized by either the axially magnetized ferrite rod, in Fig. 2-13 (a), or the circumferentially magnetized ferrite disks in Fig. 2-13(b). Their physical realizations are shown in Fig. 2-13 (c) and (d), respectively. The measured results reveal a 20 MHz-tuning range and an unloaded quality factor better than 2500 for the filter, containing axially magnetized ferrite rod shown in Fig. 2-14 (a). A 28-MHz tuning range and an unloaded quality factor better than 3500 for the filter, containing the circumferentially magnetized ferrite disks. The currents required to achieve such tuning ranges are 2.5 A and 3 A, respectively. The tuning range can be increased by increasing the tuning power. It is feasible to construct filters with a wider tuning range and a higher Q factor at a higher frequency (around 6 GHz), since the ferrite materials have a better figure of merit around this frequency.

2.2 Tunable Bandstop Filter

Tunable bandstop filters are widely employed in wideband communication and radar systems to provide a deep rejection over a band of unwanted frequencies, and to introduce minimum disturbance in the remaining spectrum. Tunable bandstop filters are pivotal to reduce the interference from the crowded adjacent channels and to avoid cross talk between the transmitter and receiver [56, 57, 58]. In the literature, the tunability of tunable bandstop filters has been acquired by using various technologies such as semiconductors, ferromagnetic materials, and MEMS. In this section, tunable bandstop filters based on varactor diodes, ferromagnetic materials and MEMS components are compared, since the majority of tunable bandstop filters are realized by one of these methods.

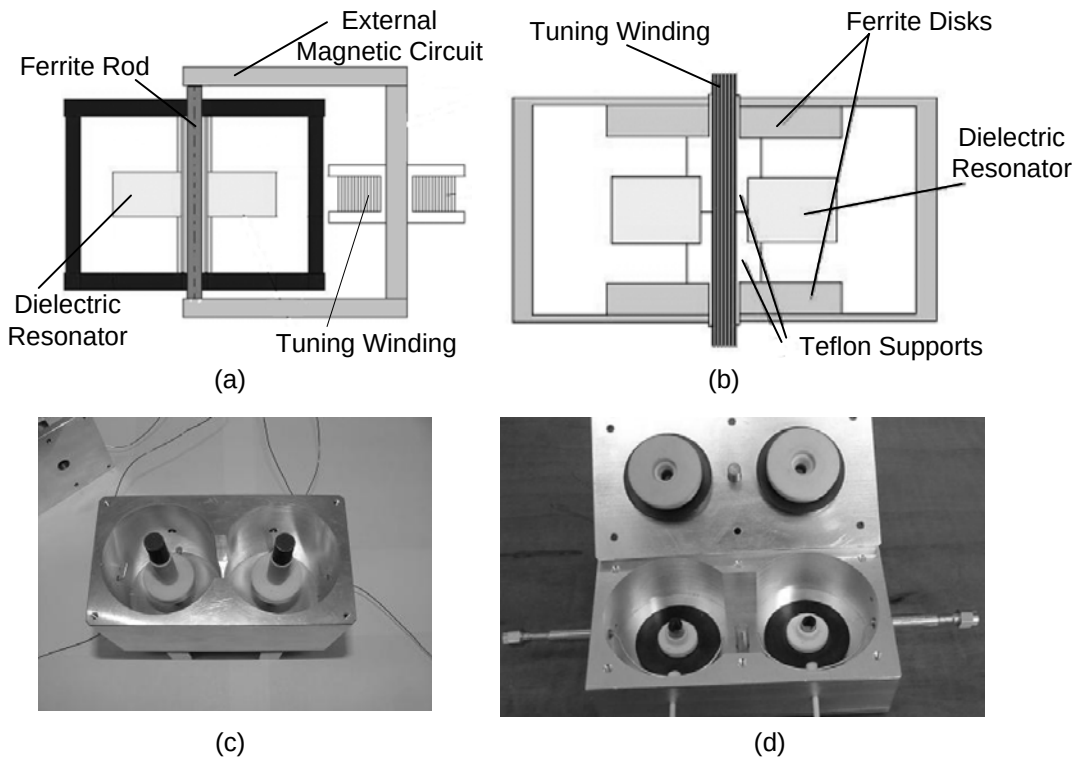

Figure 2-13: A schematic of a magnetically tunable dielectric resonator containing (a) axially and (b) circumferentially magnetized ferrite elements and their physical realization: (c) axially and (d) circumferentially [10].

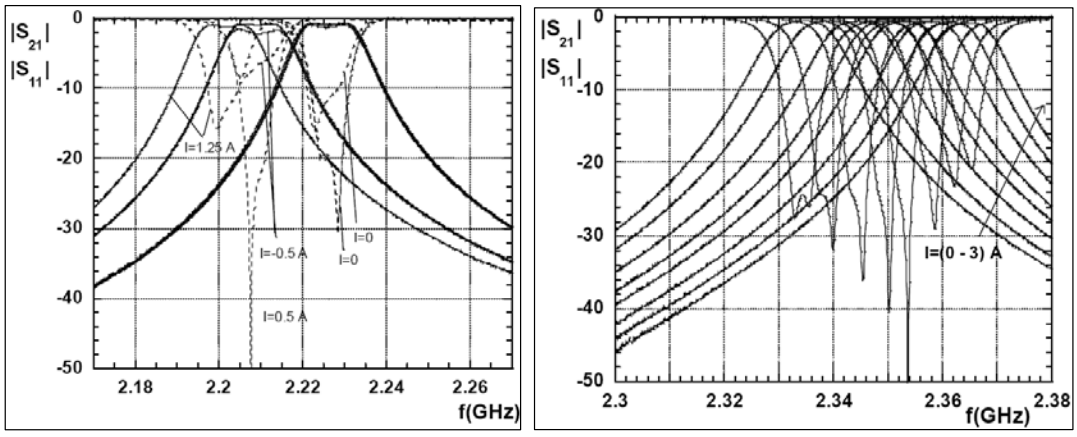

Figure 2-14: The test results for the filters containing (a) axially magnetized ferrite rods and (b) circumferentially ferrite disks [10].

2.2.1 Tunable Bandstop Filters by Ferromagnetic Materials

Two types of ferromagnetic materials have been extensively used to construct tunable bandstop filters: yttrium iron garnet (YIG)/gadolinium gallium garnet (GGG) on gallium arsenide (GaAs) substrates [59], and iron (Fe) film on GaAs substrates [60, 61]. Fig. 2-15 illustrates the configuration of a bandstop filter that is based on a YIG/GGG film on GaAs substrate [11]. After a 50-Ω microstrip line is first formed on the GaAs substrate, the YIG/GGG sample is laid on top of the microstrip line. When microwaves propagate along the microstrip line, part of the energy is coupled into the YIG/GGG layer. The peak absorption occurs when the carrier frequency coincides with the ferromagnetic resonance frequency. Since the ferromagnetic resonance frequency is a function of the magnetic field, the frequency where the peak absorption occurs can be tuned by varying the magnetic field in Fig. 2-15 (b).

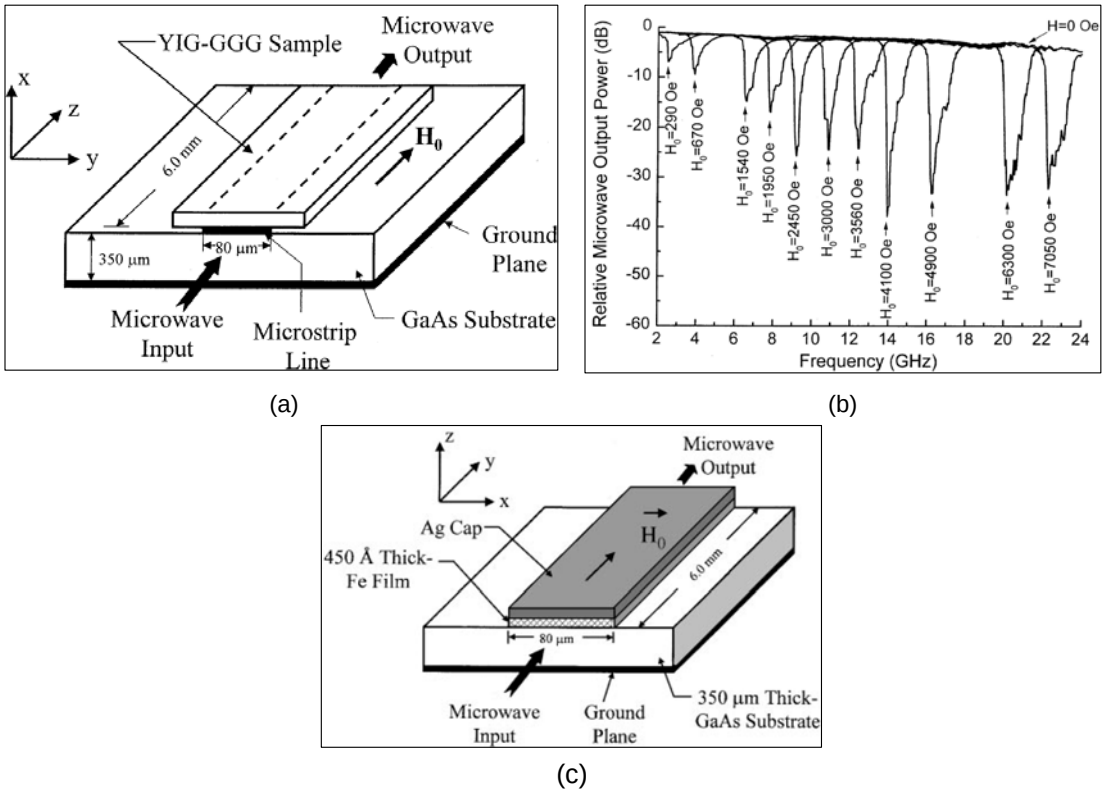

Figure 2-15: (a) A tunable bandstop filter with a YIG-GaAs flip-chip configuration, (b) the measured results with the magnetic field applied along the microstrip line, and (c) a tunable bandstop filter with a Fe-GaAs configuration [11].

Fe-film can also be employed to build tunable bandstop filters, since it has properties similar to those of YIG/GGG material [11, 61]. In addition, Fe-film can be directly grown by the molecular beam epitaxy on GaAs substrates, which produces ultimate microwave integrated circuits (Fig. 2-15 (c)). Furthermore, for a given frequency, Fe-film needs a weaker magnetic field than the YIG/GGG material.

Tunable bandstop filters that are devised from ferromagnetic materials demonstrate a superior tuning range with a deep rejection level. However, the tunability is obtained with the aid of external magnetic sources, which are bulky and consume a large amount of DC power. These two drawbacks limit the ferromagnetic tunable bandstop filters' applications for communication systems, where miniaturization and low power consumption are necessary.

2.2.2 Tunable Bandstop Filters by Active Components

There are two approaches to construct tunable bandstop filters in terms of semiconductor technology. One is to monolithically integrate passive and active components on the same substrate; and the other one is to post-assemble active components on the passive microwave circuits. The use of the monolithic microwave integrated circuit (MMIC) has been widely spread due to its size, mass and yield advantages over the hybrid microwave integrated circuit [62]. However, due to the poor quality factor of on-chip inductors, the MMIC approach is more suitable for low frequency applications [62, 63]. Q-enhancement techniques have been applied to improve the quality factor of on-chip inductors at the expense of increasing power consumption [64].

Fig. 2-16 depicts a typical hybrid integrated tunable bandstop filter, where tunable capacitors can be varactor diodes or p-i-n diodes. The tunability is obtained by changing the capacitance of the tunable capacitors, which results in changing the electrical length of the resonator stubs. The bandstop filter can be realized by various configurations such as microstrip line [65], suspended substrate stripline [66], and CPW line [58].

A microstrip line or CPW line with slots on the ground plane can also attain a bandstop filter response. The tunability of such type bandstop filters is possible by placing varactor diodes across the slots or by creating a short circuit with the use of switches [12, 13, 67].

Compared with ferromagnetic tuned bandstop filters, varactor diode-tuned bandstop filter

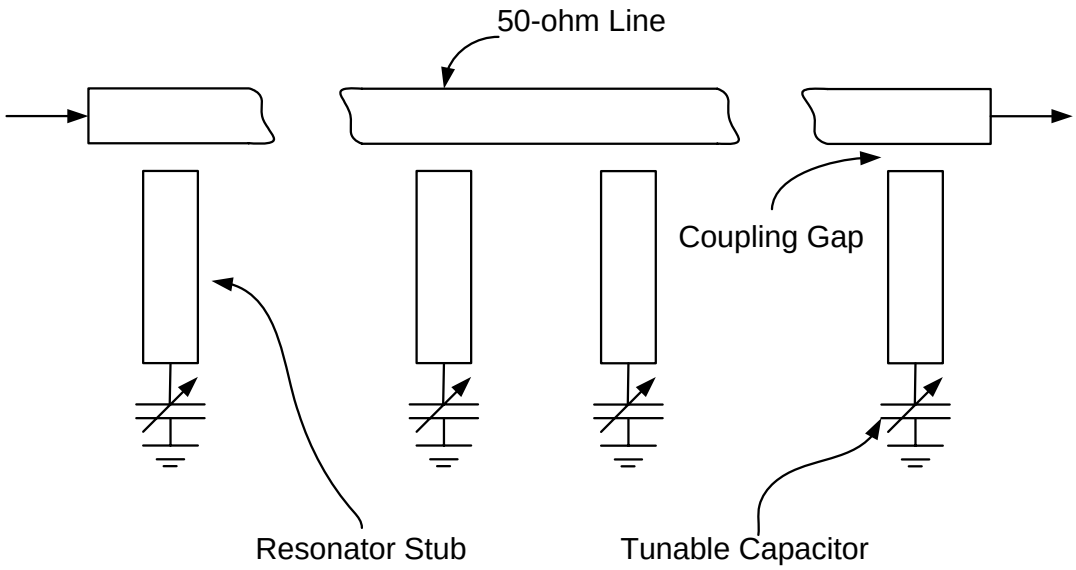

Figure 2-16: A schematic of a typical hybrid integrated tunable bandstop filter.

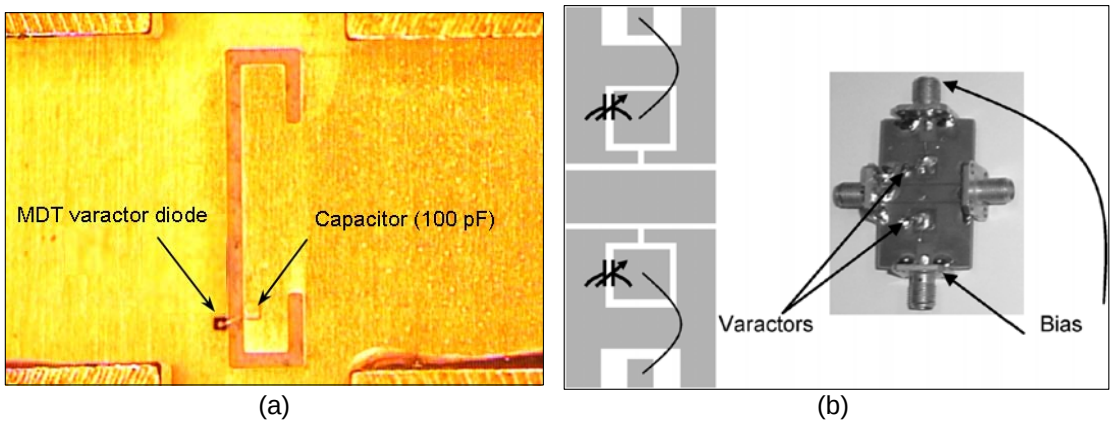

Figure 2-17: A slot type varactor tuned bandstop filter with (a) microstrip line configuration [12] and (b) CPW line configuration [13].

has a much smaller size, faster tuning speed, and consumes less power. Its tuning range mainly depends on the varactor diodes' tuning range (from a few hundreds of MHz to a few GHz). However, because semiconductor components' inherent transfer characteristics are nonlinear, they distort the incident signals, defeating the primary purpose of tunable bandstop filters [68].

2.2.3 Tunable Bandstop Filters by MEMS Components

The nonlinearity associated with varactor diodes can be solved by replacing them with MEMS components (tunable capacitors or switches). Moreover, MEMS components are amenable to microfabrication techniques, which makes the integration of microwave circuits feasible. Among the work that has been done on MEMS tunable bandstop filters, micromachined cantilever type structures and bridge type structures have been favorably selected as tuning components. They are easy to fabricate and can achieve a relatively wide tuning range, when they are used as switches [14, 69, 15].

Fig. 2-18 shows a tunable bandstop filter with MEMS bridges as the tuning elements [14]. This tunable bandstop filter has three resonating elements, and there are eight MEMS bridges between two resonating elements. When the DC bias voltage is applied between the signal line and the ground plane, the downward deformation of MEMS bridges changes the capacitance between the bridges and signal line, which changes the resonant frequency of the tunable bandstop filter. By varying the bias voltage from 0 V to 35 V, this bandstop filter can be tuned over a range from 19 GHz to 17.3 GHz.

A MEMS tunable bandstop filter with cantilever type structures as the tuning elements is illustrated in Fig. 2-19. It is fabricated on a high resistivity silicon substrate. The resonating units are U-shape cantilevers that consist of two materials. After release, the cantilevers bend upward due to the stress gradient between the two materials. The tunability of the bandstop filter is achieved by applying a voltage between the wafer back and the cantilever beams. Once they are pulled down to the substrate, the effective dielectric constant of the microstrip-like resonating units is increased, which in turn, increases the electrical length of the stubs. Therefore, the resonant frequency of the stubs is decreased. A tuning range of 5.5 GHz has been attained with an actuating voltage of less than 100 V.

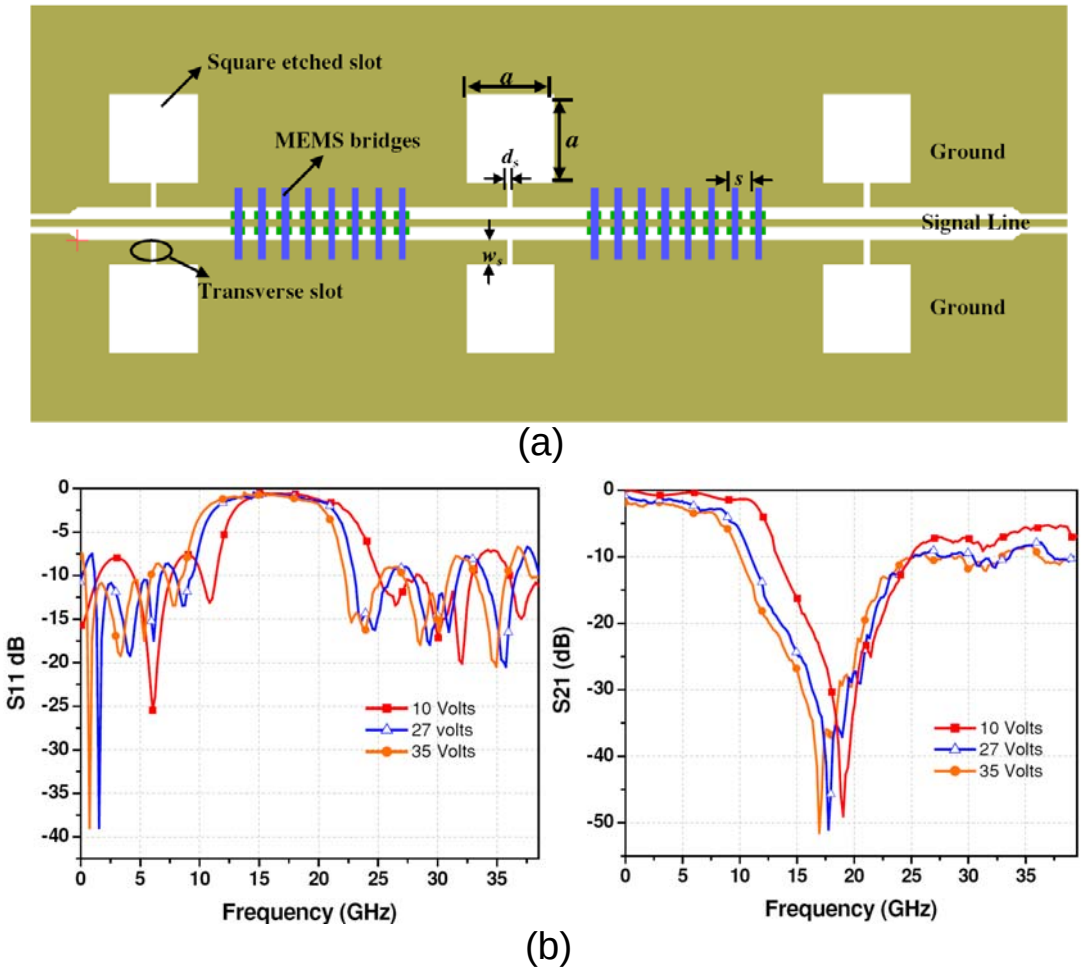

Figure 2-18: (a) A schematic of the tunable bandstop filter using MEMS bridges and (b) the measured results of the MEMS tunable bandstop filter [14].

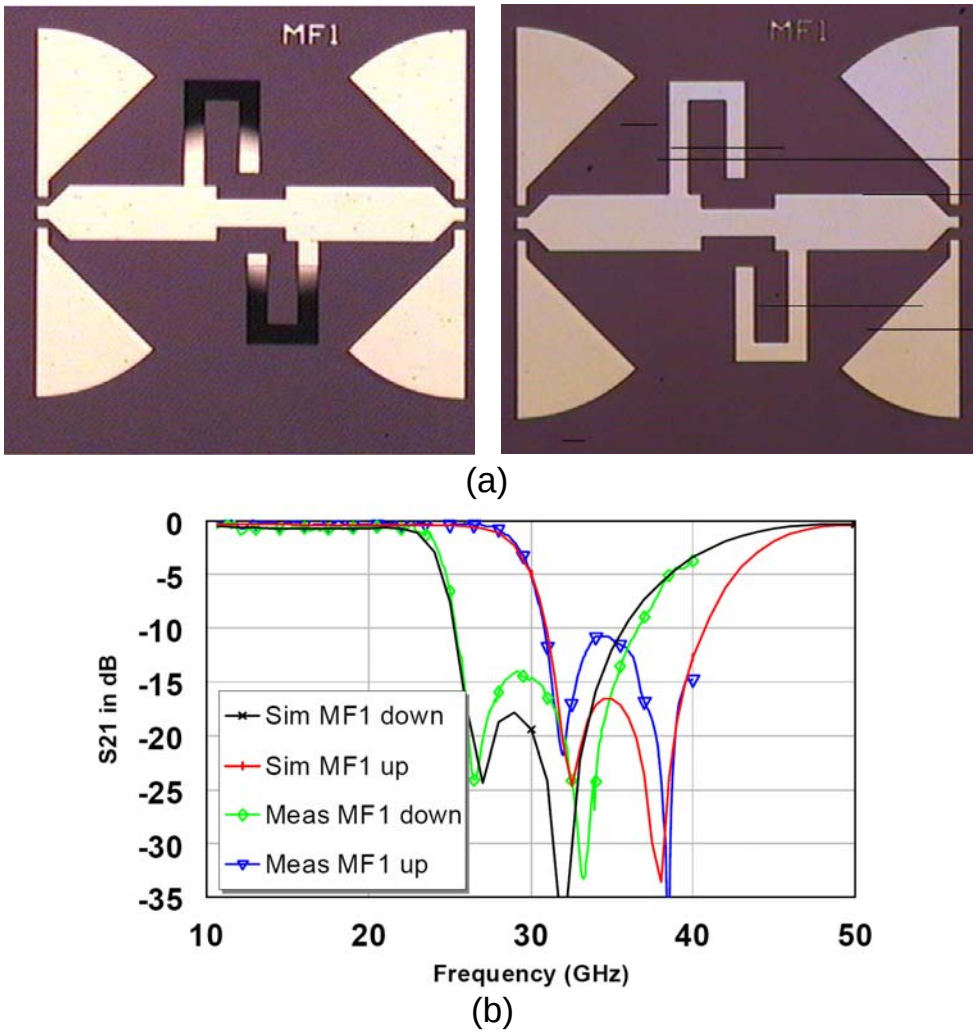

Figure 2-19: (a) Micrographs of a MEMS tunable bandstop filter with cantilevers at the up state (left) and down state (right) and (b) the simulation and measured results of the filter at two different states [15].

2.3 Micromachined Latching Mechanisms

A latching mechanism is a mechanism that retains its state in the absence of any external force. Unlike traditional latching mechanisms, micromachined latching mechanisms are popular in planar fashions due to the nature of the microfabrication techniques. In the literature, few micromachined latching mechanisms can be used to latch out-of-plane structures with the assist of an external magnetic field [26] or surface tension techniques [70, 27]. However, these mechanisms are not reversible, that is, once they are in the latching state, they cannot easily return to the original state. The research work found in the literature that will be presented in this section is restricted to micromachined latching mechanisms that can be switched between two or more stable states with the use of electrical control signals. Such mechanisms that reach their stable states with the aid of an external magnetical field or DC voltage are also summarized.

2.3.1 Compliant Bistable Mechanisms

A bistable mechanism can be explained by a classic "ball-on-a-hill" analogy, shown in Fig. 2-20. The mechanism has three different states: two stable states, A and C, and one unstable state, B, within its range of motion. The paramount advantage of a bistable mechanism is that no power input is required to maintain the mechanism at the stable states. Power input is needed only when the mechanism is switched from one stable state to the other. This particular behavior of the bistable mechanism is very attractive for MEMS applications, where power consumption must be minimized.

By imitating a traditional bistable light switch mechanism, a micromachined bistable mechanism that consists of springs and socket joints has been demonstrated [16]. It is fabricated by a conformal surface micromachining process. As shown in Fig. 2-21, two structure layers are employed to form the socket joint. The input force required to switch between the two stable states is independent to the current state. A serpentine spring is selected as the compression spring, as denoted in Fig. 2-21 (a). However, the type of spring has quite a large of footprint and might collapse on the substrate, causing a stiction problem. To solve this problem, flexible beams are substituted for the serpentine springs [71, 72].

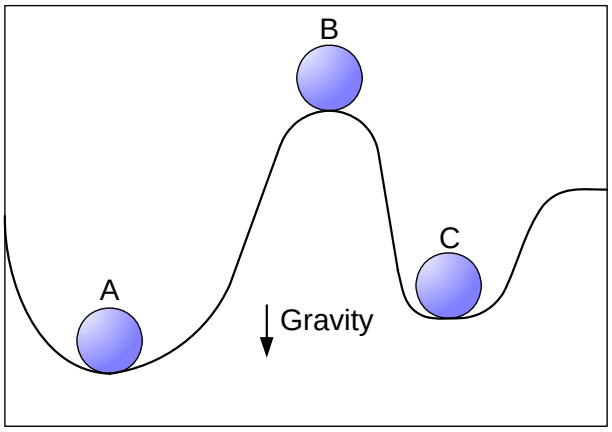

Figure 2-20: The "ball-on-a-hill" analogy of a bistable mechanism.

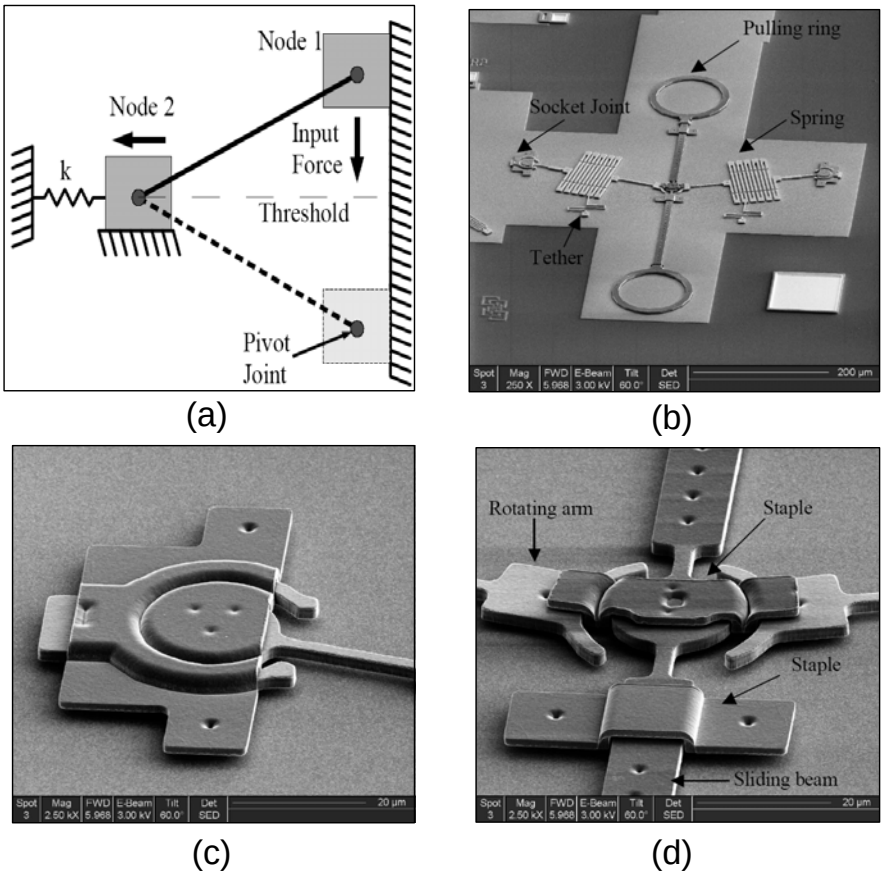

Figure 2-21: A toggle type bistable miromachined mechanism: (a) rigid body model, (b) fabricated device, (c) ball and socket joint, and (d) centre joint [16].

The micromachined bistable mechanism with the springs and socket joints requires more than one structure layer, increasing the complexity of the fabrication process; also, the alignment between the structure layers must be precisely controlled. In addition, this type of mechanism is subject to the problems of friction and wear due to the relative motion between the linkages and joints.

At the macro scale, a compliant bistable mechanism has many advantages over the bistable mechanism made of springs and joints [73]. By comparing them at the micro scale, a similar conclusion is drawn. To achieve motion and two stable states, two structure layers are needed to construct the micro joints and springs. However, in compliant mechanisms, the motion and two stable states are realized by one or more micromachined flexible beams, which require only one structure layer.

Fig. 2-22 illustrates the conversion of a rigid-body model to a fully-compliant model by using the pseudo-rigid-body modeling technique [17]. Here, the torsional springs are replaced by thin flexible beams, and the side spring is represented by clamped-clamped beam. Also, the stiffness of the clamped-clamped beam in the transverse direction is much more than that in the axial direction; therefore, the clamped-clamped beam also behaves like a slider. Fig. 2-23 depicts two stable states of a fully-compliant bistable mechanism, manufactured by surface micromachining techniques.

Due to the nature of surface micromachining techniques, the bistable mechanism shown in Fig. 2-23 has a very small output force (less than a few tens of micro newtons). The mechanism causes concerns for many applications such as switches and relays, where a high output force is desirable. Besides changing the geometry of the structure to increase the output force, increasing the thickness of the structure is another option. It has been demonstrated that a similar design with a few ten microns thick structure layer can achieve an output force of a few hundreds of micro newtons [74, 75]. Although fully-compliant mechanisms require only one structure layer, the fabrication tolerance can be very tight at certain locations such as where the thin flexible beams are. A small variation can lead to a much higher input force or even failure in function. This problem can be solved by replacing the thin flexible beams and rigid members with sinusoidal-wave-like beams at the expense of less output force [76]. In addition to increasing the output force and relaxing the fabrication tolerance, research efforts have also

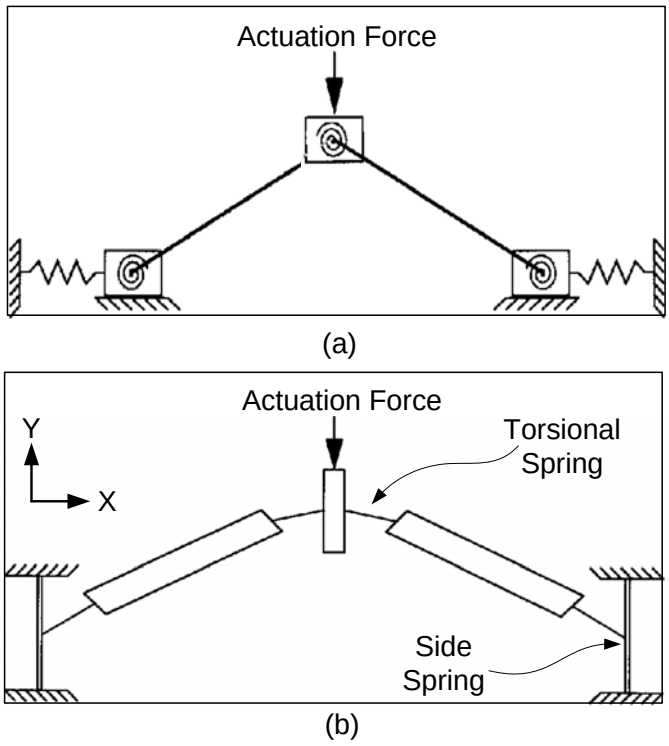

Figure 2-22: The conversion of a rigid-body model to a fully-compliant model [17].

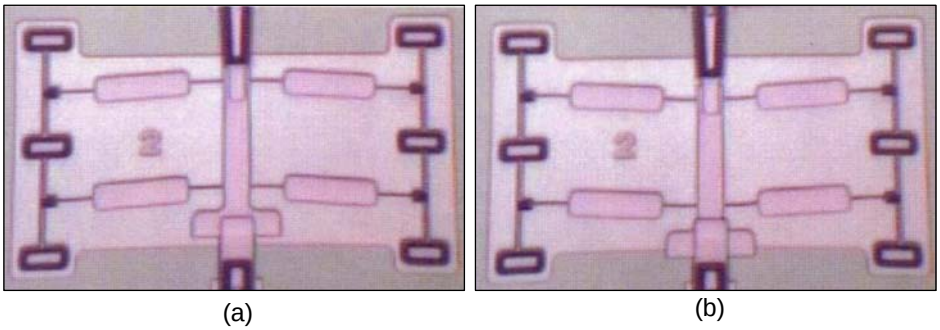

Figure 2-23: A micrograph of the two stable states of the fabricated fully-complian bistable mechanism [17].

been conducted on reducing the power consumption [77] and improving the linearity of the output displacement [78], when the compliant bistable mechanism is switched from one stable state to the other stable state.

Besides using multi-segment mechanisms to construct compliant bistable mechanisms, a monolithic compliant bistable mechanism has also been demonstrated [18]. As illustrated in Fig. 2-24, this mechanism contains two curved clamped-clamped beams that are rigidly connected at the centre. Compared with the mutli-segment compliant mechanisms, the bistable mechanism has a smaller footprint and better stress distribution which helps to extend its lifetime.

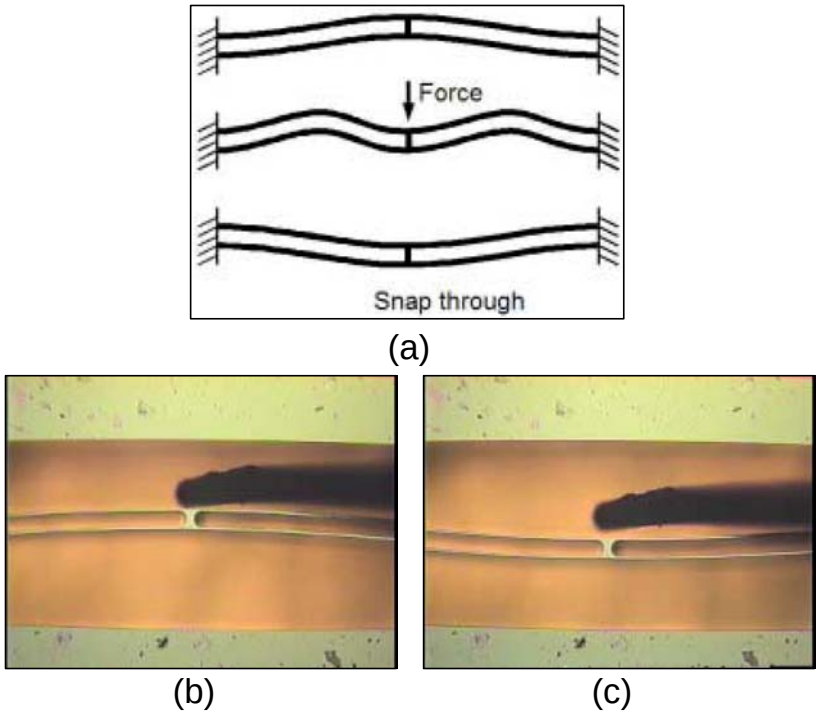

Figure 2-24: A centrally-connected double curved beam: (a) a schematic view, (b) one stable state, and (c) the other stable state [18].

2.3.2 Latch-lock Mechanism

A latch-lock mechanism is developed by using two or more MEMS actuators with synchronized control signals. Various MEMS actuators have been employed to design latch-lock mechanisms [19, 20, 79, 80, 81, 21]. Unlike the design of the compliant bistable mechanism, the design of the

latch-lock mechanism is straightforward since MEMS actuators have been well characterized in the literature. In addition, the concept of a latch-lock mechanism is easily implemented to achieve a latching mechanism with multi-stable states.

Fig. 2-25 reflects a surface micromachined bistable microrelay, based on the latching of a two-segment thermal actuator [19]. This two-segment thermal actuator contains two independently actuated bimorph actuators. By changing the operating sequence of the two bimorph actuators, two stable latching states are attained: ON and OFF. The two stable states are then separated by measuring the resistance between the two contact pads. This bistable microrelay is operated at about a 12 mW power level and takes 0.5 ms to latch and 0.1 ms to unlatch.

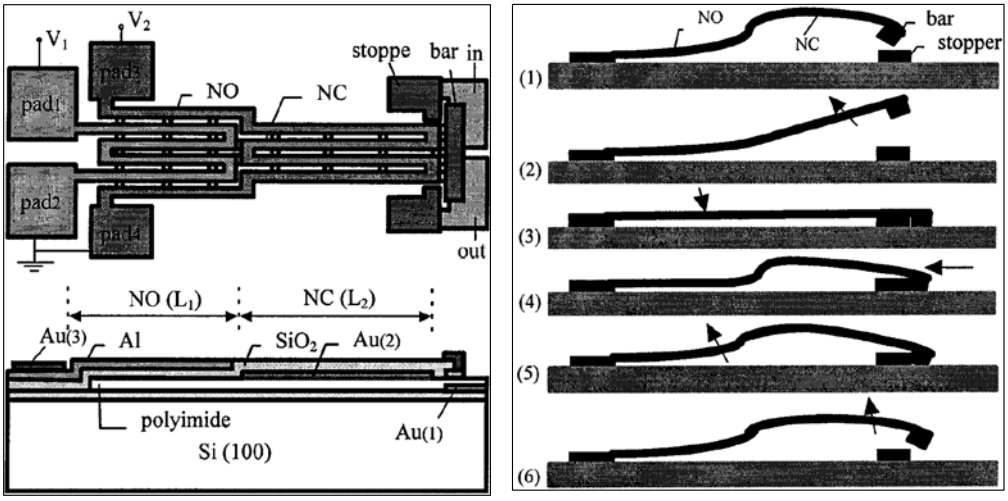

Figure 2-25: A bistable microrelay with thermal actuators: (a) top and crossection view of microrelay and (b) latching and unlatching procedures [19].

Typically, latch-lock mechanisms that use thermal actuators for the latching and unlatching motions cannot be operated at high speeds, since a certain amount of time is required to let thermal actuators to cool down for each operation cycle. For the applications where high speed operation is essential, electrostatic actuators are good candidates. Fig. 2-26 depicts a mechanically tri-stable Single-Pole-Double-Throw (SPDT) switch, where electrostatic actuation is employed to change between the stable states [20]. This tri-stable switch consists of two curved electrodes and three cantilever beams. To prevent short circuits, mechanical stoppers are placed

between the electrodes and cantilever beams. The actuation voltages for the different functions of the switches are less than 85 volts. No power input is required during the operation, and the switching speed is limited only by the size of the cantilever beams.

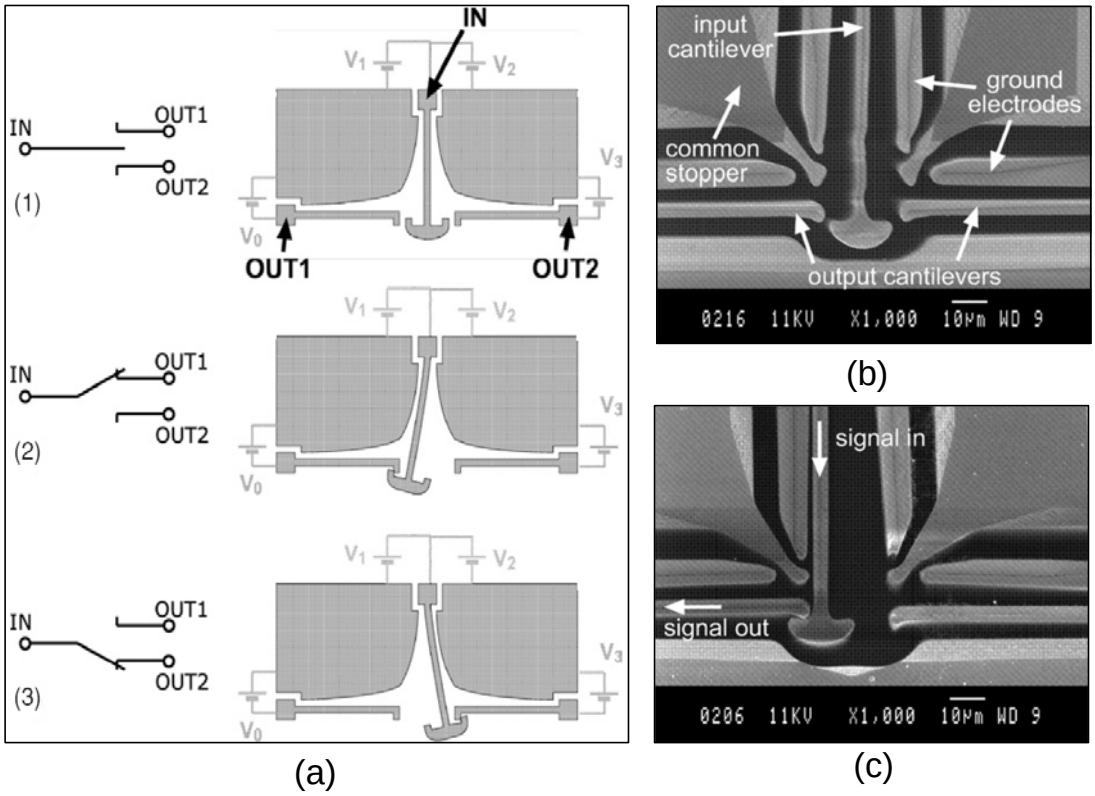

Figure 2-26: A mechanically tri-stable SPDT switch: (a) three mechanical stable positions, (b) the SEM of the switch in the OFF state, and (c) the SEM of the switch at one of the ON states [20].

One primary advantage of latch-lock mechanisms is that their concept is readily adopted to design a multi-stable latching mechanism [21]. Fig. 2-27 (a) displays a single stage latch consisting of two cantilevers, connected to two thermal actuators. A toothed rack is mounted on one of the cantilevers. If Δ is the space between two adjacent teeth on the toothed rack, then the deflection of Y at the tip of the other cantilever is equal to a set of discrete values $Y = i\Delta$, where i is an integer. The precision is limited by the tooth size, which in turn, is restricted by the fabrication processes. Improved precision is possible by lever principle. At the position, y, a point near the anchor side of the cantilever, the deflection is derived as

$y = i\Delta'$, where $\Delta' = \Delta L'/L$. However, this increase in precision is achieved at the expense of the deflection decrease. It can be solved by cascading the mechanisms as signified in Fig. 2-27 (b). The feasibility of such multi-stable latching mechanisms has been demonstrated by a MEMS variable optical attenuator [21, 82]. The layout of the fabricated device is illustrated in Fig. 2-28, and a travel range of 100 μm with a resolution of 1 μm is achieved. This latching concept has also been adopted by other designs [83, 84, 85].

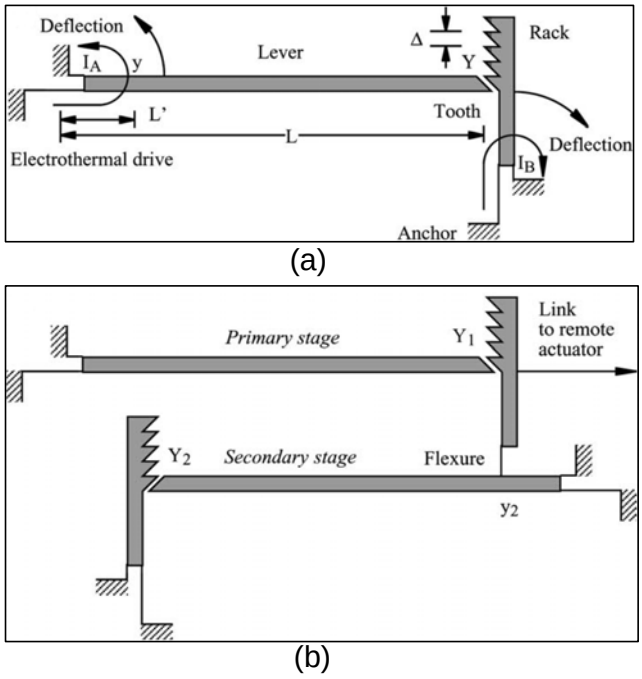

Figure 2-27: The principle of the multi-state latch-lock mechanism: (a) the single stage and (b) the multi-stage [21].

Multi-stable latching mechanisms suggested by [21, 83, 84, 85] are all in-plane, since thick structures are difficult for out-of-plane motions. Fig. 2-29 shows an out-of-plane multi-stable latching mechanism fabricated by a conformal surface micromachining process [22]. The interference in this latching mechanism is produced by the conformal nature of the fabrication process. The holes in the first structure layer, poly1, are conformally filled by material from the second structure layer, poly2. These dimple-like structures prevent the in-plane motion that are generated by the actuators in the poly1 layer. When a current is applied to the clamped-

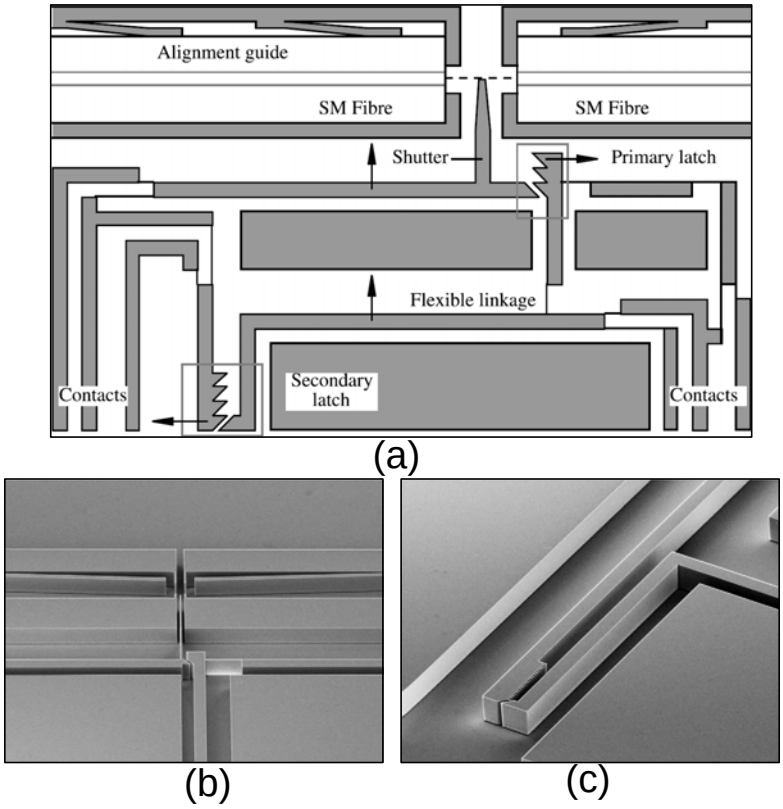

Figure 2-28: (a) The layout of a variable optical attenuator with a two-stage latching mechanism, (b) the SEM of the primary latch, and (c) the SEM of the secondary latch [21].

clamped beam in the poly2 layer, it buckles out of plane, and no constraints exist for actuators in the poly1 layer. Although this latching mechanism is compact, it requires two structure layers and the step resolution between stable states is limited by the fabrication process.

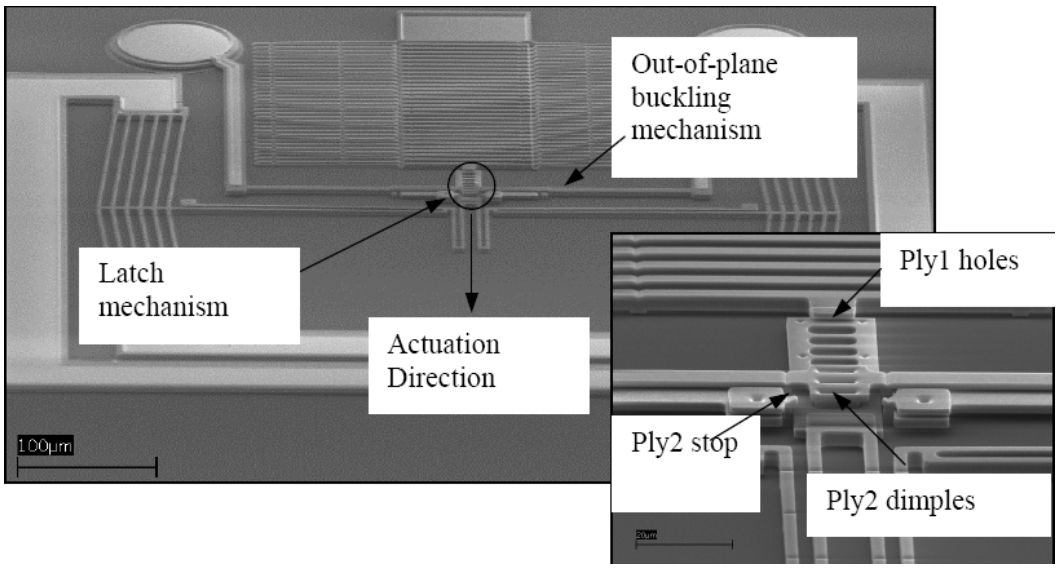

Figure 2-29: The latching mechanism based on the conformal deposition of thin films [22].

2.3.3 Other latching mechanisms

In certain MEMS applications where a magnetic source is obtainable, latching mechanisms are achieved by using an external magnetic source to hold the moving parts in stable positions [86, 23, 87]. The latching micromagnetic relay, illustrated in Fig. 2-30 (a), comprises a permanent magnet, an embedded planar coil, and a cantilever that consists of one layer of soft magnetic material and one layer of gold. In the stable states, the magnetic force, provided by the permanent magnet under the substrate, holds the cantilever in up position (ON) or down position (OFF). When a short current pulse is applied to the planar coil, a momentary magnetic field is generated to switch the relay. Depending on the polarity of the short current pulse, the relay can be switched from the ON state to the OFF state or the OFF state to the ON state. Fig. 2-30 (b, c) offers two configurations of the fabricated microrelays.

This microrelay has a low power consumption during switching (< 93 μJ) and requires

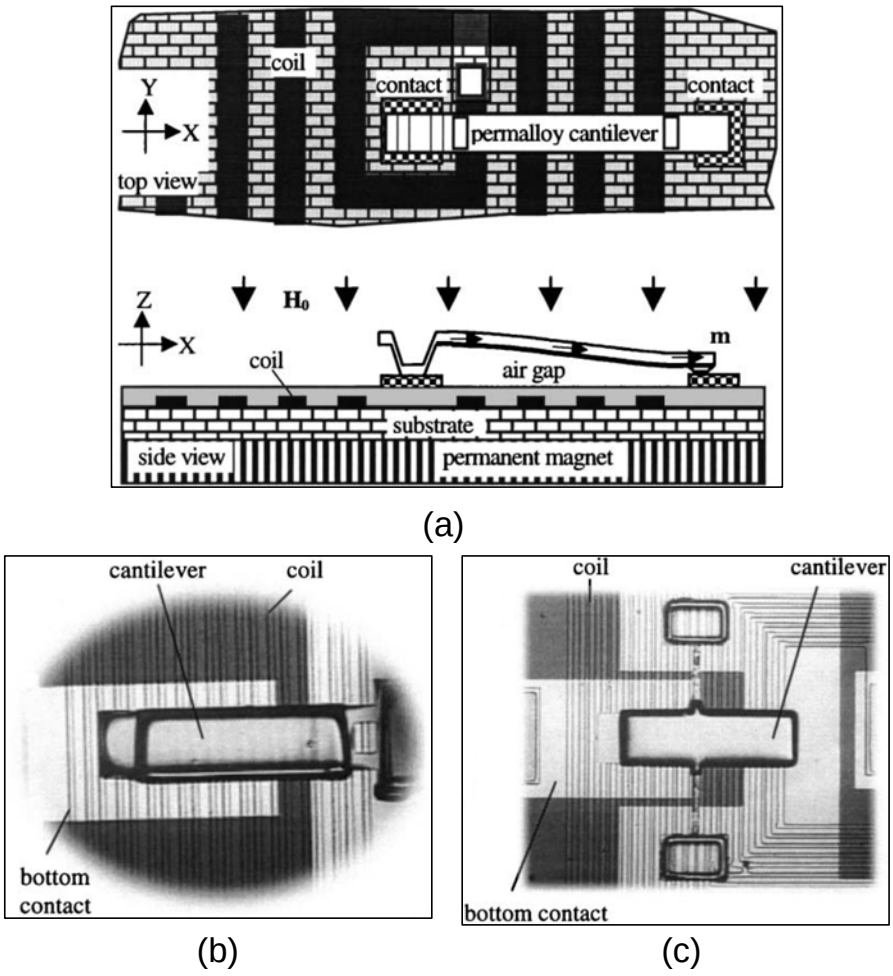

Figure 2-30: (a) The top and side views of the magnetic latching relay, and (b, c) the micrographs of the fabricated devices [23].

only 5V to operate. The planar micromachining process makes this microrelay suitable for batch fabrication. The switching time is about 0.4 ms and can be shortened by modifying the fabrication process (to decrease the gap) or the mechanical structure (to reduce the inertia).

Besides the use of a magnetic field to achieve the stable states, an electric field can be used to sustain the latching mechanism in latched position. However, the strength of the electric field is reversely proportional to the distance between two electrodes. A very large voltage is required to obtain a small travel range of a moving electrode. Therefore, other types of actuators, which can generate large actuation force with low input voltages, are needed to bring the moving electrode close to the stationary electrode. Then the electric field is applied across the two electrode to hold the latched position. Latching mechanisms with thermal actuators or magnetic actuators, combined with electrostatic actuation, have been demonstrated in the literature [24, 88, 89].

Fig. 2-31 depicts a low-voltage and low-power RF MEMS switch, actuated by the combination of a magnetic and an electrostatic force [24]. The cantilever beam is separated from the signal line by a 10-μm gap. To move the cantilever down and turn on the switch, a current of 53 mA, which corresponds to 2V of the DC voltage, is required to pass through the actuation coil on the top of the cantilever beam. Once the switch is ON, a DC voltage is applied across the cantilever beam and the bottom electrode to hold the switch at the ON state. Instead of magnetic actuators, thermal actuators have also been employed in a similar switch design [88]. A latching mechanism using the combination of electrothermal and electromagnetic with electrostatic forces utilizes the advantages of both types of actuation: electrothermal and electromagnetic actuation can generate a large force and deflection, whereas the electrostatic actuation consumes no power. However, the electric charging effect might cause concerns for this type of latching mechanism.

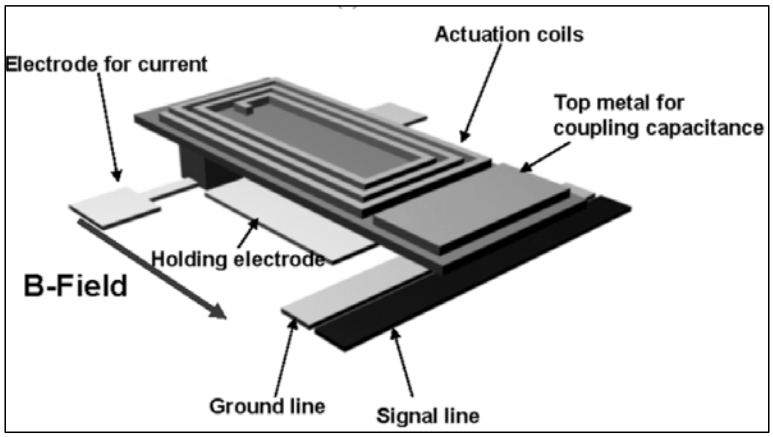

(a)

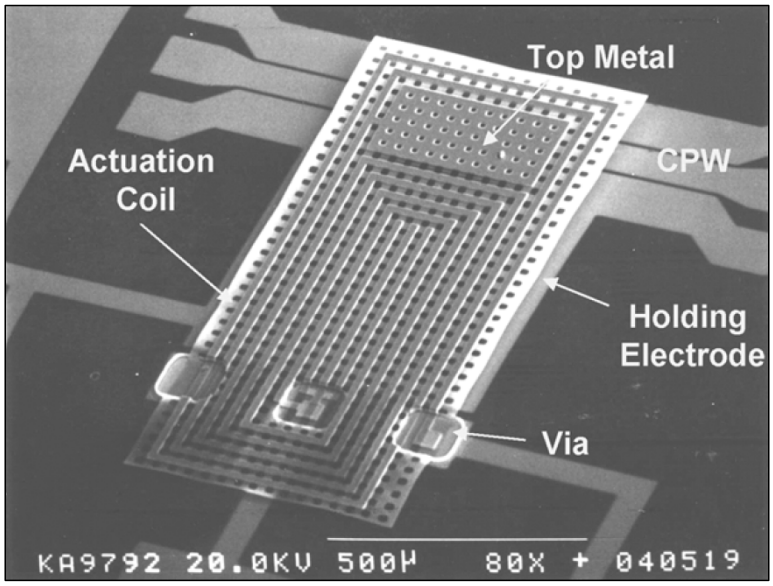

(b)

Figure 2-31: (a) A schematic diagram of a shunt-type switch and (b) an SEM of the fabricated device [24].

Chapter 3

Fine Tuning of Micromachined Bandpass Filters

3.1 Introduction

Microwave and millimeter-wave filters are widely employed not only in telecommunication applications but also in instrumentations and sensing applications such as anti-collision radar [90, 91]. At high frequencies, traditional filter techniques encounter many difficulties such as fabrication limitations and low quality factors due to the substrate loss. The fabrication tolerance and stringent requirements necessitate that the filters be fine tuned by tuning elements. However, their integration and assembly increase the design complexity and costs dramatically.

MEMS technology has the potential to provide various advantages to overcome these difficulties. Over the past few years, several research groups have demonstrated different types of micromachined filters with excellent performances [92, 93, 94, 95, 96]. MEMS filters, with a substantial loss reduction have been attained by partially removing the substrates [92] or fabricating the entire filter on a suspended thin dielectric film [93]. Micromachined 3D filters eliminate the losses from substrates, and provide other advantages such as size reduction [95, 96]. However, to authors' the best knowledge, all existing micromachined filters cannot be fine tuned after fabrication. Any tolerance generated from materials and during fabrication process degrades the filters' performance, which potentially reduces the yield and increases the cost.

In this chapter, a new method to compensate for the fabrication tolerance by embedding MEMS actuators as tuning elements in micromachined filters is developed. When hundreds of filters are batch-produced on a wafer by micromachining techniques; the tuning elements can be integrated and monolithically fabricated by the same techniques on the same wafer. No post-assembly is needed. Furthermore, these filters can be tuned electronically instead of manually tuning which is expensive. This newly developed fine tuning concept is applied to two types of mcicromachined bandpass filters: One is a quasi dual-mode microstrip line filter and the other is a ridge waveguide cavity filter with a coplanar input and output interface. Both types of filters are fabricated and tested to prove the proposed concept. The experimental results demonstrate the feasibility of using the novel built-in MEMS actuators to fine tune micromachined filters.

3.2 Fine Tuning Micromachined Quasi Dual-Mode Filter

3.2.1 Design and Analysis

Fig. 3-1 is a schematic view of a micromachined filter, with embedded tuning elements. A two-pole quasi dual-mode filter with CPW input and output ports is integrated with a number of MEMS actuators. The fine tuning of the micromachined filters is implemented by disturbing the electromagnetic field of a filter with close-by MEMS actuators. When the DC power is applied, these actuators generate a forward motion. This changes the loading effect of the nearby resonator, which in turn, changes the response of the filter.

The position of the MEMS actuators and the gap between the resonator and the MEMS actuators are two critical design parameters. They can be numerically determined by analyzing the electromagnetic field distribution of the resonator. To achieve the maximum tuning range, all the MEMS actuators should be placed at the locations that have a high density of field distribution. As portrayed in Fig. 3-2, the field distribution of a single resonator at its resonant frequency indicates that the actuators should be placed at each end of the resonator. For choosing the gap between resonators and MEMS actuators, two factors should be balanced: the impact of the MEMS actuators before tuning and the maximum displacement of the MEMS actuators. In other words, the MEMS actuators should have a minimum impact on the filter response before tuning; if fine tuning is needed, the MEMS actuators can move close enough

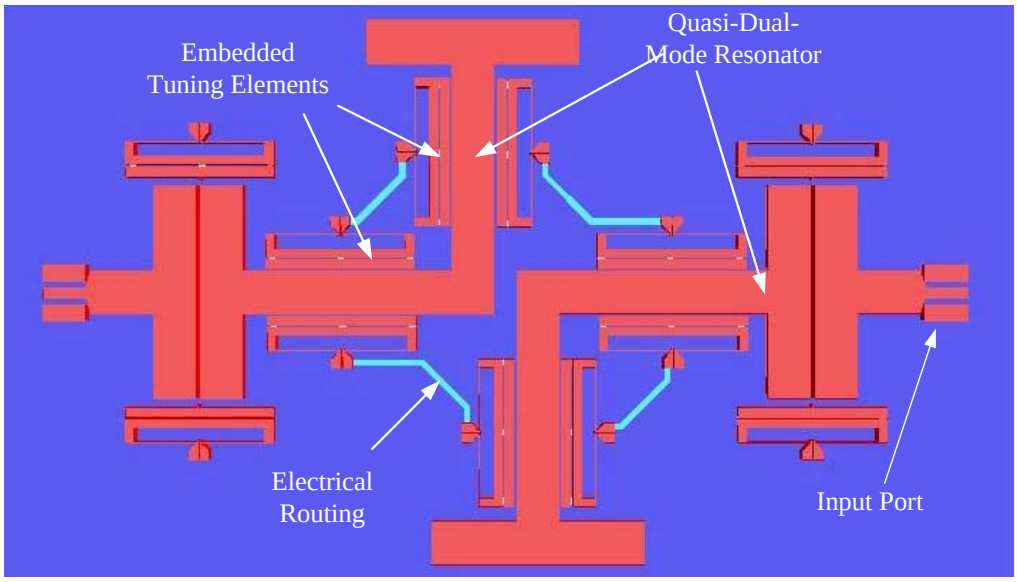

Figure 3-1: A schematic view of a micromachined quasi dual-mode filter with embedded tuning elements.

to the resonators. A 20-mm gap is selected after carefully considering these two factors. Here, the thermal actuators are employed as embedded tuning elements due to their relative larger displacement and low actuating voltage [97]. Different types of MEMS actuators can serve as embedded tuning elements, as long as they are capable of providing a proper motion for filter tuning and suitable to the fabrication process.

3.2.2 Fabrication Process

Several 2-pole quasi dual-mode filters are fabricated on a 3-inch diameter, high resistivity ($\rho > 10^{12}\ \Omega{\cdot}cm$) and low dielectric constant ($\epsilon_r = 9.9$) alumina wafer. A SU-8 (Mcirochem Inc., MA) photo resist based surface micromachining technique is employed. As illustrated in Fig. 3-3, the device consists of three layers: the bottom ground plane, suspension layer, and top tuning structure layer. First, a seed layer (chrome and copper) is sputtered on the substrate to form the electroplating base; then, a 5-mm thick SU-8 layer is created by photo resist spin-coating and UV lithography. After patterning the SU-8 layer, electroplating is performed to build the ground plane, as seen in Fig. 3-3.1 - 3-3.2. The other two metal layers, the suspension layer

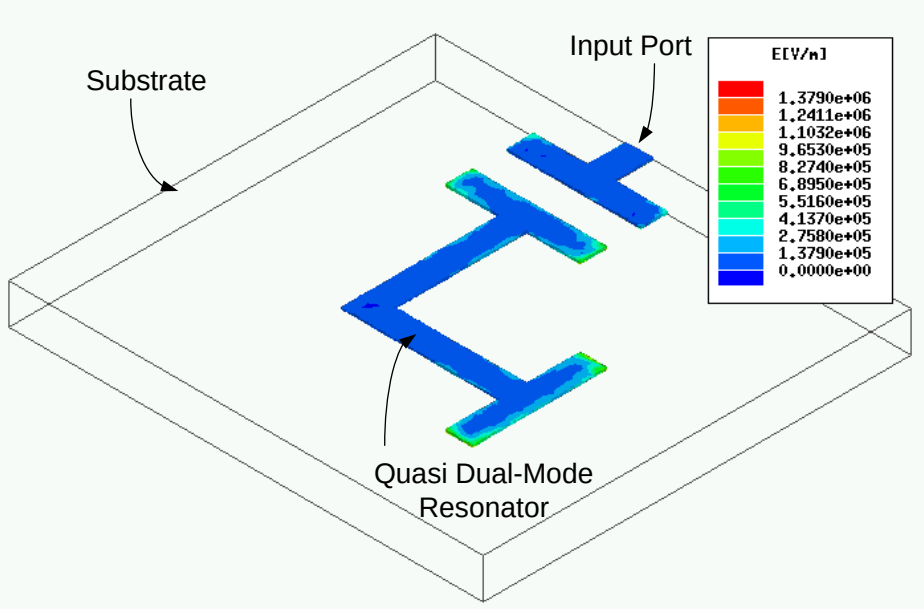

Figure 3-2: A simulated E-field distribution of a resonator at its resonant frequency.

and the top tuning structure layer, are produced by the same UV patterning and electroplating techniques as those of the first layer (Fig. 3-3.3). After the top seed layer is sputtered, a thin layer of gold is electroplated to reduce the oxidation effect and to provide the probing pads. Finally, the SU-8 electroplating mold layers and metallic seed layers are removed by a plasma (20% CF4: 80% O2) dry etch and a wet chemical etch, respectively.

3.2.3 Test Results

A micrograph of the micromachined filter with the embedded tuning elements is displayed in Fig. 3-4. The MEMS actuators are placed in three different locations: position A is for tuning the input and output coupling; position B, for tuning the coupling between the resonators; and position C, for tuning the resonant frequency of the resonator. To increase the MEMS actuators' tuning effect, spiral microstrip lines are added to the MEMS actuators. The inset in Fig. 3-4 relates the detail of the micromachined filter with thermal actuators as tuning elements. The RF measurements from 1 to 10 GHz are carried out by an HP8722ES S-parameter network analyzer, and GSG-tipped Cascade Microtech microwave probes. Two DC probes are required

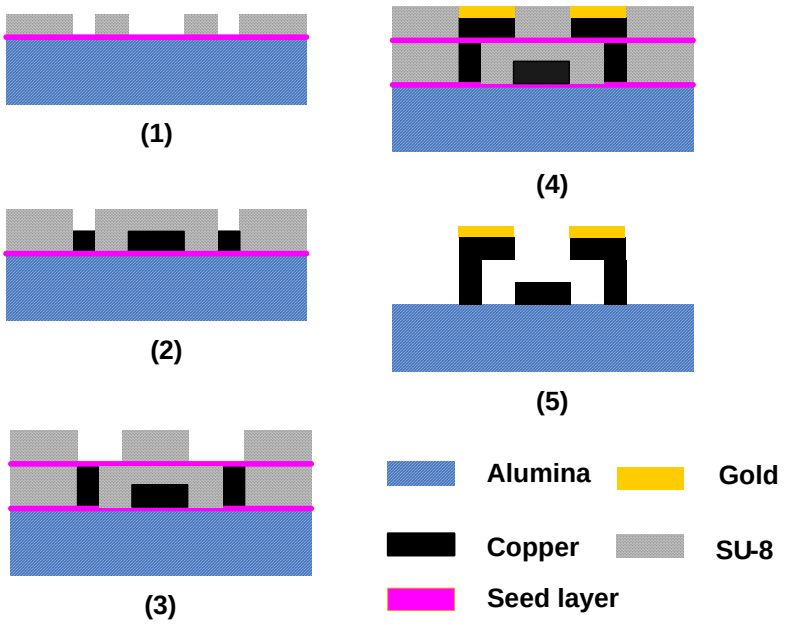

Figure 3-3: The fabrication process flow chart for the quasi dual-mode microstrip filter.

for actuating the thermal actuator. Fig. 3-5 shows the filter response without tuning, where the center frequency of the filter is 5 GHz, and the insertion loss is 2 dB at the center frequency. This filter has a fractional 3-dB bandwidth of 7.35%. The out-of-band rejection is better than 30 dB from 4 GHz to 1 GHz, and 6 GHz to beyond. A comparison of the filter responses with and without tuning is offered in Fig. 3-6.

3.2.4 Discussion

The test results indicate the MEMS actuators' capability of fine tuning the micromachined filters. The tunability is limited to two factors: First, the fabricated filter operates in a relatively low frequency range; therefore, the wavelength of the filter is much larger than the size of the MEMS actuators, which limits the tuning capability of the MEMS actuators. However, most micromachined filters are designed for high frequency applications (usually a few tens of GHz). Consequently, this limitation is not an issue in such a frequency range. Secondly, for planar type filters, most of the electromagnetic field is contained in the dielectric substrate, as seen in Fig. 3-7 (a), which also constrains the tunability of the MEMS actuators. This problem can be

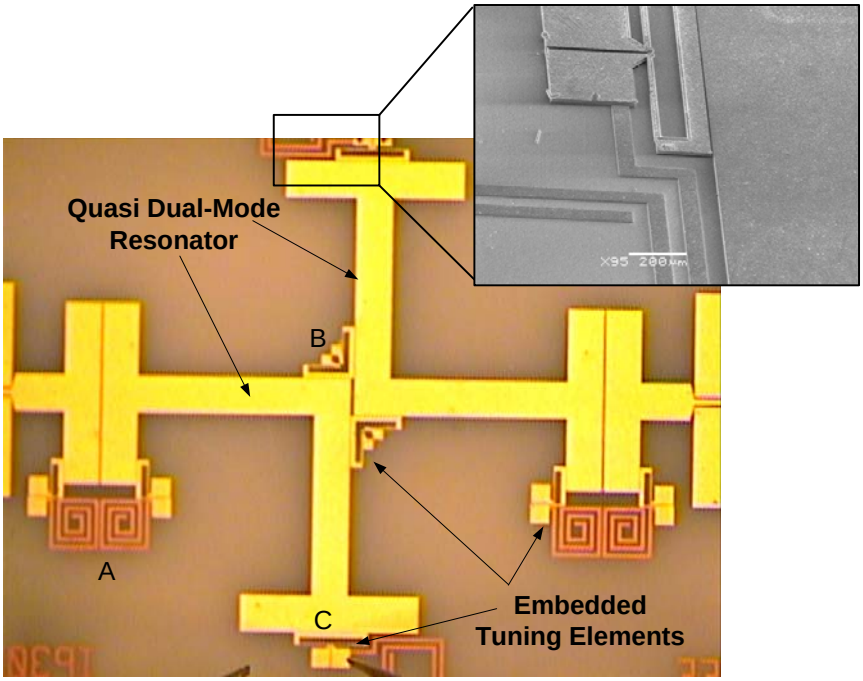

Figure 3-4: A micrograph of a micromachined 2-pole quasi dual-mode filter with embedded tuning elements.

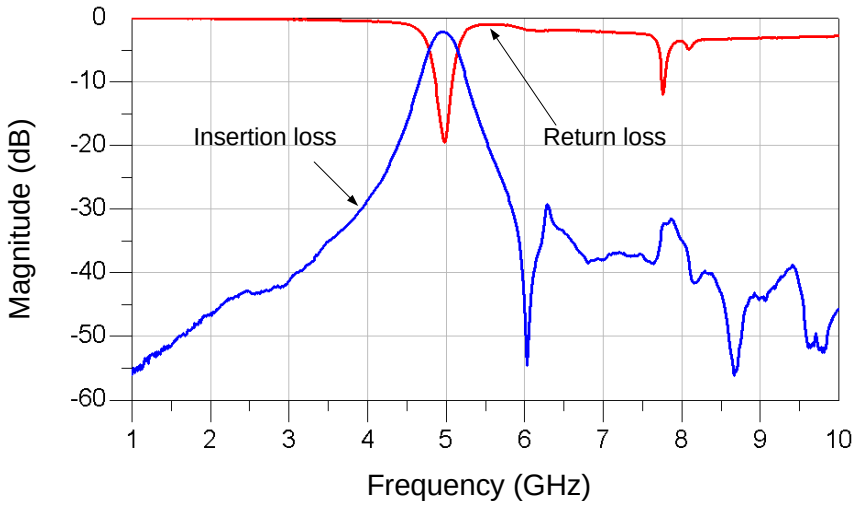

Figure 3-5: The test results of a micromachined 2-pole quasi dual-mode filter without tuning.

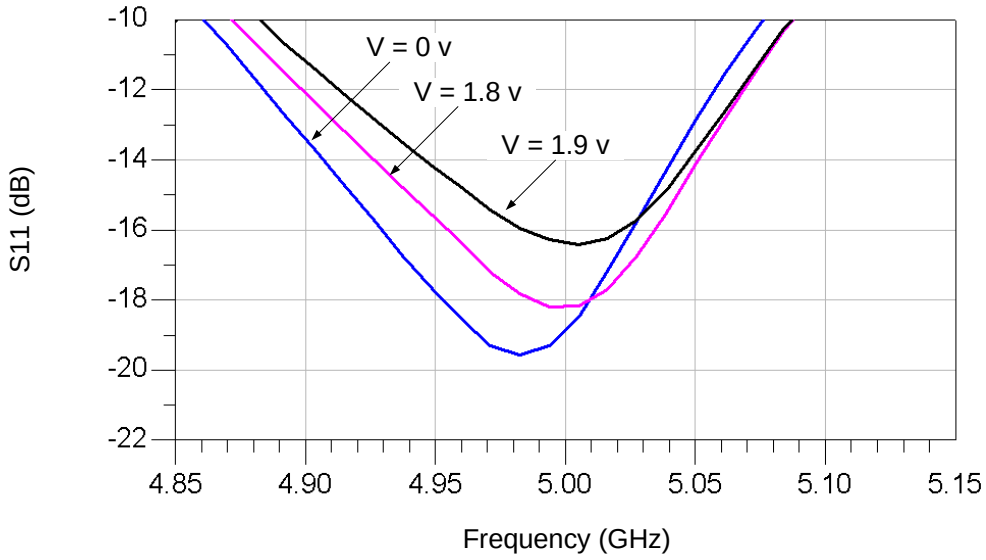

Figure 3-6: A comparison of the return loss responses of a micromachined filter at different tuning voltages.

solved by adding a trench underneath the gap between the filter and the tuning elements, as indicated in Fig. 3-7 (b). The electromagnetic simulation results in Fig. 3-8 prove the validity of the concept. A tunable filter with a 1-GHz tuning range is achieved with the same MEMS actuators.

3.3 Fine Tuning Micromachined Ridge Waveguide Filter

3.3.1 Design and Analysis

Ridge waveguide filters exhibit a low insertion loss, high spurious performance, and compact in size. The cross sections of two typical ridge waveguide structures are shown in Fig. 3-9, where their length extends in the Z direction. When the ratio of a/s is fixed, where a is the width of the cavity and s is the width of metal ridge, the cut-off frequency of a ridge waveguide structure is determined by the ratio of d/b. Here, d is the gap between the top cover of the cavity and the top surface of the metal ridge, and b is the height of the metal ridge. The smaller the ratio of d/b is, the higher the cut-off frequency is. This relationship indicates that a lower resonance frequency

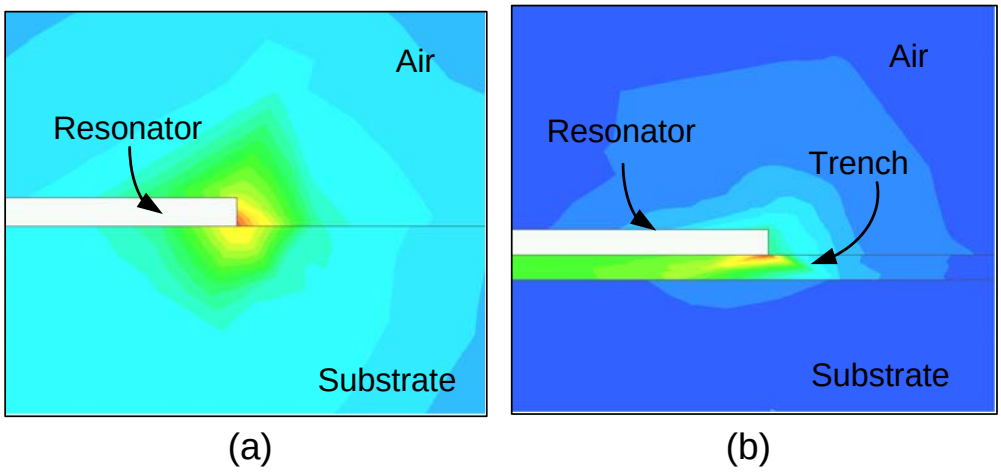

Figure 3-7: Electric field distribution of microstrip resonators (a) without and (b) with the trench.

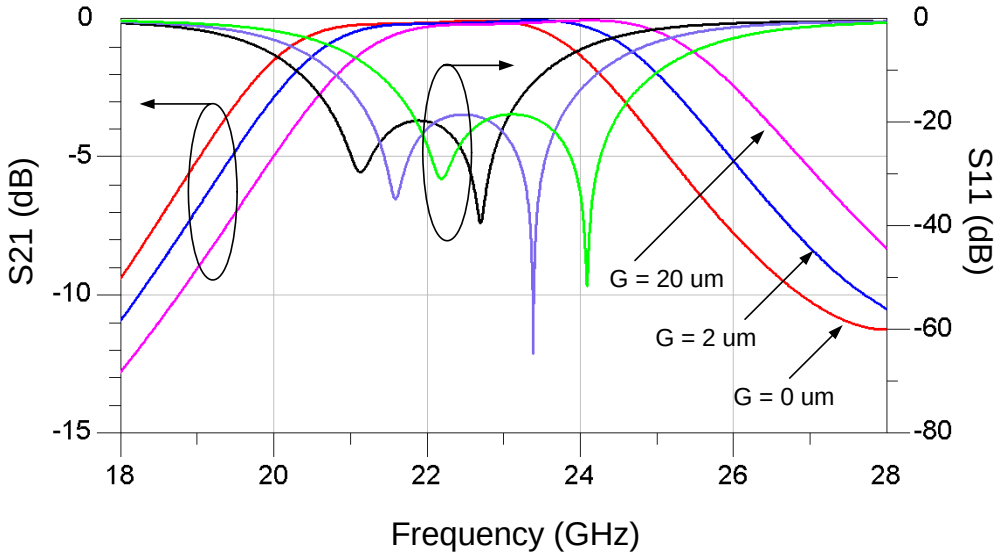

Figure 3-8: A comparison of the simulation results of a micromachined filter with trenches at various tuning gap widths.

is possible by using smaller ridge waveguide structure, as long as the ratio of d/b is small enough. Traditional fabrication techniques have limited capabilities for providing a low value of d/b, restricting the size reduction of the ridge waveguide filters. However, micromachined ridge waveguide filters have a huge advantage with the MEMS fabrication techniques; that is, they can create a gap as small as a few micrometers and a ridge as high as a few hundred micrometers, which implies that the ratio of the d/b can be as low as a few one hundreds.

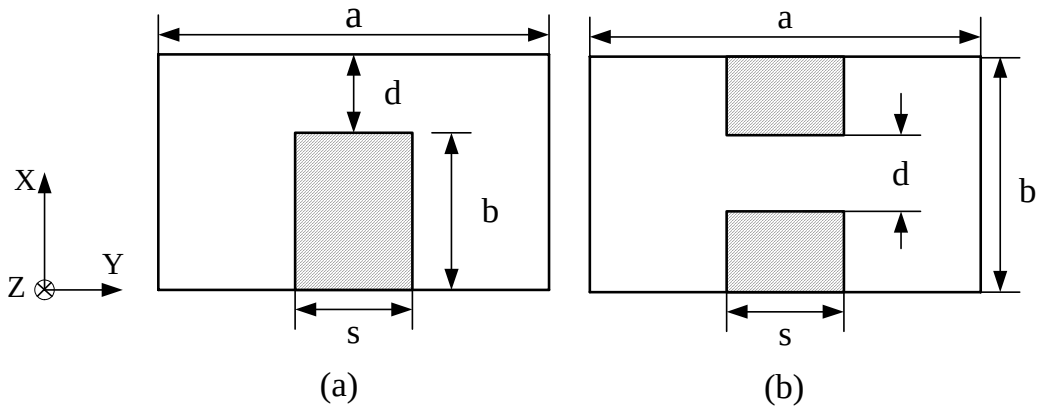

Figure 3-9: (a) a cross section of a single ridge waveguide structure and (b) a cross section of a double ridge waveguide structure.

Fig. 3-10 records a typical relationship between the resonant frequency of a ridge waveguide resonator and the ratio of d/b when the ratio of a/s is fixed. If the design value of d/b is varied by 1%, the corresponding resonance frequency changes about 200 MHz. For most commercial fabrication foundries, a 1% fabrication tolerance is quite reasonable, indicating that fine tuning is essential to micromachined filters.

A micromachined ridge waveguide filter with embedded tuning elements is also designed, fabricated, and tested to prove the concept of the filter fine tuning by the use of MEMS actuators. The filter design is based on a 3D microfabrication process, provided by MOSIS and Microfabrica Inc. The process is described in the following section. Fig. 3-11 is a schematic view of a micromachined filter, embedded with tuning elements. The fine tuning of such filters is conducted by disturbing the electromagnetic field of a filter with close-by MEMS actuators. When DC power is applied, the MEMS actuators generate a forward motion and slide the tuning

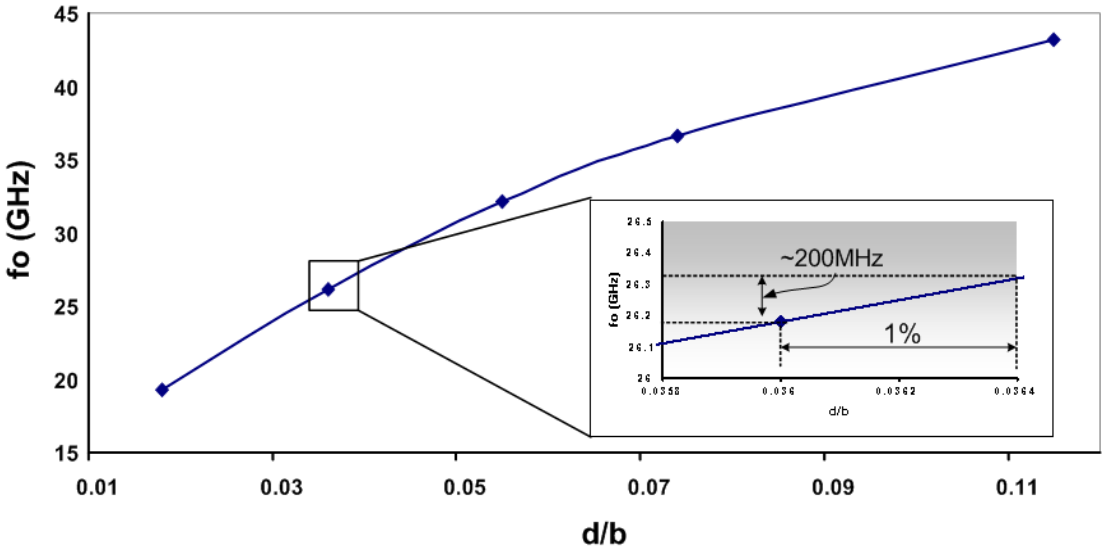

Figure 3-10: A ridge waveguide resonance frequency vs. the ratio of d/b when a/s is fixed.

rod into the cavity of the ridge waveguide filter through a small opening on the sidewall. This changes the loading effect of the nearby resonator, which in turn, changes the overall response of the filter.

Thermal actuators are employed as the embedded tuning elements, since they have a relatively large displacement and high force at a low actuating voltage (less than 5 volts) [97]. Different types of MEMS actuators can serve as embedded tuning elements, as long as they can provide the appropriate motion for filter tuning and suitable to the filter fabrication process.

Commercial electromagnetic simulation software are employed to analyze the RF performance of the proposed ridge waveguide filter. The two-pole filter has a center frequency of 26.9 GHz and is predicted to have a 10% bandwidth with an insertion loss of 1.8 dB at the mid-passband. When the tuning elements are fully inserted into the cavity, they can shift the centre frequency of the filter up to 200 MHz and maintain the filter's bandwidth with every little change, as observed in Fig. 3-12.

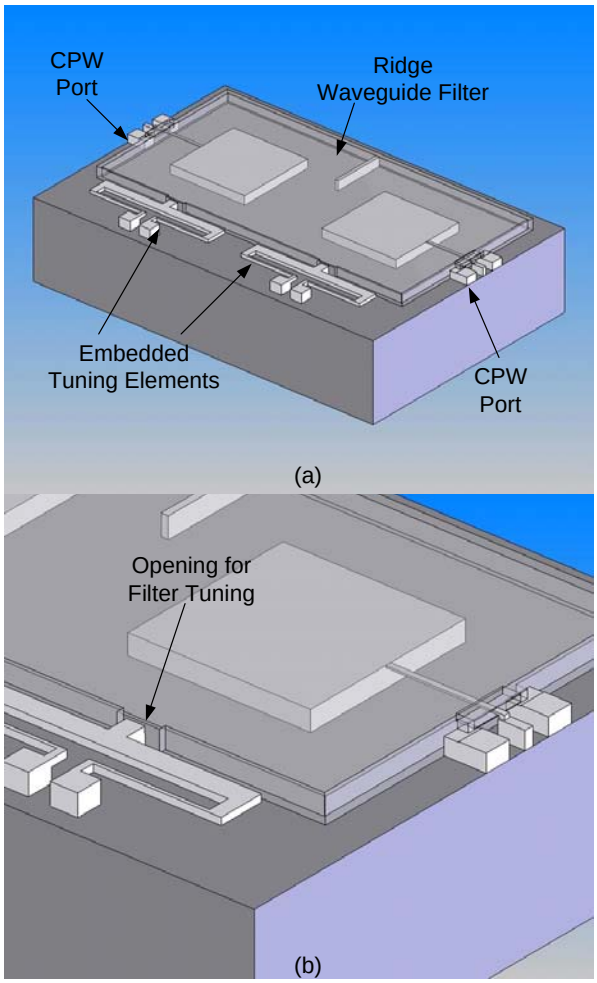

Figure 3-11: A schematic view of a micromachined ridge waveguide filter with embedded tuning elements.

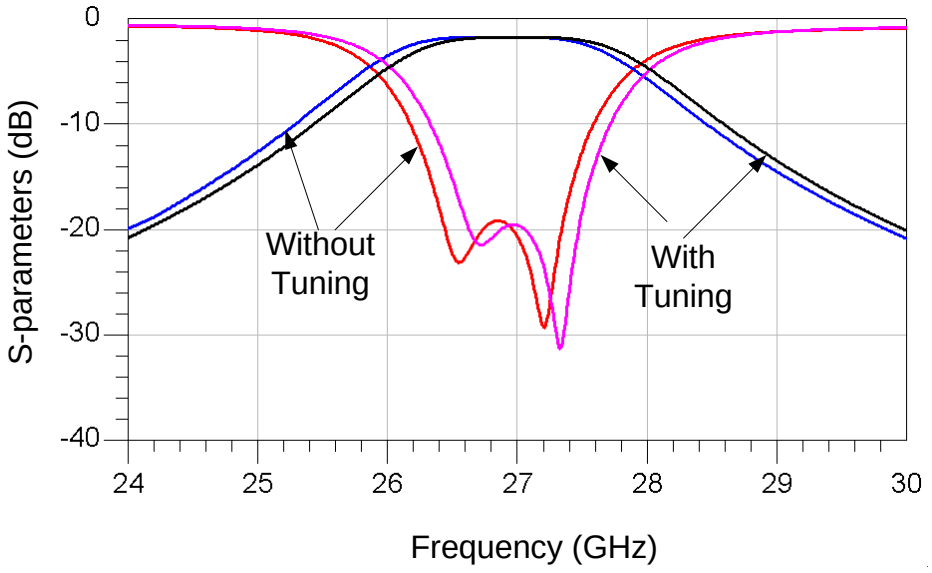

Figure 3-12: A comparison of the simulated responses of a two-pole filter with and without tuning elements.

3.3.2 EFAB^{TM} Fabrication Process

The proposed ridge waveguide filter with embedded tuning elements is fabricated by EFAB^{TM} ACCESS, a new multi-user micromachining process provided by MOSIS and Microfabrica Inc [25]. The EFAB^{TM} technology is a multi-layer microfabrication process, based on the deposition and planarization of metallic material. Multi-layer complex microscale devices are rapidly produced by repeating a few basic process steps multiple times. The EFAB^{TM} technology process flow begins with depositing and patterning sacrificial metal on a bare substrate, as described in Fig. 3-13 (a). Then, structural metal is blank deposited, Fig. 3-13 (b), to fill the space remaining from the previous step. The properties of the structure layer, such as the thickness, flatness, and the surface finish are precisely controlled by the planarization step in Fig. 3-13 (c). The process is repeated from step (a) to (c) until the desired structure is formed, as illustrated in Fig. 3-13 (d). Then a wet release step, Fig. 3-13 (e) is performed to remove the sacrificial metal.

In EFAB^{TM} technology, the number of layers and the thickness of each layer are varied so that designers can create a wide range of 3D microstructures for various applications. The

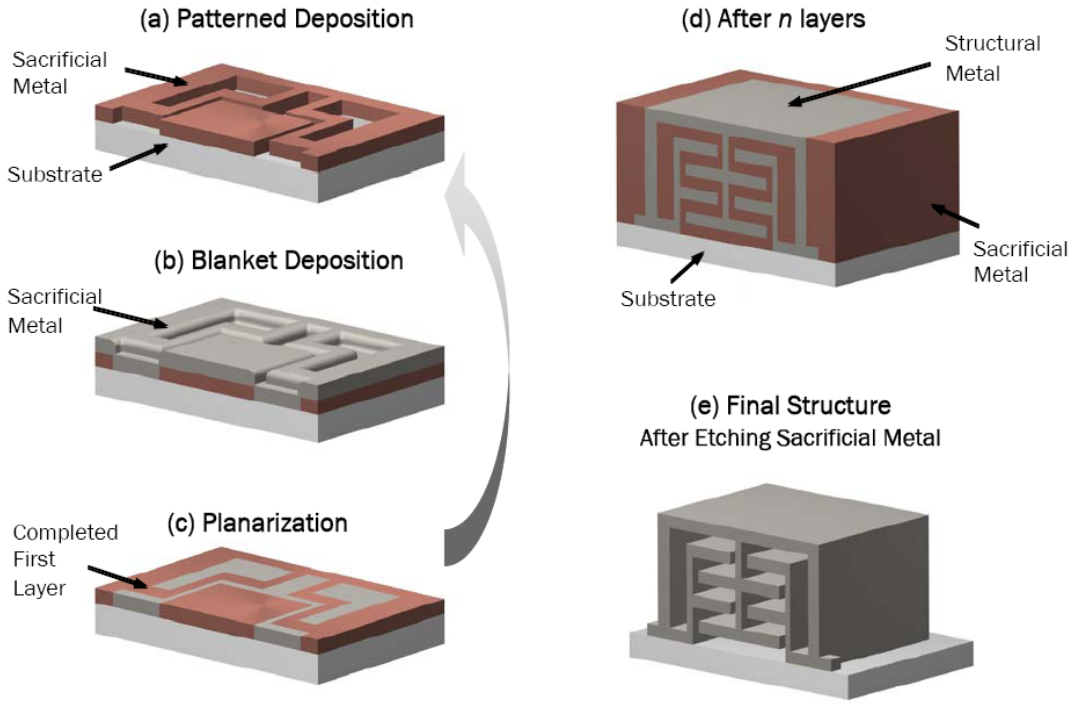

Figure 3-13: The EFAB^{TM}technology process overveiw [25].

EFAB^{TM} ACCESS process comprises 20 structure layers. The first layer is 10 μm thick, the second layer is 4 μm thick, and so on for all 20 layers. Nickel-cobalt (NiCo) is employed as the structure material and copper is used as the sacrificial material. All the devices are fabricated on the 1-mm thick alumina substrate in Fig. 3-14.

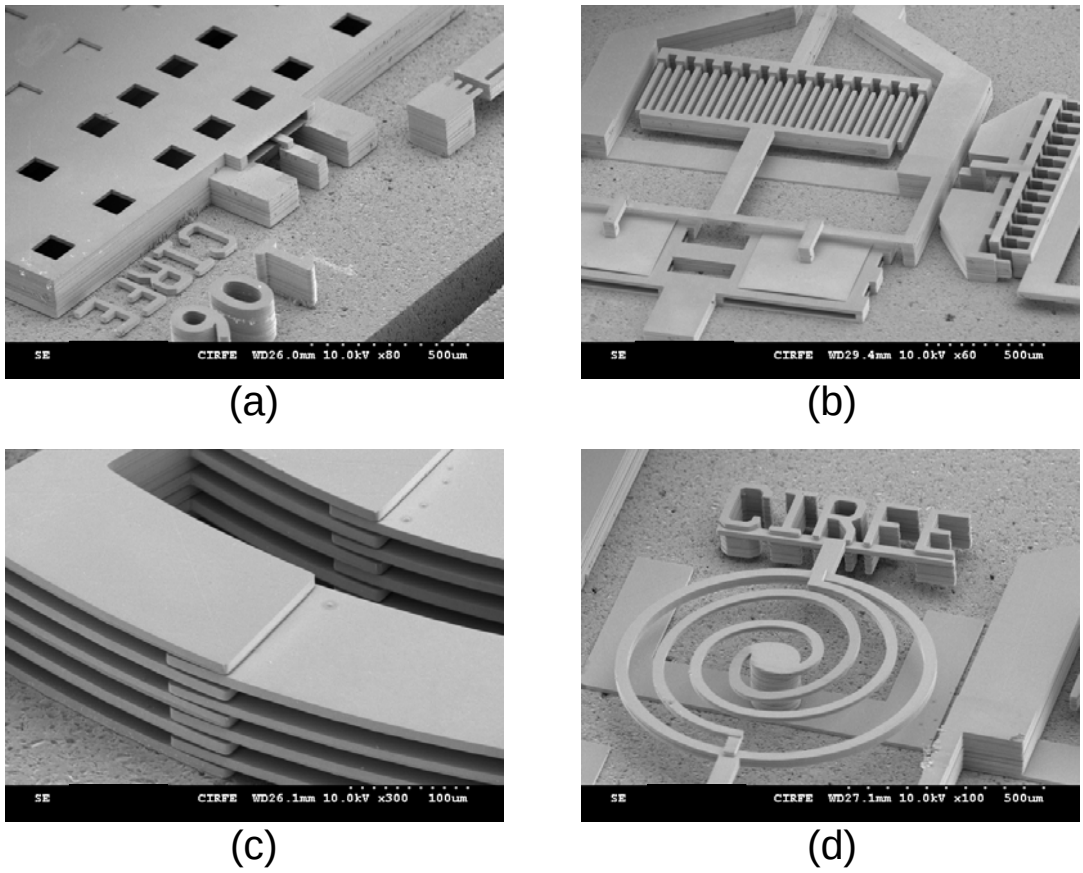

Figure 3-14: 3D microdevices fabricated by the EFAB^{TM} ACCESS process.

3.3.3 Test Results

As mentioned in the previous section, the resonance frequency of a ridge waveguide resonator is primarily dependent on the ratio of d/b when a/s is fixed. To take advantage of the capabilities of the EFAB^{TM} process and to create the ratio of d/b as small as possible, the ridge waveguide gap, d, is chosen to be 4 μm, and the height of the metal post, b, is 112 μm, which gives the ratio of d/b as 0.036. The footprint of the two-pole ridge waveguide filter is about 2mm x

4mm. Each thermal actuator has a footprint of 300 μm x 1500 μm, and carries a tuning rod with a size of 140 μm x 100 μm x 100 μm. Fig. 3-15 is an SEM of the micromachined ridge waveguide filter with embedded tuning elements. Since copper is the sacrificial material, release holes must be carefully placed on the top of the filter cavity in order to avoid undesirable short circuits inside the cavity.

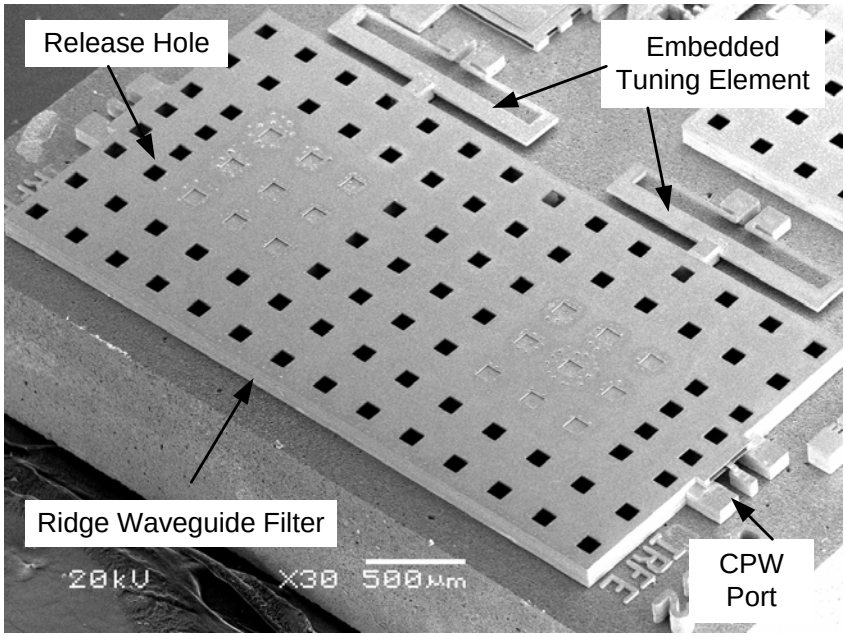

Figure 3-15: An SEM of the fabricated ridge waveguide filter with embedded tuning elements.

Thermal actuators are selected as the embedded tuning elements because of their large deflection and low actuating voltage (Fig. 3-16). When a DC voltage is applied, the two hot arms expand more than the cold arm, which pushes the cold arm forward to tune the filter. To prevent buckling during the actuation, the aspect ratio of the hot arms of the thermal actuators must be less than 1; that is, the width of the hot arm is less than the thickness of the hot arm. Generally, alumina has a good thermal conductivity; the heat loss through the alumina substrates can be considerably high, if the gap between the thermal actuators and the substrate is small. This decreases the deflection of the thermal actuators, which in turn, decreases the tuning capability of the thermal actuators. Thicker anchors should be used to ensure the gap is large enough.

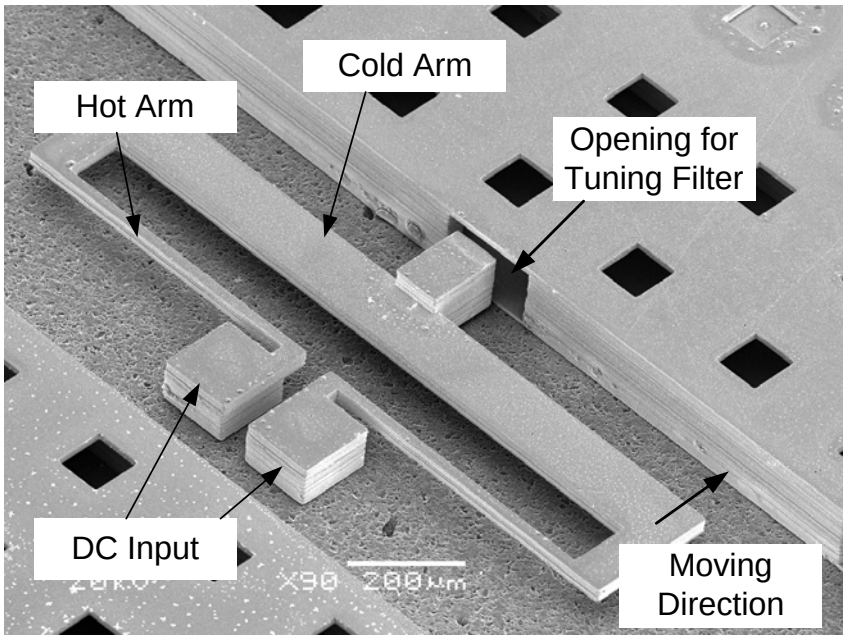

Figure 3-16: The SEM of a thermal actuator used as an embedded tuning element.

Fig. 3-17 consists of the measured response of the fabricated ridge waveguide filter without tuning. The centre frequency of the filter is 23.5 GHz, and the insertion loss is 3 dB at the centre frequency. This filter has a bandwidth of 5% and a spurious-free window as high as 40 GHz. A comparison of filter responses with and without tuning is exhibited in Fig. 3-18. The test results indicate an almost 200-MHz tuning range, when the two metal tuning rods that are attached to the thermal actuators are fully inserted into the cavity.

3.3.4 Discussions

The test results of the tunability of the thermal actuators in Fig. 3-18 is in good agreement with the simulation results in Fig. 3-12, which proves the feasibility of using embedded MEMS actuators as tuning elements for filter fine-tuning. However, there is a considerable discrepancy in the insertion loss between the simulated and test results. Besides the metallic loss, radiation loss through release holes and the discontinuity from one structure layer to the other that contributes extra losses, are not considered in the simulation. The center frequency of the test filter is 3.4 GHz lower than that of the simulated filter. As verified by the scanning electron

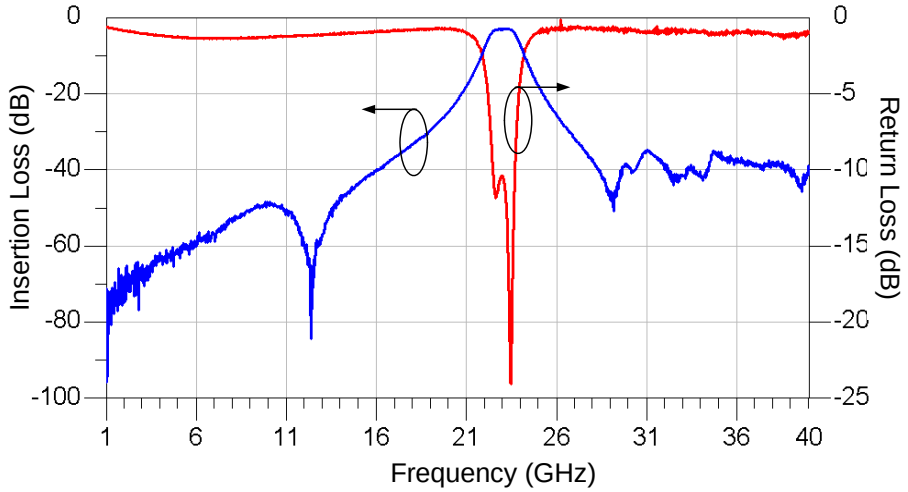

Figure 3-17: The measured response of the fabricated ridge waveguide filter with embedded MEMS tuning elements.

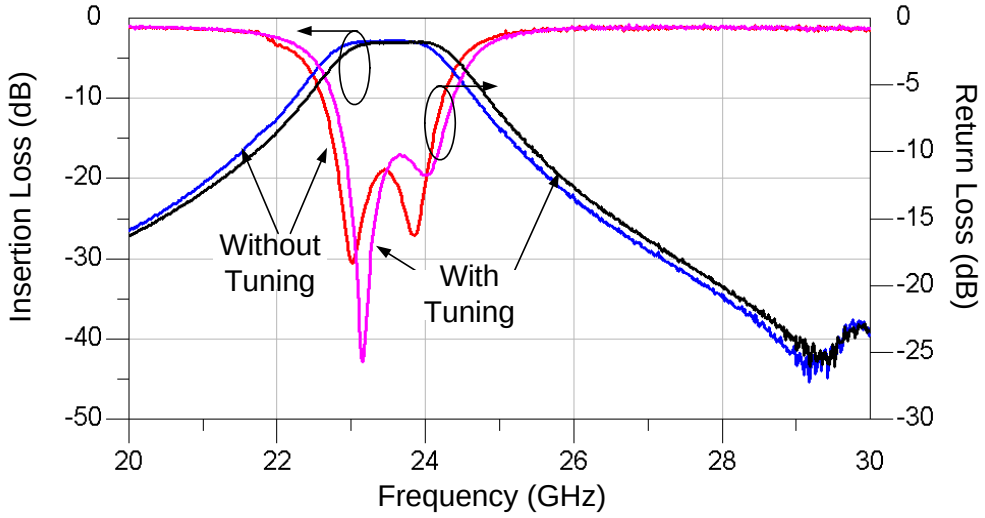

Figure 3-18: A comparison of the measured responses of the proposed design with and without tuning.

micrograph (Fig. 3-19.), this frequency shift is due to the fact that the fabricated gap, d, is 4.2 μm and the fabricated ridge height, b, is 136 μm which are all higher than the design values of 4 μm and 112 μm, respectively. This renders the ratio of d/b of the fabricated filter 14% lower than the design value. Such a large fabrication tolerance far exceeds the tuning capability that the thermal actuators can provide. New MEMS actuators with a larger deflection need to be developed to compensate for such a tolerance. However, as the fabrication process is refined, the tolerance is expected to be a few percent or less, which is the scope of this research.

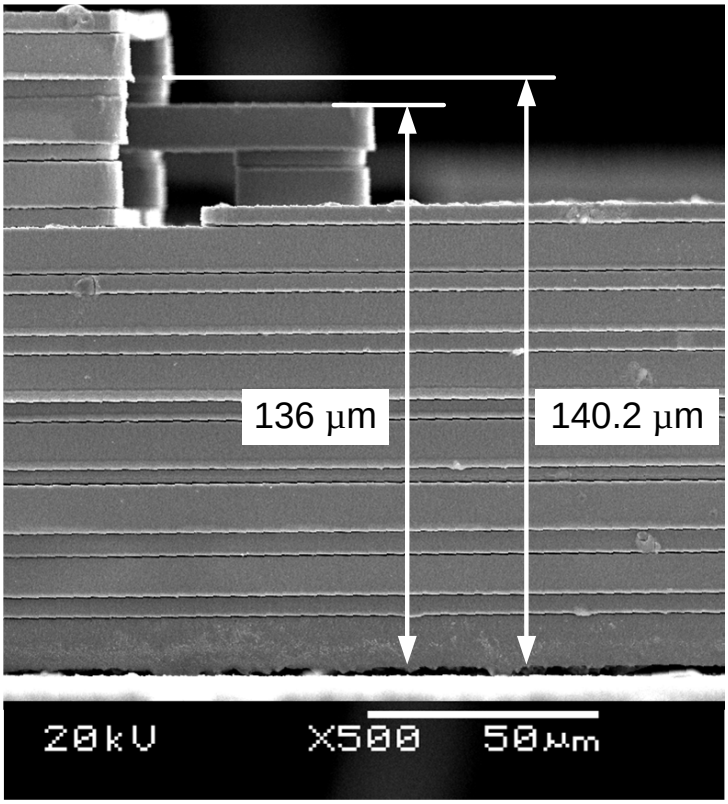

Figure 3-19: The side view of the input port of the fabricated ridge waveguide filter.

The quality factor of the filter can be further increased by fully implementing the fabrication capabilities of the EFAB^{TM} ACCESS [25]. This can be demonstrated by comparing the performances of the ridge waveguide resonators with different materials, various gap sizes, and metal ridge heights. Table 3.1 displays the resonant frequency change of a ridge waveguide resonator. For NiCo as the structure material, the resonance frequency is slightly mitigated when

the height of the ridge waveguide, b, is increased and the same ratio of d/b and the footprint are maintained. In the case of Cu as structural material, the frequency change follows the same trend. However, the quality factor is increased by four times in the same situation (Table 3.2).

Table 3.1: Comparison of the resonance frequency of different ridge waveguide resonators (unit: GHz)

	$d = 4\mu m$	$d = 20\mu m$	$d = 30\mu m$
Material	$b = 112\mu m$	$b = 560\mu m$	$b = 840\mu m$
NiCo	26.75	25.71	24.81
Cu	26.64	25.78	24.88

Table 3.2: Comparison of the Quality factor of different ridge waveguide resonators

	$d = 4\mu m$	$d = 20\mu m$	$d = 30\mu m$
Material	$b = 112\mu m$	$b = 560\mu m$	$b = 840\mu m$
NiCo	70.5	221.57	265.85
Cu	170.63	554.52	655.16

The resonant frequency of the ridge waveguide filter is decreased by filling the gap between the top cover of the cavity wall and the surface of the metal ridge with dielectric material. For a quick concept proof, photoresist (AZ3312 from the Clariant Corp.) is spin coated on top of the fabricated ridge waveguide filter (Fig. 3-20). The measured response of the filter after spin coating photoresist is denoted in Fig. 3-21. The center frequency of the fabricated filter is decreased from 23 GHz to 13 GHz. Also, the measured filter response shows a quite large insertion loss. This is attributed to two factors: the mismatch of the input and output coupling and the loss from the photoresist.

One advantage of 3D micromachined filters over its planar counterparts is the relatively high power handling capability. For the micromachined ridged waveguide filter in this chapter, there are two potential power failure modes: one is an electric field breakdown in the gap of the ridged waveguide filter; and the other is a deformation of the top cover of the cavity due to the electrostatic force from the voltage potential across the gap of the ridged waveguide filter.

Fig. 3-22 illustrates the steps for an electrical field breakdown analysis. In general, a bandpass filer can be excited by terminating a matched load at the output port, when the

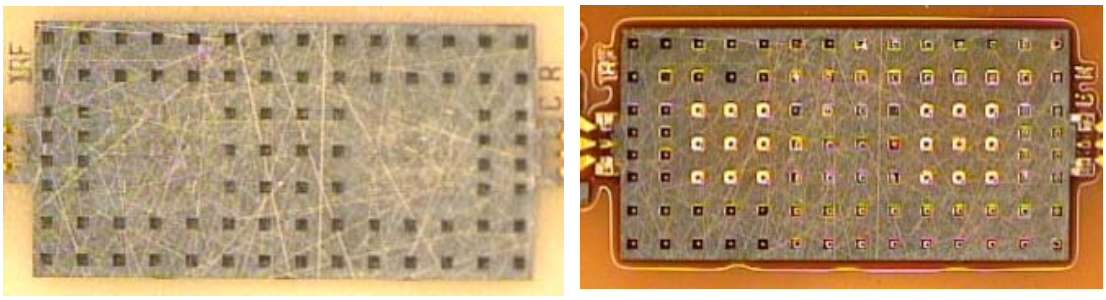

Figure 3-20: The fabricated ridge waveguide filter (a) without a photoresist coating and (b) with a photoresist coating.

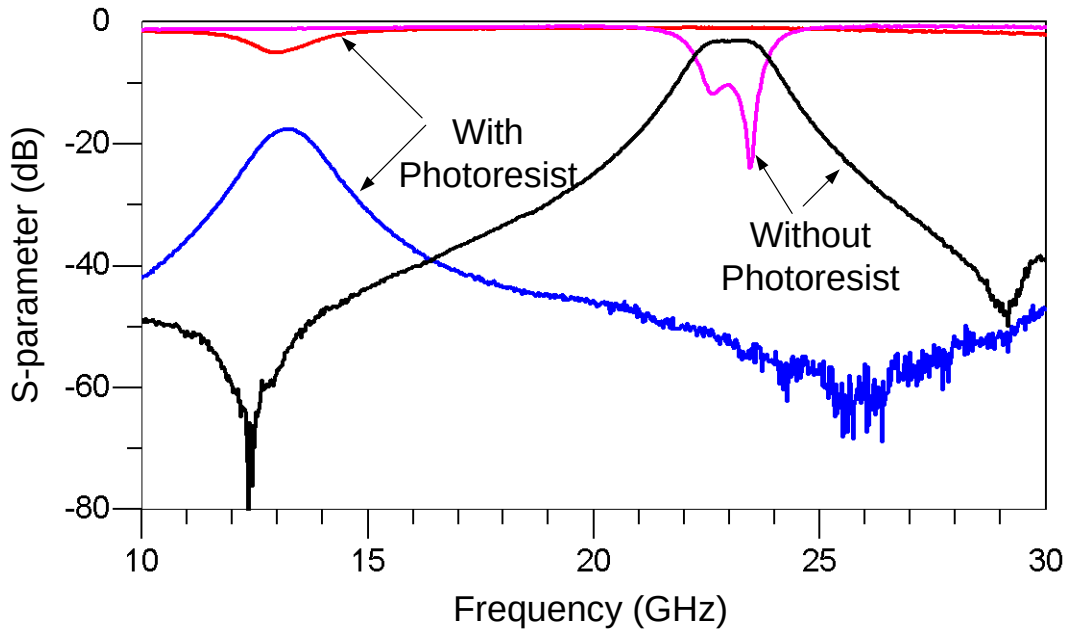

Figure 3-21: The comparison of the measured responses of the ridge waveguide filter with and without a photoresist coating.

input port is driven by a signal. The electric field inside each resonator is varied as a function of the frequency [98]. It is demonstrated that the time averaged stored energy in a passive network is proportional to the group delay of the network [99]. Therefore, the peak electric field of a bandpass filter over a frequency range can be found by plotting the group delay of the filter. In this case, the frequency point that has the highest electric field is 25.98 GHz (Fig. 3-22 (c)). For a ridged waveguide structure, most of the electric field is contained in the gap between the metal post and the cavity top cover (Fig. 3-22 (d)). The exact value of the peak electric field is read from the electric field distribution of a surface that intersects the ridged waveguide. Fig. 3-23 portrays the maximum electric field inside the ridged waveguide at different input power levels. At a normal atmospheric pressure, the breakdown strength of air is 2.28e6 V/m [100], so the maximum input power this ridged waveguide filter can handle should be less than 0.6 W, after some safety margins are included.

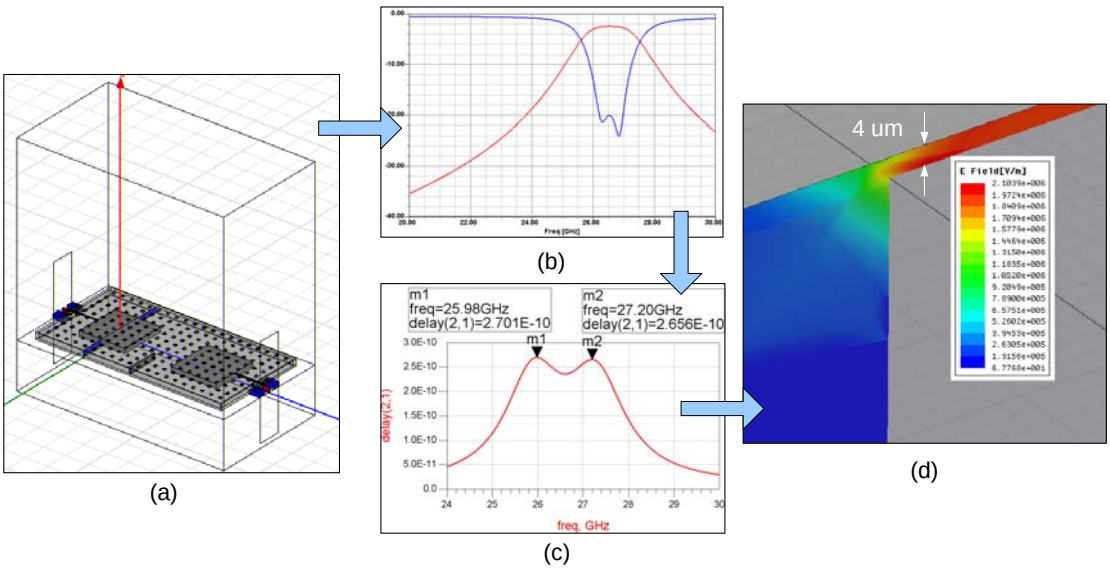

Figure 3-22: The power handling analysis procedure for a micromachined ridged waveguide filter.

When the input power of the filter is 0.6 W, the maximum electric field inside the ridged waveguide is 2.14e6 V/m. Consequently, the voltage potential across the 4- μm gap is 8.56 V. The electrostatic force on the top cover of the cavity, due the voltage potential across the ridge gap can be achieved by the following [101]:

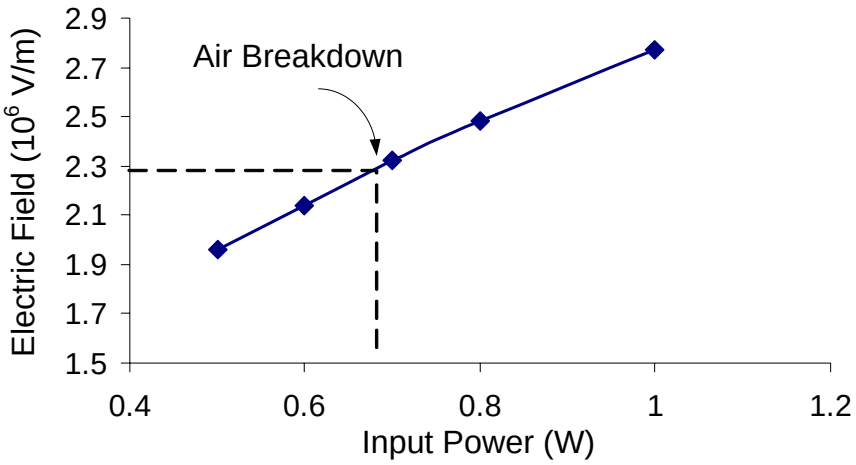

Figure 3-23: The maximum electric field of the micromachined ridged waveguide filter at different input power levels.

$$F_e = \frac{1}{2}\frac{\epsilon_o A}{g^2}V^2$$

where g is the gap between the cavity top cover and the metal ridge inside the cavity, V is the voltage potential cross the gap g, A is the area of the metal ridge, and the calculated electrostatic force, F_e , is 20.27 μN. The maximum deflection of the cavity top cover, caused by the electrostatic force, is predicted to be 4.9 nm in Coventorware$^{\text{TM}}$. The impact of the deflection of the cavity top cover on the resonant frequency of the ridged waveguide structure can be neglected when comparing with other factors.

3.4 Summary

Modern microfabrication techniques have the great potential to produce millimeter wave filters with an excellent performance. By embedding MEMS actuators into micromachined filters, the requirement for the tolerance of micromachining processes is reduced and the yield of micromachining process is improved. In this chapter, the feasibility of using MEMS actuators as tuning elements to fine tune micromachined filters is demonstrated first by a two-pole quasi dual-mode microstrip filter. The tuning range of the MEMS actuators is increased by adding

trenches underneath the gap between the filters and MEMS actuators. The proposed concept is also proved by a micromachined ridge waveguide filter with embedded thermal actuators as tuning elements. A 200-MHz tuning range is experimentally achieved, demonstrating the feasibility of constructing 3D micromachined filters with built-in MEMS tuning elements. By fully implementing the capabilities of EFAB^{TM} technology, the size of the micromachined ridge waveguide filter can be further decreased, and the quality factor can be improved.

Chapter 4

Tunable Dielectric Resonator Bandpass Filter

4.1 Introduction

Tunable filters with a fast tuning speed, high quality factor, and broad tuning range are key elements in reconfigurable systems. Tunable filters effectively utilize the frequency bandwidth, suppress interfering signals, and ease the requirements for the oscillator phase noise and dynamic range. In terms of the tuning mechanisms, most of the tunable filters in the literature are categorized as three types: magnetic tuning, electronic tuning, and mechanical tuning. Each tuning approach has a different impact on the performance of tunable filters, including insertion loss, tuning speed and tuning range.

Yttrium-iron-garnet (YIG) magnetically tunable filters have a wider tuning range and a higher quality factor; however, they are quite bulky and consume a considerable amount of DC power (typically from 0.75W to 3W) [30, 102]. Electronically tunable filters, realized by integrating solid-state or MEMS devices with microstrip or coplanar filters, offer a compact size, fast tuning speed, and wide tuning range [102, 32, 103, 104]. However, this type of tunable filter results in a high insertion loss due to the low quality factor of planar filters that are in the range from 200 to 400. The limited power handling capability of electronically tunable filters is another drawback. Often, mechanically tunable filters are realized in a waveguide cavity or dielectric resonator format, but are bulky and suitable for only low speed applications [105, 106].

Dielectric resonator filters have a much higher quality factor than microstrip or coplanar filters. The ability to integrate MEMS devices with dielectric resonators opens the door for the realization of MEMS-based high quality factor tunable filters. G. Panaitov et al. [8] have proposed the integration of the MEMS switch loaded slots with dielectric resonators to achieve tunability. However, a limited tuning range has been achieved (only a few MHz).

In this chapter, a novel approach for constructing a tunable dielectric resonator bandpass filter by using MEMS technology is described. A high quality factor tunable bandpass filter with a wide tuning range and moderate tuning speed can then be attained. Tuning disks, powered by MEMS thermal actuators, are embedded in the dielectric resonator filter to serve as tuning elements. The tunability is attained by perturbing the electrical fields with the nearby tuning elements. A wide tuning range of the dielectric resonator filter that operates at the TE_{01} mode is accomplished with the assistance of the large deflection of the tuning disk, provided by MEMS thermal actuators. Moreover, since the MEMS tuning elements are not in the main electrical path, the power handling capability of this proposed design can be maintained at a relatively high level. Additionally, the tuning speed of the new tunable filter is much higher than that of any traditional mechanically tunable filter due to the low mass and the fast response to the electrical control signal of the MEMS tuning elements. In order to prove the proposed concept, a three-pole tunable dielectric resonator bandpass filter is designed and constructed. Three MEMS tuning elements with large deflections are embedded into the experimental dielectric resonator filter.

4.2 Design and Analysis of Tunable Dielectric Resonators

The proposed tuning mechanism of the tunable dielectric resonator filter includes a dielectric resonator with an operating mode of TE_{01}, a tuning disk, and MEMS thermal actuators that connect the tuning disk to the cavity wall. All the components are contained in a metallic cavity. A cross section of the proposed tuning mechanism is exhibited in Fig. 4-1.

The concept of the newly developed tuning mechanism is to use MEMS thermal actuators and tuning disks to imitate the tuning screws in conventional, mechanically tunable filters [105]. The tunability of the proposed structure is achieved by moving the tuning disk along the Z axis

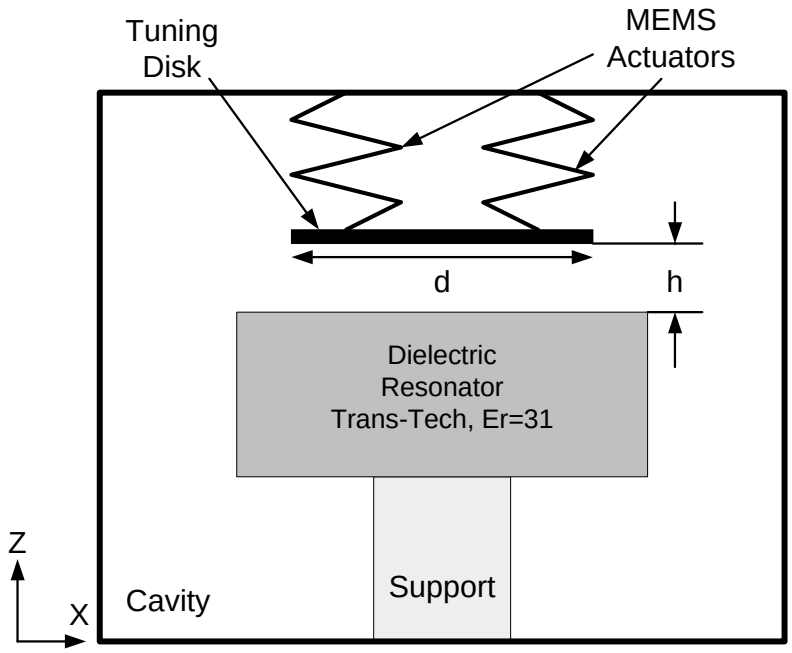

Figure 4-1: Schematic of the proposed tuning structure.

with the use of MEMS thermal actuators. Initially, the MEMS thermal actuators are in the relaxation state, and the tuning disk is at the closest position to the dielectric resonator, that is, the value of tuning gap h is at a minimum. In this state, the MEMS tuning elements have the most impact on the resonant frequency of the dielectric resonator. When a DC voltage is applied to the MEMS actuators, they pull the tuning disks from the dielectric resonator, and the resonant frequency begins to decrease. A comparison of the magnitude of the electrical field of the dielectric resonator with and without the tuning disk is depicted in Fig. 4-2. The substantial difference indicates the impact of the tuning disk on the resonant frequency of the dielectric resonator.

There are several constraints in developing the proposed MEMS tuning elements. To select the optimal electrical and mechanical configurations for the proposed design, HFSS$^{\mathrm{TM}}$ software is employed to determine the optimum tuning disk size for a maximum tuning range and a maximum quality factor. The most important design parameters of this novel structure are tuning gap h and the diameter of tuning disk d, since they have the most impact on the tuning range and quality factor of the dielectric resonator. Two sets of simulations are performed to

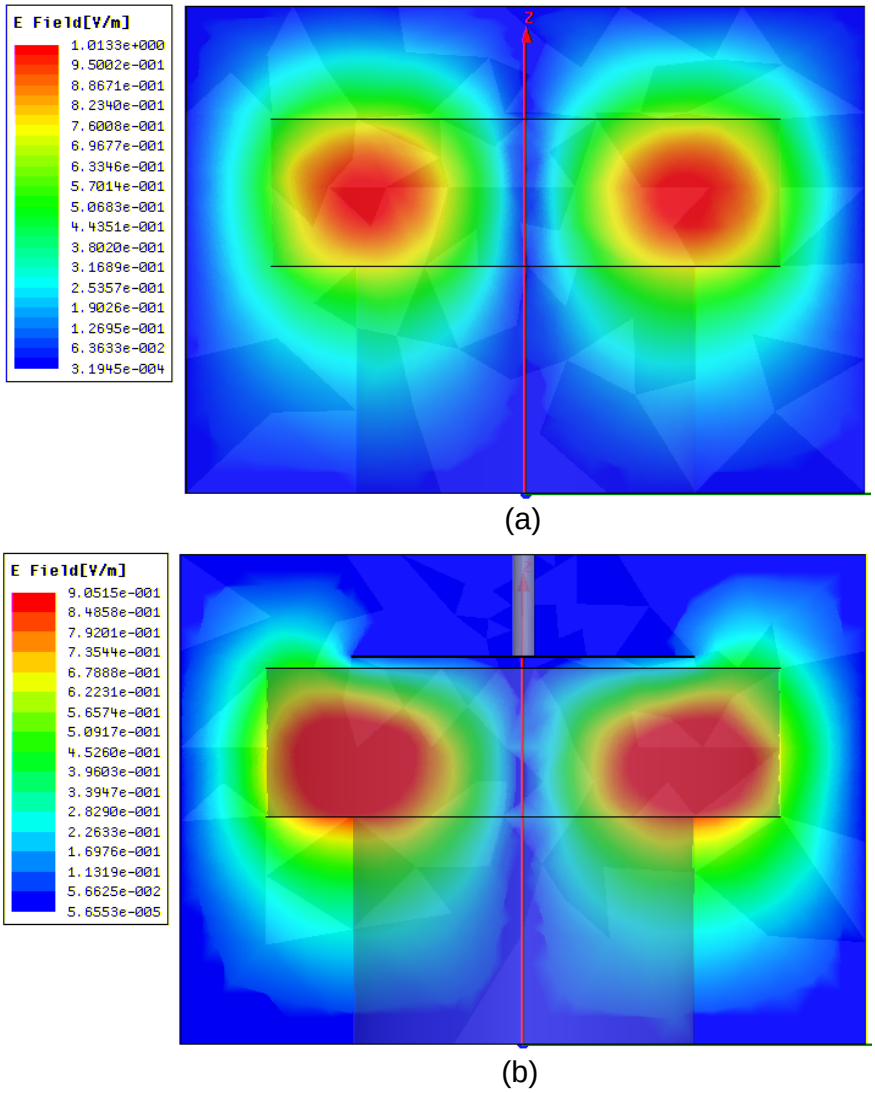

Figure 4-2: A cross section of the electrical field of the dielectric resonator: (a) without the tuning element and (b) with the tuning element.

study the effects of these two parameters. Fig. 4-3 illustrates the variation in the frequency shift and quality factor as a function of the tuning gap, when the diameter of the tuning disk is fixed.

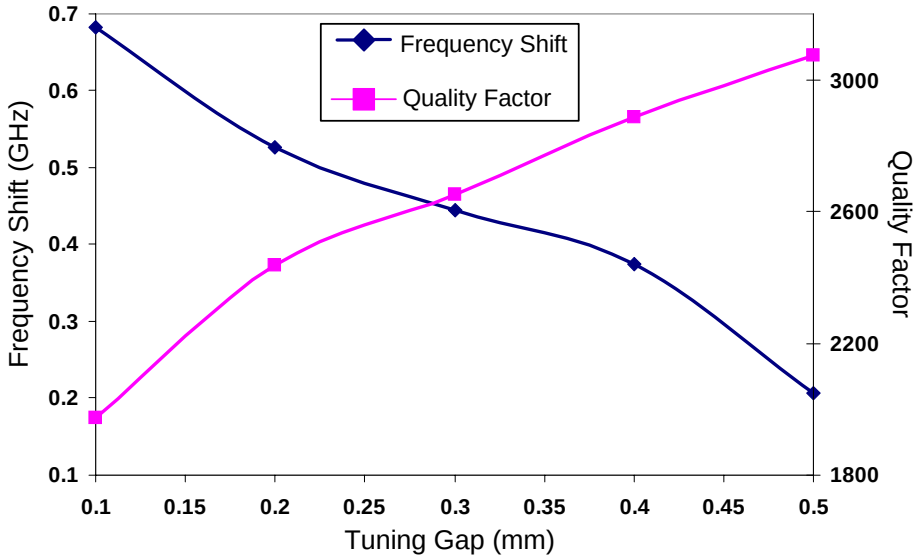

Figure 4-3: Frequency shift and Q factor as a function of the tuning gap when the tuning disk diameter is fixed.

A 2-mm diameter circular tuning disk, made of 2-μm gold and 3.5-μm polysilicon, is employed to construct the simulation model. For simplicity, the zigzag configuration of MEMS thermal actuators are replaced by a gold rod configuration. With the decrease in the tuning gap, the frequency shift is increased, whereas the Q factor of the dielectric resonator is decreased. In view of Fig. 4-3, it can be seen that at a tuning gap of 0.5 mm, the tuning structure can achieve a frequency shift of only 200 MHz. Based on the cavity size and the maximum deflection of the MEMS thermal actuators, the theoretical minimum tuning gap that can be achieved is approximately 0.1 mm. When the tuning disk is at this location, the proposed structure exhibits a maximum frequency shift of about 700 MHz. However, the quality factor is decreased to 2000, about 45% lower than that of the dielectric resonator without the presence of the tuning elements. The loss is mainly attributed to the lossy polysilicon. The novel structure exhibits a good tuning linearity, one of the most important criteria for tunable filters [30]. By

balancing the tuning range and quality factor, for a 2-mm diameter tuning disk, the optimal operating range of the proposed design in terms of tuning gap should be higher than 0.2 mm, which corresponds to a tuning range of approximately 500 MHz.

The focus of the second set of simulations is to investigate the effect of the tuning disk size on the tuning range and quality factor of the proposed structure. In terms of the tuning disk size, two groups of simulation results are compared: one group is generated with a 0.1 mm tuning gap, and the other one, with a 0.2 mm tuning gap. As indicated in Fig. 4-4, the larger the tuning disk is, the wider the tuning range is when the tuning disk is moved the same distance. The quality factor of the proposed structure starts to decrease, when the diameter of the tuning disk is increased. However, the quality factor is constant at 1800, when the diameter of the tuning disk is larger than 3 mm. A tuning disk with a 4-mm diameter size seems to perform better than smaller tuning disks, since the 4-mm disk has more than a 400% increase in the tuning range with a only 50% decrease in the quality factor. However, such large tuning disks are subject to other design issues such as mechanical stability and warpage. After a careful consideration of the overall performance of the proposed MEMS tuning elements (the mechanical and RF properties), tuning disks with a 2 and 3-mm diameter are chosen for this study.

Fig. 5 denotes the HFSS simulation results of a three-pole tunable dielectric resonator filter. Circular tuning disks of a 3-mm diameter are employed in the simulation model. With a deflection of 0.7 mm provided by the MEMS tuning elements, the filter can be continuously tuned from 15.65 GHz to as high as 16.45 GHz.

4.3 MEMS Tuning Element Design

In the proposed tunable dielectric resonator filter, the MEMS actuator is one of the key elements. In order to achieve a wide tuning range, it is essential to design a MEMS actuator that can generate enough force to lift a relatively large tuning disk, as well as generate a large deflection. In addition, a low actuation voltage and fast tuning speed are desirable.

MEMS thermal actuators are good candidates to meet such requirements. An out-of-plane rotation of a 400 μm x 2500 μm x 2 μm plate, produced by MEMS thermal actuators, is

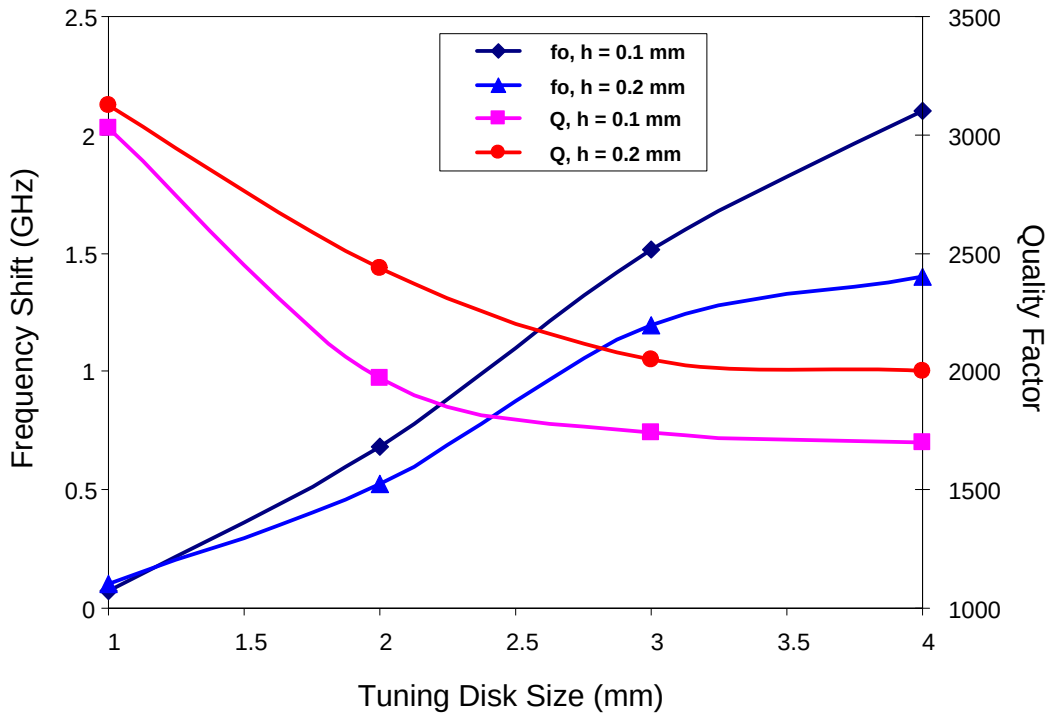

Figure 4-4: The frequency shift and Q factor as a function of the tuning disk diameter when the tuning gap is 0.1 and 0.2 mm.

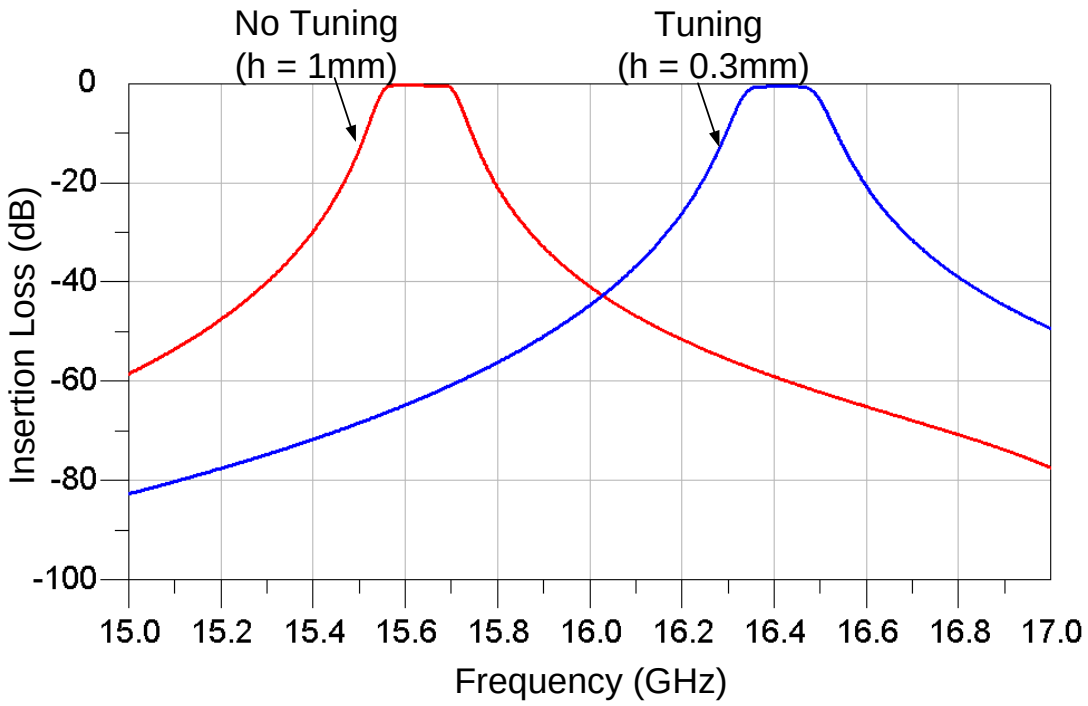

Figure 4-5: The HFSS simulation results of a three-pole dielectric resonator filter tuned at different frequencies (without loss)

successfully demonstrated [107]. The actuation voltage is less than 10 V and a 90-degree rotation is achieved within 1 millisecond. The basic unit for constructing the MEMS thermal actuator in [107] is a bimorph of gold and polysilicon. After the thermal plastic deformation assembly treatment [108], the bimorph unit deflects because of the difference of the thermal expansion coefficient between gold and polysilicon. To achieve a large out-of-plane rotation, several units are connected in series, requiring a large footprint for a single actuator. This, though, is not desirable for the proposed design, since lifting each MEMS tuning disk requires at least two MEMS thermal actuators.

In this thesis, the concept of the thermal plastic deformation assembly is adopted to design the MEMS tuning element with a vertical displacement. Since a linear motion that is perpendicular to the substrate is required for the newly devised tunable dielectric resonator filter, bimorphs of gold and polysilicon are connected by a passive polysilicon beam in a zigzag manner instead of in series (Fig. 4-6). After the thermal plastic deformation assembly treatment, each bimorph unit has a small deflection in the Z direction; meanwhile, the passive polysilicon beam keeps straight since it is composed of only one material. The straight passive polysilicon beam can transfer a small deflection of one bimorph unit to an adjacent unit. A large deflection can be achieved by accumulating each bimorph's small deflection through passive polysilicon beams. When several bimorphs are connected by passive polysilicon beams in a zigzag configuration, the deflection is accumulated in only the Z direction. As shown in Fig. 4-6 (a), when a MEMS rectangular disk is lifted by the two proposed MEMS actuators, the new MEMS thermal actuator demonstrates a negligible deflection in the X and the Y direction and a maximum deflection in the Z direction (Fig. 4-6 (b)). The payload of the MEMS thermal actuators in Fig. 4-6 is 1500 μm x 300 μm x 4.75 μm. It is confirmed that four such MEMS thermal actuators can lift a 3000 μm x 3000 μm x 2 μm plate more than 1 mm in the Z direction (Fig. 4-7). Each MEMS thermal actuator in this particular design contains four bimorph units with dimensions of 100 μm x 700 μm.

The maximum deflection of the proposed MEMS thermal actuator depends on the length of each bimorph unit and the number of the bimorph units used in the design. Obviously, the length of the bimorph unit and the number of the bimorph units is proportional to the total deflection of the design. However, the increase of the bimorph unit length and the number of the

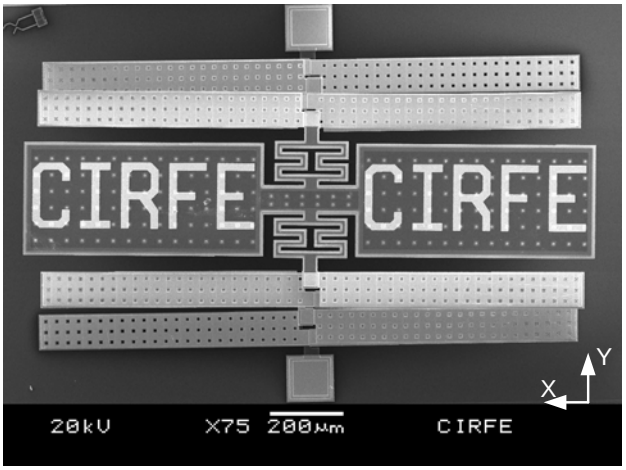

(a)

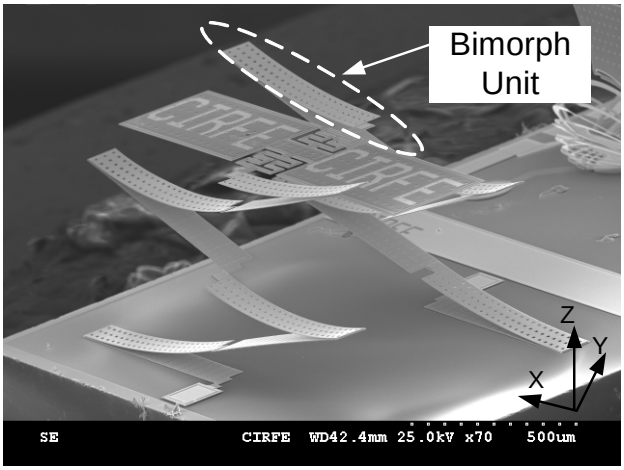

(b)

Figure 4-6: A MEMS rectangular disk lifted by two proposed MEMS thermal actuator: (a) a top view and (b) an isotropic view.

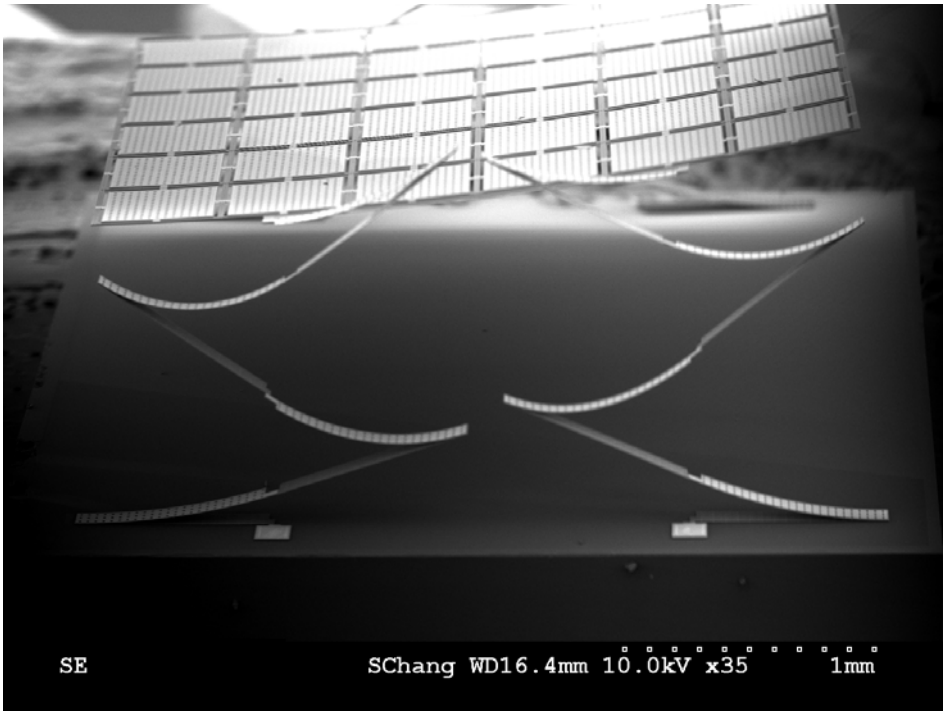

Figure 4-7: MEMS tuning element with a 3-mm square disk lifted by the four proposed MEMS actuators.

bimorph units decreases the stiffness of the entire structure, affecting the actuator's capability to lift a large tuning disk. As a result, these two parameters must be carefully selected, according to the size of the tuning disk and the maximum deflection required. Fig. 4-8 portrays a side view of one of the proposed MEMS thermal actuators. By using six bimorph units, each with dimensions of 700 μm x 100 μm, a deflection of 1200 μm is obtained. The inset in Fig. 4-8 is an isotropic view of the thermal actuator.

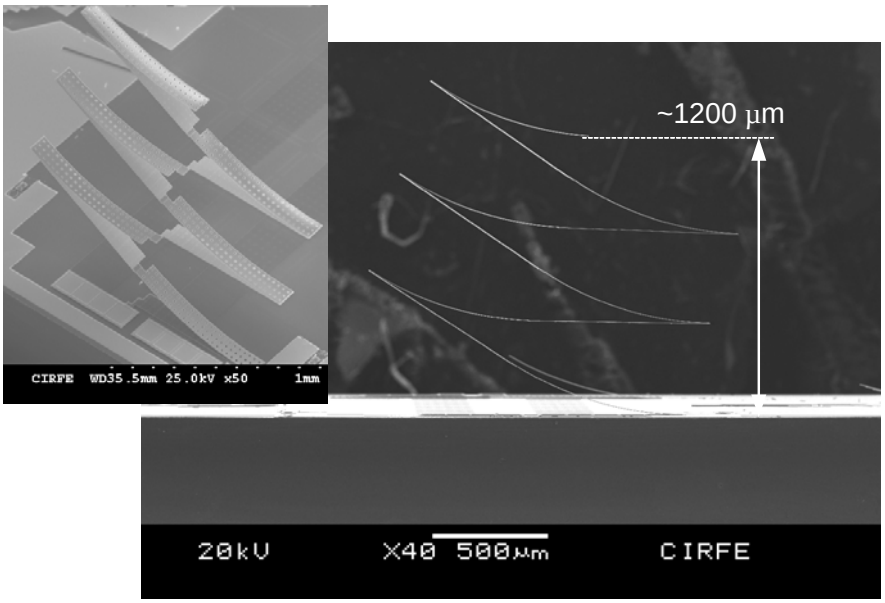

Figure 4-8: A side view of the proposed MEMS thermal actuator.

First, a MEMS tuning element with four of this novel MEMS thermal actuators and one 3-mm diameter circular tuning disk is constructed. However, after the treatment of thermal plastic deformation assembly, the tuning disk is subjected to large warpage due to the mismatch between the thermal expansion coefficients of the gold and polysilicon as shown in Fig. 4-9 (a). This warpage decreases the effective deflection of the thermal actuators, which results in a narrower tuning range. In place of a solid circular disk, a hexagonal plate is employed to solve the warpage problem. As illustrated in Fig. 4-9 (b), the large hexagonal plate consists of many small hexagonal plates. Each plate consists of six equilateral triangles that are connected by short beams. The small air gap between the triangles can significantly reduce the warpage of the tuning disk. The dimensions of the small air gaps among the triangles are only a fraction of the

wavelength at the filter's centre frequency and do not affect the size of the tuning disk. The size of this hexagonal tuning disk is approximately 2000 μm x 2000 μm x 4.75 μm. The resistance between two DC pads is 3.35 KΩ. For a single MEMS tuning element, less than 0.1 W DC power is needed to achieve the maximum deflection. Therefore, the total DC power consumption of the tunable filter is less than 0.3 W over the entire tuning range. Latching mechanisms can be embedded in the MEMS tuning elements to further reduce the power consumption, increase the resistance to the mechanical vibration and temperature variation.

4.4 Experimental Results

To facilitate the assembly of the MEMS tuning elements, the filter cavity of the proposed design is manufactured as two detached parts: the top cover in Fig. 4-10 (a) and the body in Fig. 4-10 (b). These two parts are gold plated to decrease the metallic loss from the metal cavity. Dielectric resonators are assembled with the body and the MEMS tuning elements are integrated on the top cover. Each MEMS tuning element is connected to two DC feed-through pins for applying the control voltage. A synchronously tuning method is employed to tune the proposed filter. All the tuning elements are connected to one control signal to ensure they have the same deflection; that is, the same loading effect on the dielectric resonators. In addition, this configuration also allows the tuning elements to be independently controlled. Therefore, the nonsynchronous tuning of each resonator can then be applied to attain a wider tuning range, a better return loss, and a constant absolute bandwidth within the tuning range of the tunable dielectric resonator filter. The gold coating of the MEMS actuators is instrumental to reduce the loss from the polysilicon structure layer and the silicon substrate. A few mechanical tuning screws are also included in the tunable filter design to compensate for the machining tolerance and variation of material properties.

The measurement is carried out by a vector network analyzer (HP8722ES). SOLT (Short, Open, Load and Thru) calibration is performed before the measurements. A comparison of the simulated and measured results of the proposed dielectric resonator filter is illustrated in Fig. 4-11. From the simulated results, it is predicted that the proposed filter has a centre frequency of 15.6 GHz with a relative bandwidth of 1%. The insertion loss at the mid band is

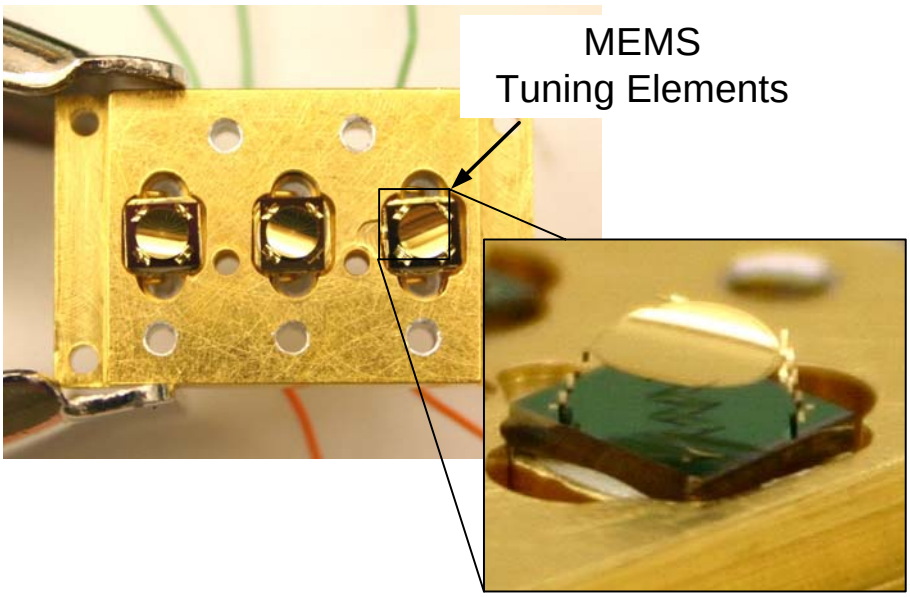

(a)

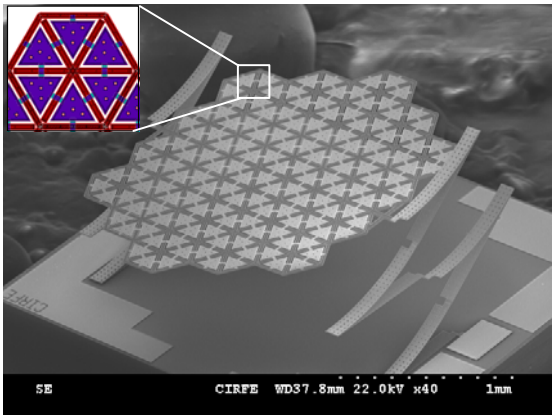

(b)

Figure 4-9: The MEMS tuning elements: (a) a solid circular disk with warpage, and (b) a hexagonal tuning disk without warpage.

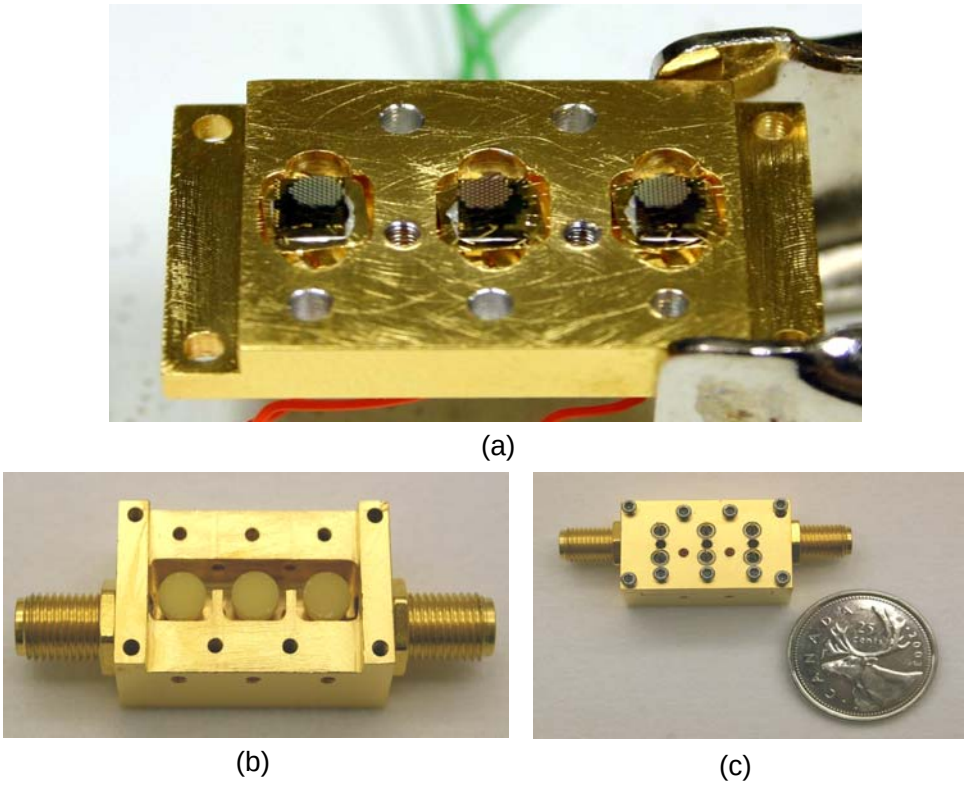

Figure 4-10: The proposed three-pole tunable dielectric resonator filter: (a) the top cover with the MEMS tuning elements (b) the filter body, and (c) the assembled filter.

approximately 0.5 dB. The measured response of the fabricated filter has a slightly lower centre frequency. This minor difference can be attributed to the machining and assembly errors, and the approximation of the material properties and the dimensional tolerances of the dielectric resonators. The insertion loss of the measured results at the mid band is approximately 1.5 dB, which corresponds to an unloaded quality factor of about 1300. The discrepancy between the insertion loss of the simulated results and that of the measured results is partially due to the discontinuity on the top cover, since there are small gaps between the MEMS tuning elements and the metal body, and the small holes required for the DC feed-through pins. Moreover, the lossy assembly materials such as the dielectric resonator support structures also contribute to the higher insertion loss.

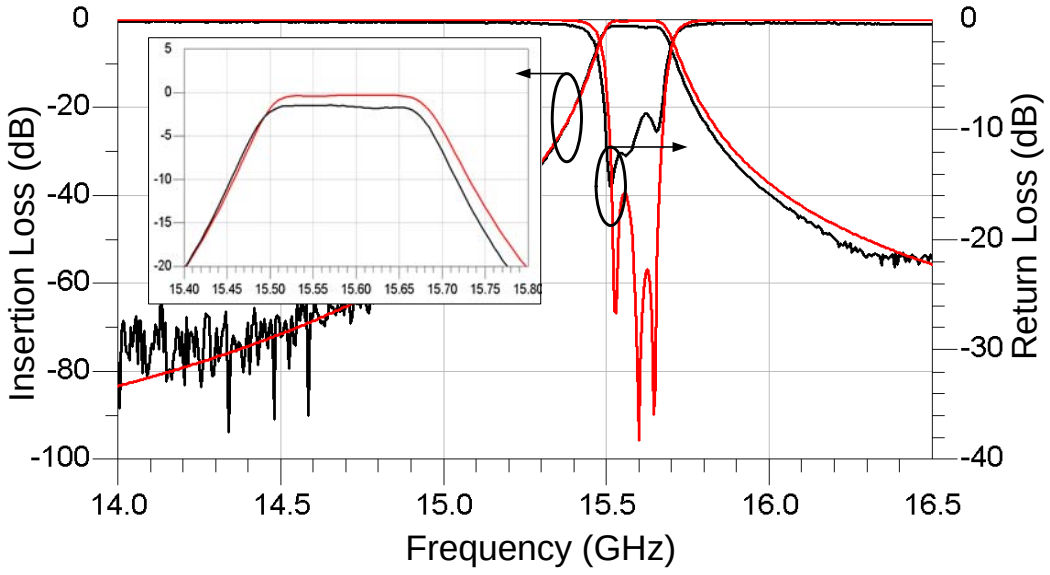

Figure 4-11: A comparison of the simulated and measured results of the proposed three-pole dielectric tunable filter.

Fig. 4-12 illustrates the measured unloaded quality factor values of a single dielectric resonator as it is tuned by the newly devised approach. As shown in Fig. 4-12, the dielectric resonator can be tuned from 15.62 GHz to 15.86 GHz. The extracted unloaded quality factor varies between 1638 and 421 over this tuning range. The method used to extract the unloaded quality factor can be found in [109].

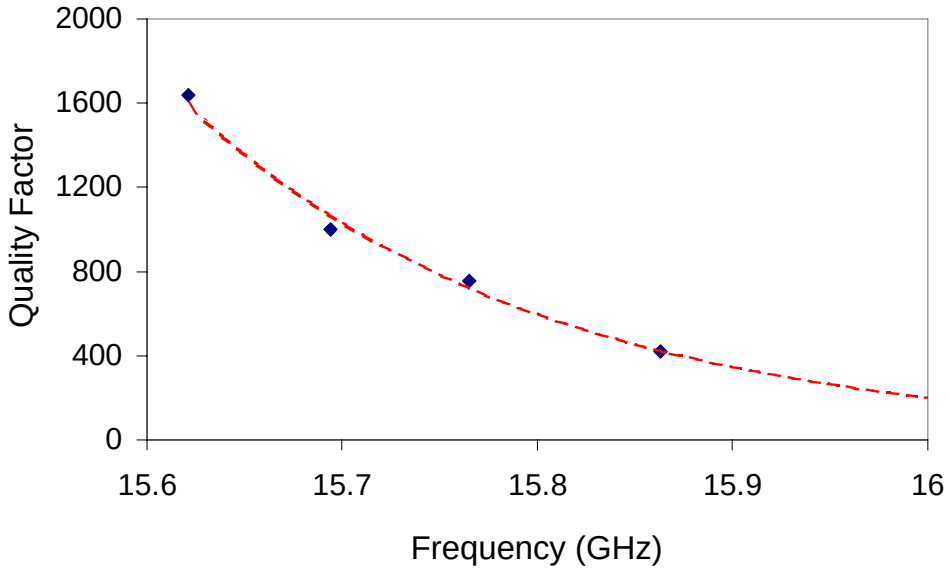

Figure 4-12: The measured results of a single dielectric resonator tuned at different resonant frequencies.

The measured results for the insertion loss and the return loss responses of the proposed three-pole tunable dielectric resonator bandpass filter are presented in Fig. 4-13. The filter's centre frequency is synchronously tuned from 15.6 GHz to 16.0 GHz. The mid band insertion loss of the filter increases from 1.5 dB to 4.5 dB, when the filter is tuned from 15.6 GHz to 16.0 GHz.

4.5 Discussion

There is a 15-MHz variation in the bandwidth during the entire tuning range. Less variation in the bandwidth can be achieved by utilizing nonsynchronously tuning where the resonators are tuned at different rates [110, 111]. However, it is believed that the main cause for this variation is the lack of the input and output coupling of the proposed filter, which is fixed during the entire tuning range. To achieve a constant bandwidth for a wide tuning range, the tuning mechanisms must be implemented for the input and output coupling as well.

The simulation results reveal that the proposed tunable filter exhibits an unloaded quality

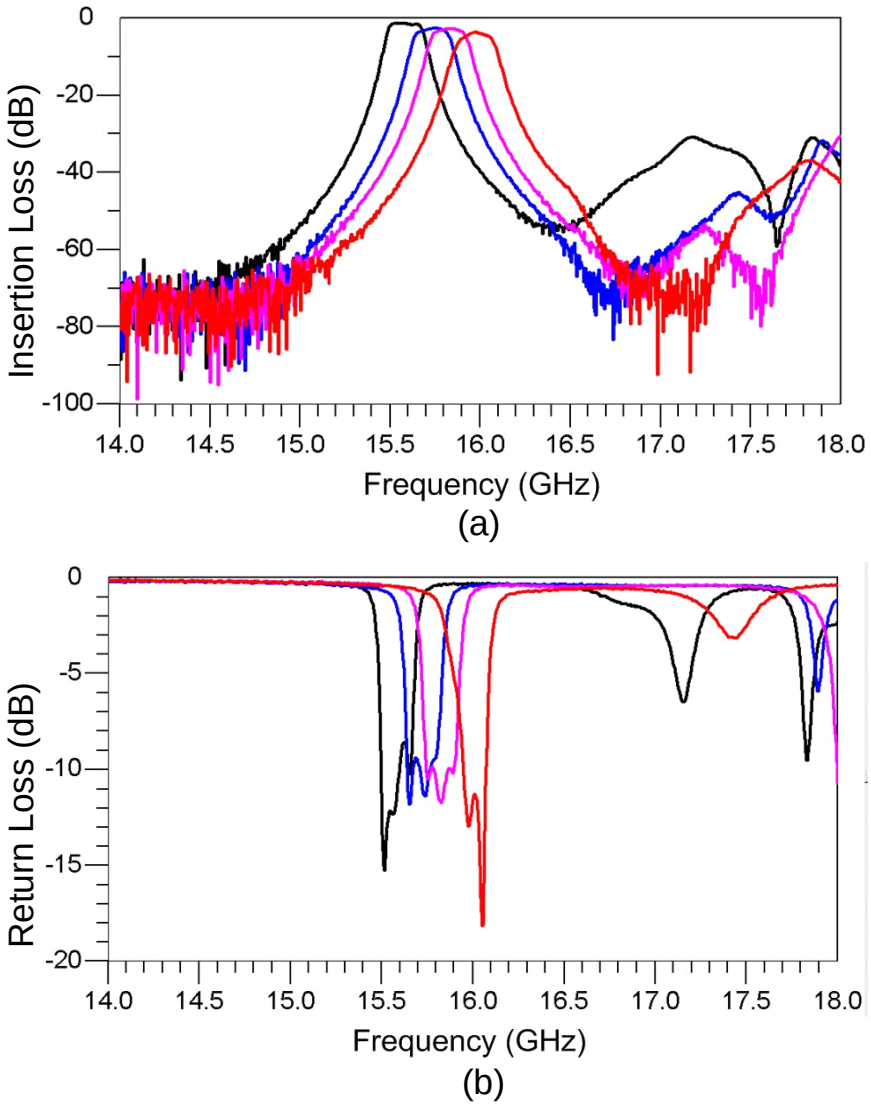

Figure 4-13: A comparison of the measured results of the proposed tunable dielectric resonator filter at different tuning states.

factor as high as 1500 over a 400 MHz tuning range when only the losses from the dielectric resonators, metal cavity, and MEMS tuning disks are considered. This measured high insertion loss is attributed to several factors such as the assembly procedure and lossy materials (epoxy, stainless tuning screws, and so on) used to construct the prototype filter. As mentioned earlier, the MEMS actuators are partially made of polysilicon, which is very lossy at high frequencies. This also contributes to the high insertion loss of the filter. To further improve the insertion loss, amorphous silicon can be employed to replace the polysilicon since amorphous silicon has almost the same mechanical properties as polysilicon and a much better electrical performance than polysilicon [112].

For high power applications, dielectric resonator bandpass filters are favoured. To examine the impact of the MEMS tuning elements on the power handling capability of the proposed tunable dielectric resonator filter, a 3D model, shown in Fig. 4-14 is constructed. Two extra surfaces (cross section 1 and 2) are defined to determine the maximum electric field inside the filter cavity when the filter is tuned at various frequencies. When the input power level is fixed, the maximum electric field inside the filter cavity is proportional to the tuning gap between the MEMS tuning disks and dielectric resonators. The maximum electric field is found to be 3.17e4 V/m, when the tuning gap is 1mm and the input power is 1W. To achieve the breakdown strength of air under the normal atmospheric pressure, more than a 5 KW input power is needed, which is far beyond the power level required for practical applications [100].

Besides the air breakdown failure mode, another failure mode can occur. It is attributed to the deflection of the MEMS tuning disks caused by the potential difference across the tuning gap. This electrostatic force can pull the tuning disks towards the dielectric resonator, which in turn, decrease the filter tuning range. The same procedure, described in Chapter 3, is followed to calculate the electrostatic force. It is found that when the input power is in the range of a few KW, the maximum electrostatic force is a few tens of μN , which is compatible with the force generated by MEMS thermal actuators. So, the electrostatic force generated by the potential across the tuning gap can be canceled by the force produced by the MEMS thermal actuators. Therefore, MEMS tuning elements does not have an impacts on the power handling capability of the proposed tunable dielectric resonator bandpass filter.

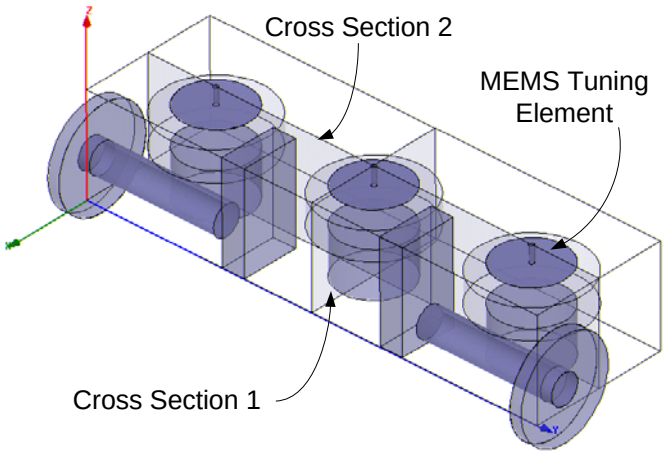

Figure 4-14: The 3D model used for the power handling analysis.

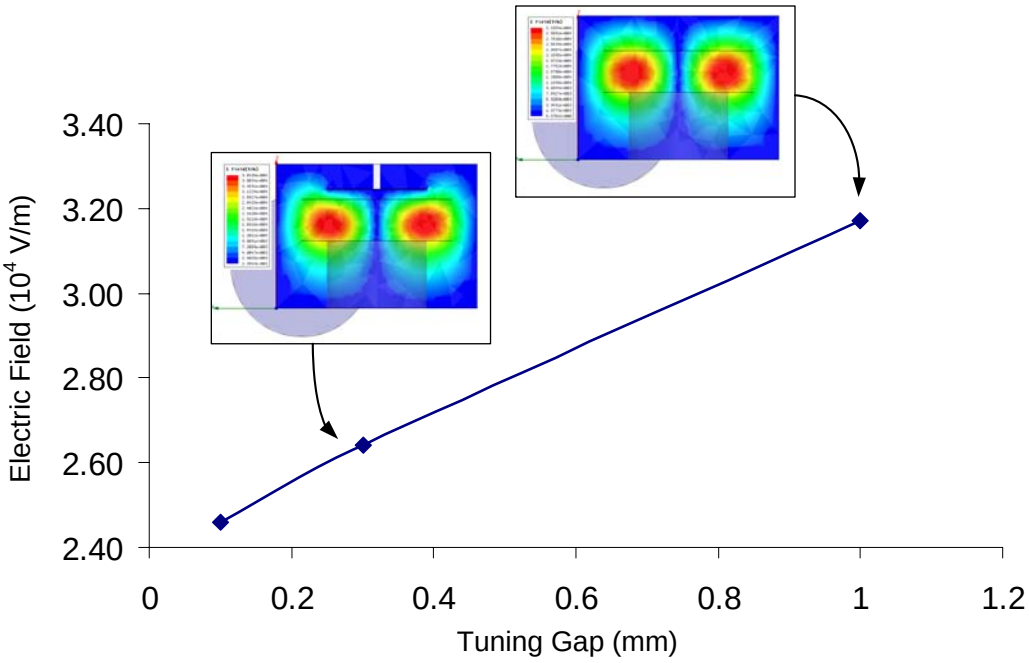

Figure 4-15: The maximum electric field inside the filter cavity vs. the tuning gap between the DR resonator and MEMS tuning disk.

4.6 Summary

In this chapter, a novel approach to construct tunable dielectric resonator filters has been presented and discussed in detail. To the best of the authors' knowledge, this is the first time that MEMS tuning elements have been applied to demonstrate a high quality factor tunable dielectric resonator filter with a wide tuning range. By using MEMS tuning elements, the size of the tunable dielectric resonator filter has been significantly reduced; in addition, the tuning speed has been dramatically increased. The integration of MEMS with dielectric resonators can lead to the realization of miniature tunable filters with a reasonably high quality factor. A three-pole tunable dielectric resonator bandpass filter has been designed, fabricated and tested. This K_u band filter with a relative bandwidth of 1% has achieved a 400-MHz tuning range. The measured results have proved the feasibility of the proposed concept. With the superior performance of the newly developed MEMS tuning element, the proposed approach can be used to construct X, K_u, and K bands tunable filters with a relatively wide tuning range.

Chapter 5

Tunable Bandstop Filter with Tri-Layer MEMS Tuning Elements

5.1 Introduction

Tunable bandstop filters with a compact size, superior performance and low cost are crucial for such applications as communication transceivers, radar and measuring instruments [113, 114]. The filters effectively reduce the complexity of overall system design and relax the requirements for the bandpass filter selectivity and the oscillator phase noise.

In the literature, various tuning mechanisms have been applied to construct tunable bandstop filters. Each tuning method shows different impacts on the tunable bandstop filters in terms of size, performance, and cost. Tunable bandstop filters with wide tuning range and high quality factor have been demonstrated by employing magnetic materials as tuning elements [11, 59] . However, such filters require an external magnetic source that is bulky and consume a considerable amount of DC power. These two drawbacks are generally at odds with the demand for miniaturization and low costs. Semiconductor varactor tuned bandstop filters have attracted attention due to their fast tuning speed, compact size, and deep rejection [114, 115]. But, the high nonlinearity, associated with solid-state devices, cause serious concerns. Usually, varactor tuned bandstop filters require the post assembly of the varactors with passive circuit elements, significantly increasing the cost. With the development of micromachining techniques, MEMS technology has been extensively employed in tunable lowpass and bandpass filter designs to

achieve a high linearity, light weight, and low cost [116, 117]. More recently, Karim, *et al.* have proposed a MEMS-based tunable bandstop filter for wireless sensor networks [118]. The tunability results from actuating micromachined switches between the CPW signal line and the ground plane. To achieve a reasonable tuning range, sixteen MEMS switches are needed for a three-pole filter, which requires a large footprint and introduces reliability issues. The failure of any MEMS switch degrades the filter's performance.

In this chapter, a novel approach for constructing a tunable bandstop filter in MEMS technology is proposed. In addition, a unique surface microfabrication process is developed to facilitate the monolithic integration of MEMS tuning elements in a bandstop filter. Microstrip line with slots etched in the ground plane is the basic configuration for the bandstop filter. MEMS tuning elements, consisting of a tri-layer thermal actuator and a tuning plate (metal-dielectric-metal), are fabricated above the slots. Each slot resonator requires only one tuning element. The tunability is achieved by actuating tuning elements to change the loading effect of slot resonators in the ground plane. This tri-layer structure allows the DC bias circuit to be separated from the RF circuit, simplifying the RF circuit design. To prove the proposed concept, a three-pole tunable bandstop filter is designed, simulated, and tested. The measured results are in good agreement with the simulation results, demonstrating a remarkable tunable bandstop filter with a compact size and wide tuning range.

5.2 Design of a Tunable Bandstop Filter

5.2.1 Proposed Tuning Mechanism

Typically, the resonant frequency of a slot resonator is determined by the width and length of the resonator in the ground plane. However, it is difficult to change the slot width after fabrication; therefore, changing the slot length is a more effective way to tune the resonant frequency of the slot resonator. Commercial MEMS switches have been employed to short-circuit the slots in the ground plane to effectively decrease the length of the slots [116]. The tunability depends on the number of switches used on each slot resonator, and only discrete tuning can be achieved. To realize continuous tunability with fewer components, the varactors can be utilized to replace the switches. The effective length of the slot resonator is increased when the capacitance of the

varactors is increased. Unlike the switch tuning method, the varactor tuning method means a continuous tunability and the tuning range depends on only the tuning ratio of the varactors.

In this thesis, the varactor tuning concept is adopted. Instead of post assembling the discrete varactors to the bandstop filter, a novel surface microfabrication process is developed to monolithically integrate MEMS tuning elements with the bandstop filter on the same wafer. The proposed tuning structure is shown in Fig. 5-1, where the resonating unit is a 50-Ω microstrip line with a zigzag slot etched in the ground plane. Tunability is accomplished by varying the distance between the tuning plate and the ground plane. A tuning element, composed of a tuning plate and an actuator, is placed on top of the slot to realize the tuning function. When a DC voltage is applied to the actuator, it moves the tuning plate toward the ground plane to disturb the electric field of the slot resonator, which in turn, shifts the resonant frequency of the resonator.

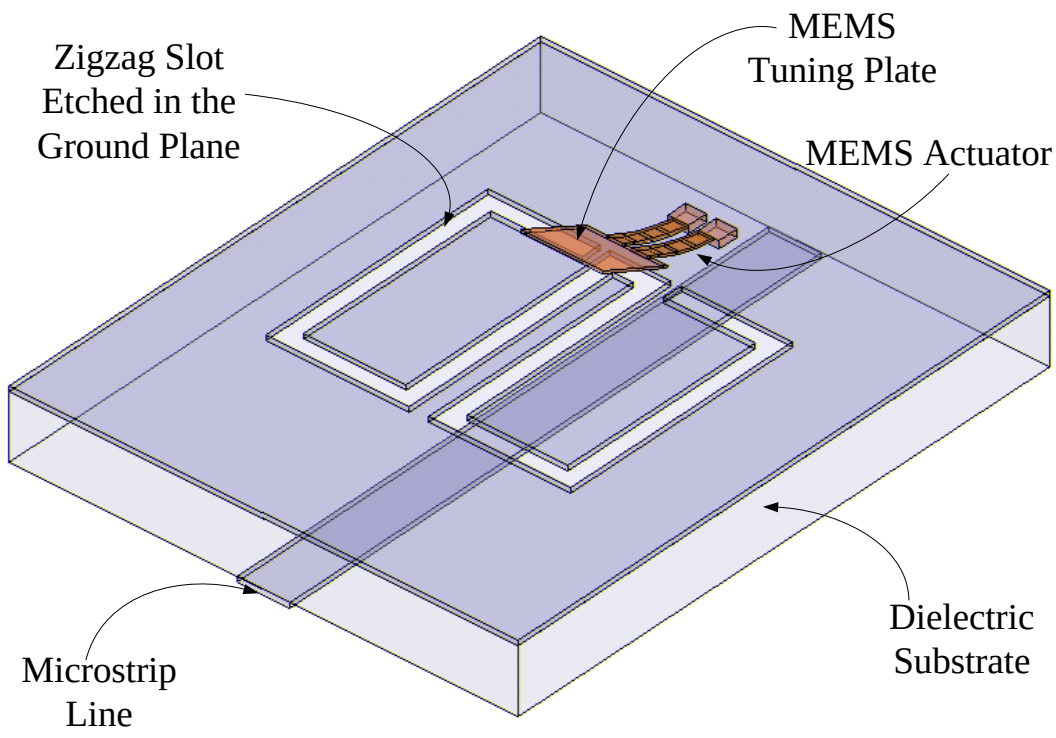

Figure 5-1: A schematic view of the proposed tuning concept.

For the maximum tuning range, the tuning element is placed where the highest electric field

is. Fig. 5-2 reflects the variations of the resonant frequency of the slot resonator at different tuning gaps. When the tuning gap is larger than 50 μm, the tuning structure has a negligible effect on the resonant frequency of the slot resonator. However, when the tuning gap is changed from 15 μm to 1 μm, the resonant frequency of the slot resonator can be changed dramatically. This indicates that a MEMS actuator that is capable of providing up to a 50-μm deflection can effectively tune the newly designed resonator.

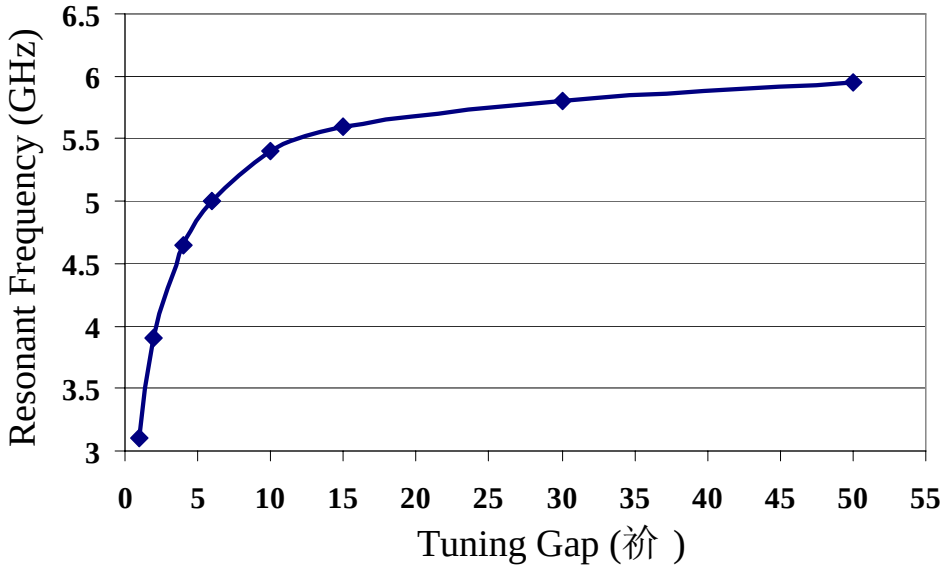

Figure 5-2: The simulation results of the resonant frequency of the zigzag slot resonator with different tuning gaps.

To verify the newly devised tuning concept, a three-pole tunable bandstop filter, embedded with the proposed tuning mechanism, is designed and simulated. Fig. 5-3 (a) provides a layout of the tunable bandstop filter. The slot resonators are a quarter of a wavelength away from each other which is 5.103mm in this case. The thermal actuators used for the tuning elements are 0.8 mm long and attached to tuning plates of 0.5mm x 0.5mm. Fig. 5-3 (b) illustrates the simulated results of the proposed tunable bandstop filter when the gap between tuning elements and ground plane is varied from 50-μm (simulation e) to 1-μm (simulation a).

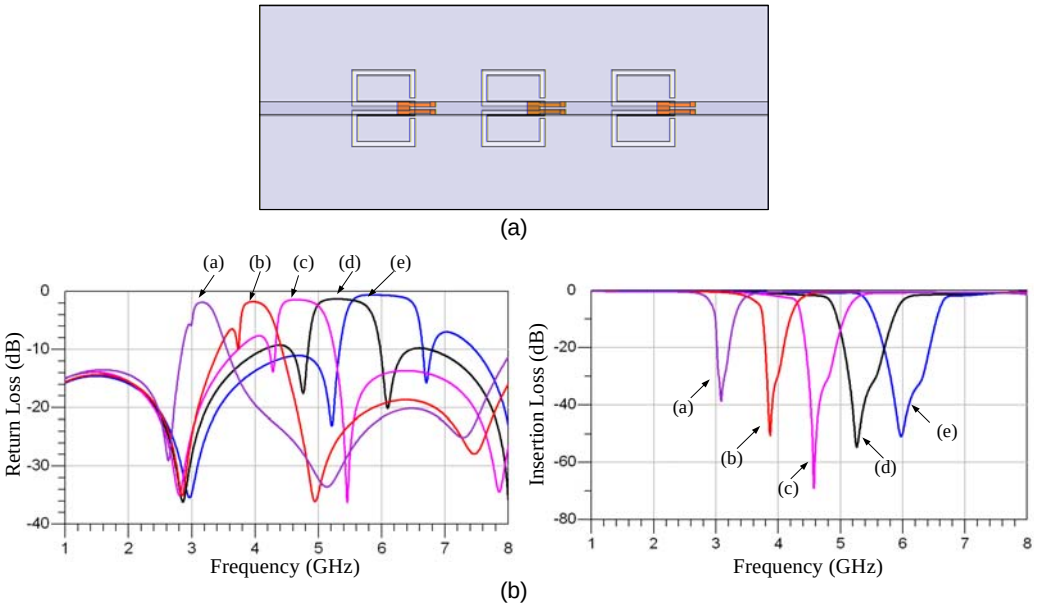

Figure 5-3: A three-pole tunable bandstop filter with the proposed tuning mechanism: (a) the design layout and (b) the simulated results.

5.2.2 Zigzag Slot Resonator

The configuration of the microstrip line with slots etched in the ground plane is selected in this work, since it can be modeled by simple resonant circuits and the parameter extraction is straightforward [119]. In addition, the configuration is more compact than that of the CPW line, where the slots are etched in the ground plane [118]. Fig. 5-4 shows three types of slot resonators that are examined in this research. All the slot resonators have the same slot width, but different slot lengths in order to maintain the same resonant frequency, as displayed in Fig. 5-4.

As illustrated in Fig. 5-5, the U-slot resonator has the highest quality factor of the three slot resonators, whereas the C-slot resonator has the lowest quality factor. The U-slot resonator is more lengthy in the Y direction than the other two resonators. The footprint is considerably large when the U-slot resonator is adopted to construct the bandstop filter, since all resonators are cascaded along the Y direction. The zigzag slot resonator has a better quality factor than the C-slot resonator, and maintains a comparable footprint as the C-slot resonator. Fig. 5-

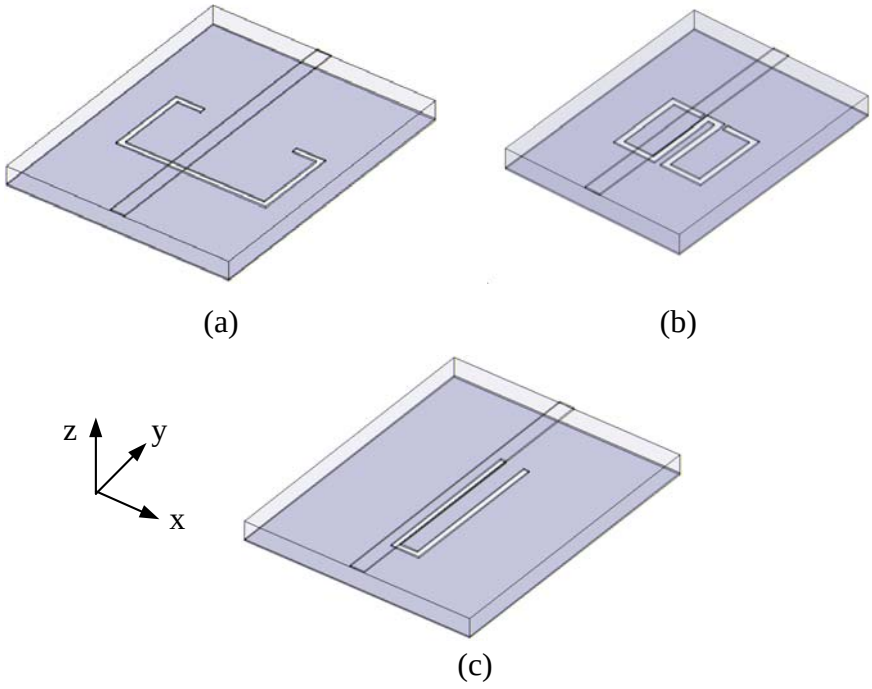

Figure 5-4: The schematics of slot resonators with various shapes: (a) the C slot, (b) the U slot, and (c) the zigzag slot.

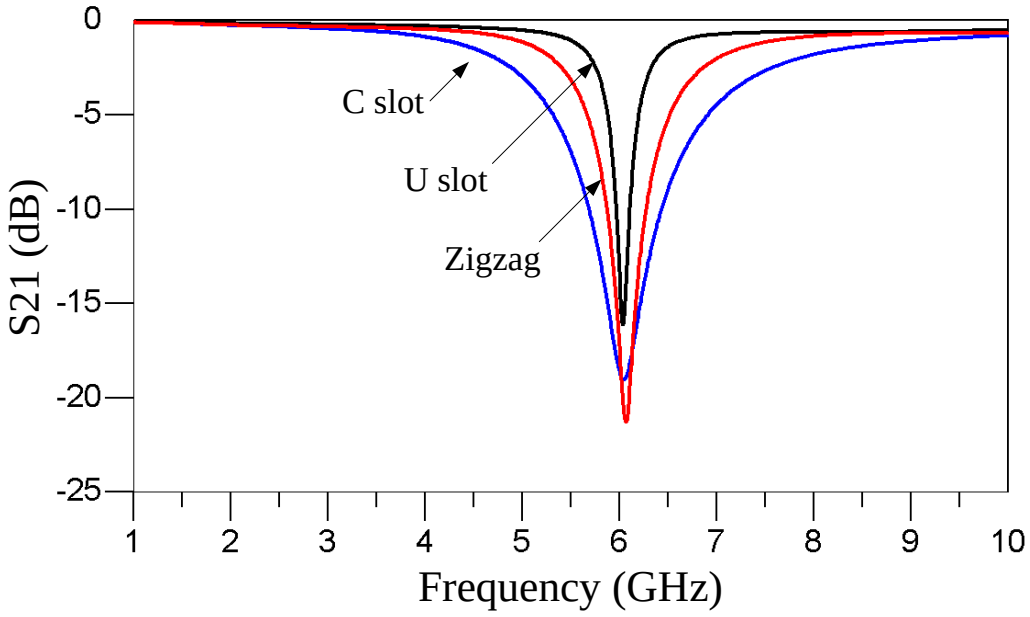

Figure 5-5: A comparison of the simulated results of the three slot resonators.

6 depicts the electrical field distribution of the three slot resonators. The electrical field of the C-slot is almost evenly distributed along the slot, whereas the zigzag slot and the U-slot resonators' electrical field is concentrated in the area under the microstrip line. As shown in Fig. 5-7, when the same tuning element is used, the U-slot resonator can achieve the widest tuning range; the C-slot resonator has the smallest tuning range.

After the quality factor, footprint and tuning range of the three slot resonators are balanced, the zigzag slot resonator is selected as the basic resonating unit to create the three-pole bandstop filter. The dimensions are listed in Table 5.1. An alumina substrate with a thickness of 25 mil and a dielectric constant of 9.9 is chosen for all simulations. The frequency response exhibits a typical passband-stopband property, and is shown in Fig. 5-8.

Table 5.1: Dimensions of the zigzag slot resonator (unit: mm)

Parameter	Dimension	Parameter	Dimension
w	0.52	b	1.1
l	2.5	c	1.4
a	0.6	g	0.2

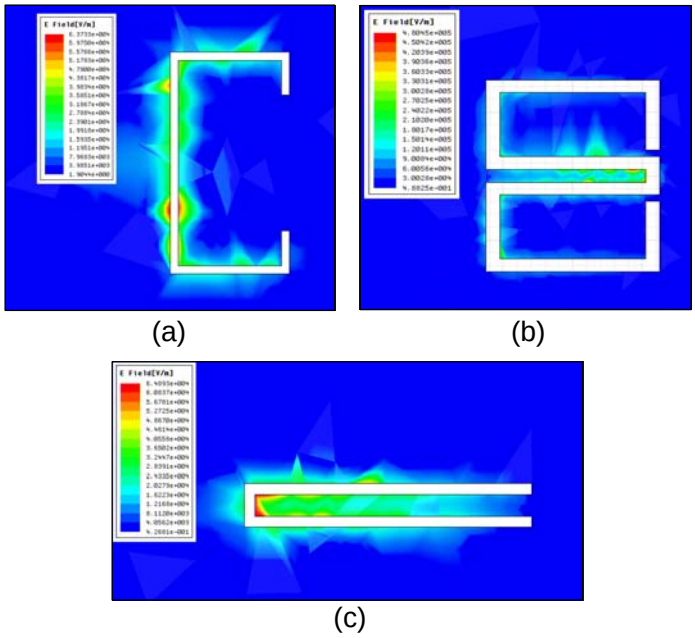

Figure 5-6: A comparison of the electrical field distribution of the three different slot resonators.

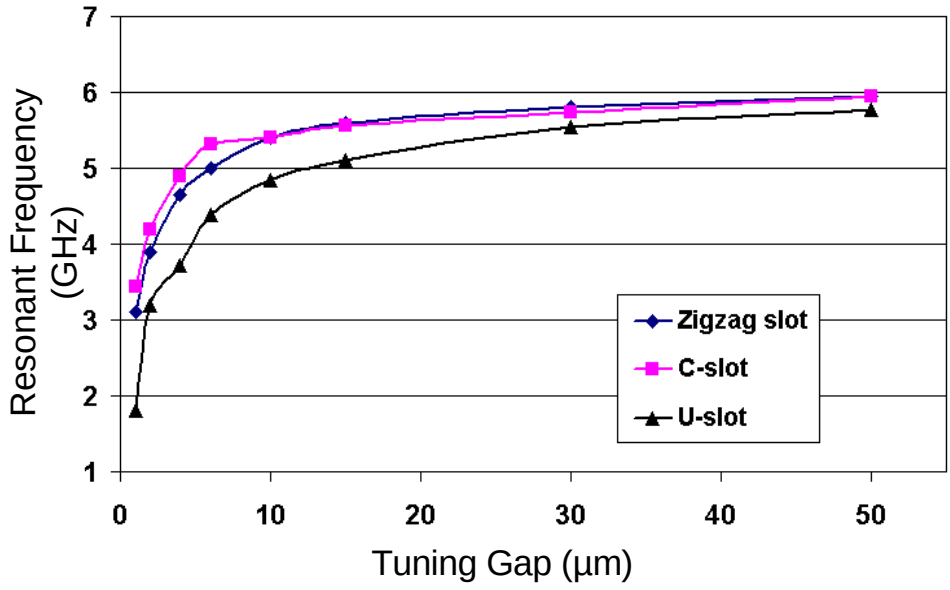

Figure 5-7: A comparison of the resonant frequency tuning of the three resonators with the same tuning element.

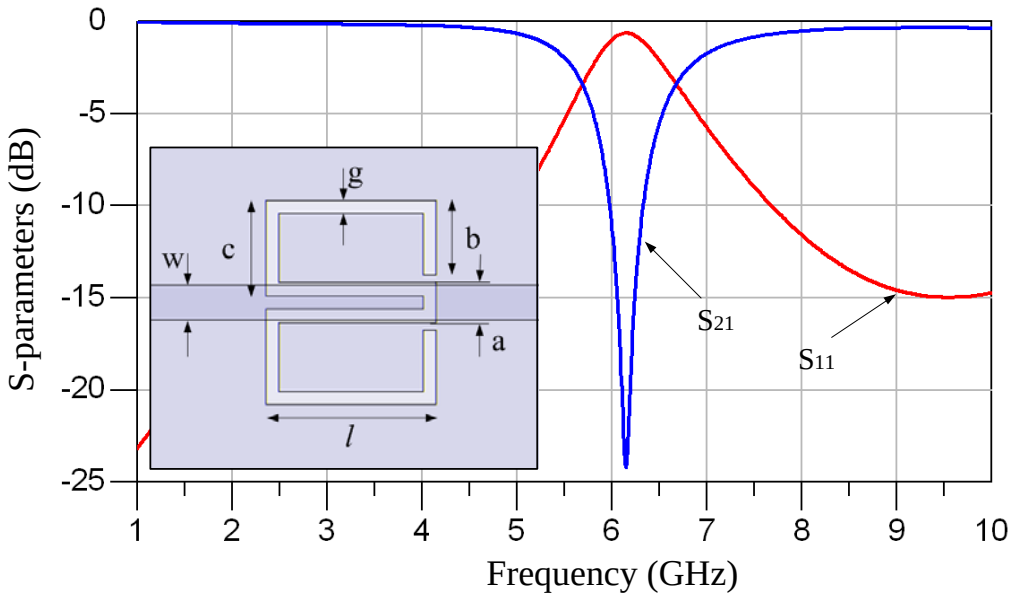

Figure 5-8: The frequency response of the zigzag slot resonator shown in 5-1.

5.2.3 Tuning Element Design

There are two types of actuators suitable for the proposed tuning structure: electrostatic and thermal. The electrostatic actuator provides a fast tuning speed and consumes almost zero power. However, the actuator has a limited deflection which indicates a narrower tuning range for a tunable bandstop filter. Often the electrostatic actuator requires a high biasing voltage for a mid range deflection. In addition, the electrostatic actuator is subject to the pull-in effect, which prevents the actuator from providing continuous tuning. On the contrary, the thermal actuator achieves a deflection in the order of hundreds of microns with a very low actuating voltage. Moreover, the power consumption can be significantly reduced by implementing latching mechanisms. The thermal actuator is a perfect candidate for the proposed tuning structure.

Fig. 5-9 gives the cross section of the novel tri-layer MEMS thermal actuator with two metal layers and one dielectric layer. The bottom metal layer is used to disturb the electric field above the zigzag slot resonator and to provide a RF tuning function. The DC current passes through only the top metal layer to attain a mechanical deflection. The dielectric layer is used to separate the top metal from the bottom metal. In this way, the DC biasing circuit is

isolated from the RF circuit, simplifying the RF circuit design. In addition, the stress mismatch between the metal and dielectric layers facilitates the initial deflection of the tri-layer MEMS thermal actuator after the final release.

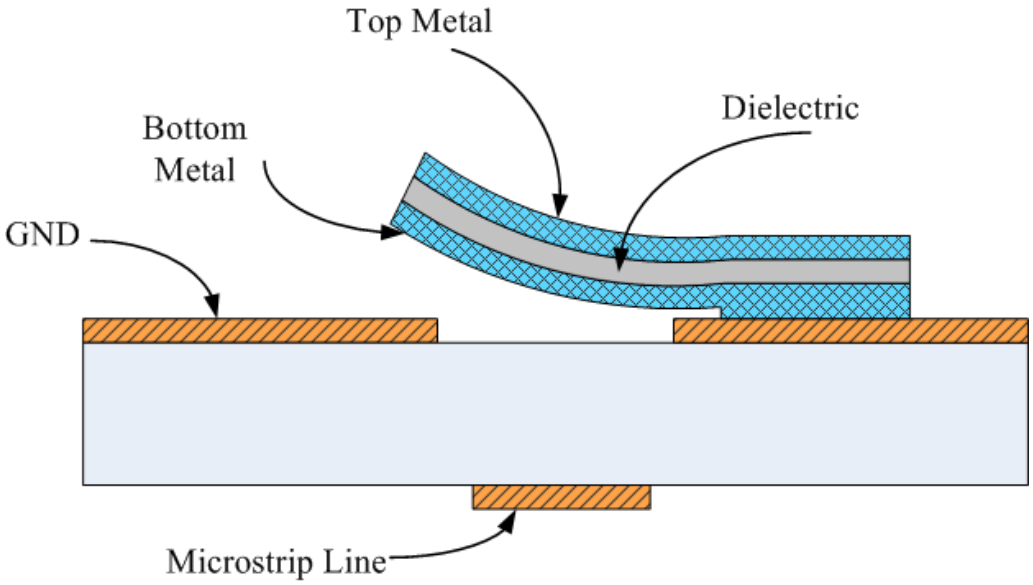

Figure 5-9: A cross section of the proposed tri-layer MEMS thermal actuator.

5.3 Fabrication Process for Tri-Layer MEMS Actuators

The proposed MEMS tunable bandstop filter is fabricated by using the process, illustrated in Fig. 5-10. Four masks are required to monolithically fabricate the bandstop filter and the MEMS tuning elements on the same substrate. The newly developed process starts with a bare alumina wafer. After the substrate is cleaned by RCA solution, a 1-μm gold layer is evaporated on both sides of the substrate. Then, mask 1 is used to pattern the gold on the front of the substrate to form microstrip lines. After the front is patterned, the substrate is coated with a positive photoresist as the protective layer. The remaining process steps only occur on the back of the substrate. Here, mask 2 is used to pattern the gold on the back of the substrate to realize zigzag slot resonators.

Before the MEMS tuning elements are fabricated, a sacrificial layer is needed to space

the MEMS elements from the substrate. LOR15, a non-photosensitive resist, is selected as the sacrificial layer. Prior to spin coat LOR15, the wafer is baked for 2 minutes at 160 ^{0}C for dehydration. After the coating, the wafer is baked again for 30 minutes at 190 ^{0}C in a convection oven. This sacrificial layer is then patterned by mask 3 to construct the anchors for the structure layers. AZ3312, a photosensitive resist, is chosen to pattern the sacrificial layer and is removed later in the developer, and Reactive Ion Etching (RIE) is employed to etch the sacrificial layer. This step is timed to ensure a 1-μm sacrificial layer remains. After LOR15 is patterned, a 1-μm of aluminum is sputtered on top of the sacrificial layer as the first metal structural layer. Then 1-μm of amorphous silicon is deposited by using Plasma Enhanced Chemical Vapor Deposition, (PECVD) for the dielectric layer. After the coating of the amorphous silicon film, another 2-μm aluminum is sputtered as the top metal structure layer. The top aluminum layer is patterned by mask 4 and wet etched. It serves as a good masking material for etching amorphous silicon in the RIE chamber. Then the bottom aluminum is wet etched. As a final step, the sacrificial layer is wet etched, releasing the devices. The PG remover is selected as the etching solution for the sacrificial layer. Fig. 5-11 portrays an SEM of the fabricated tri-layer MEMS tuning element.

The newly developed surface fabrication process is a good candidate not only for MEMS tunable bandstop filter, but also for other RF MEMS applications such as switches and phase shifters. As shown in Fig. 5-11, due to the stress mismatch between each structure layer, the proposed unique tri-layer MEMS tuning element easily achieves a deflection in the order of hundreds of microns. Also, the new process has a very low fabrication temperature (less than 200 ^{0}C), which make it very compatible with the commercial CMOS process. This feature can facilitate the system integration of passive RF components with active circuits.

5.4 Experimental Results

The proposed tunable bandstop filter is fabricated on a 1-inch square alumina substrate. The spacing between each slot resonator is 5.103 mm, which is a quarter wavelength at the center frequency. The 50-Ω microstrip line extends to the edge of the substrate in order to launch the filter through SMA connectors. However, from the RF design point of view, the filter

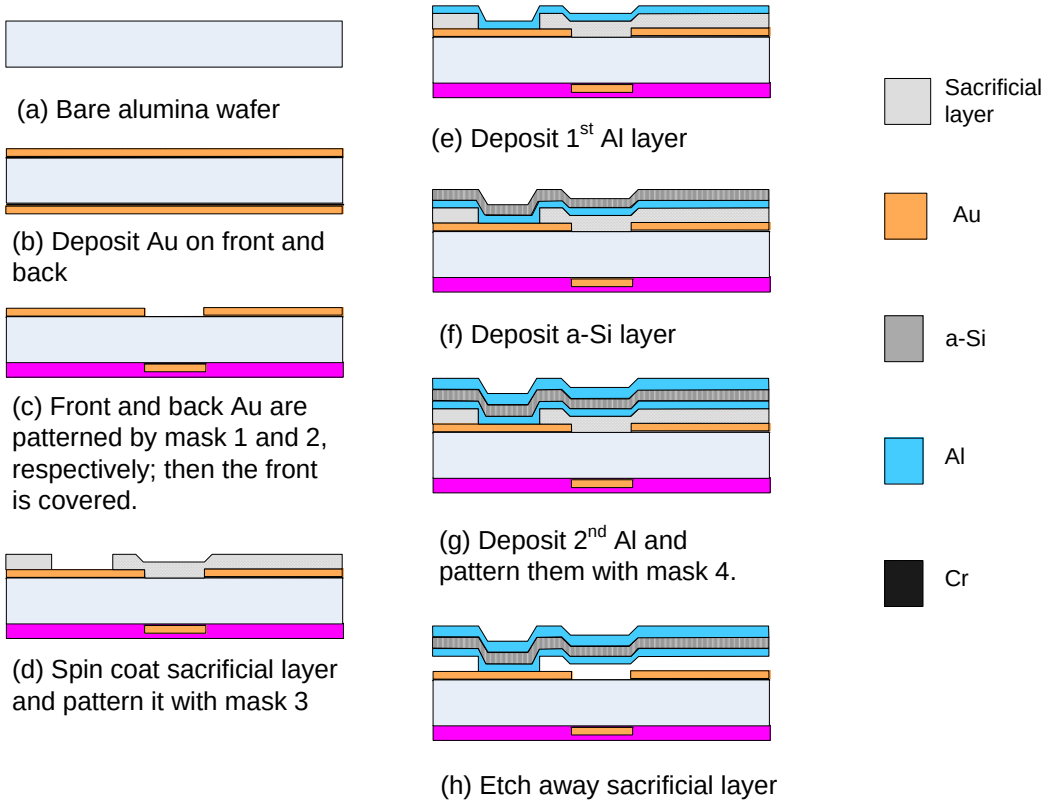

Figure 5-10: The fabrication steps of the proposed MEMS tunable bandstop filter.

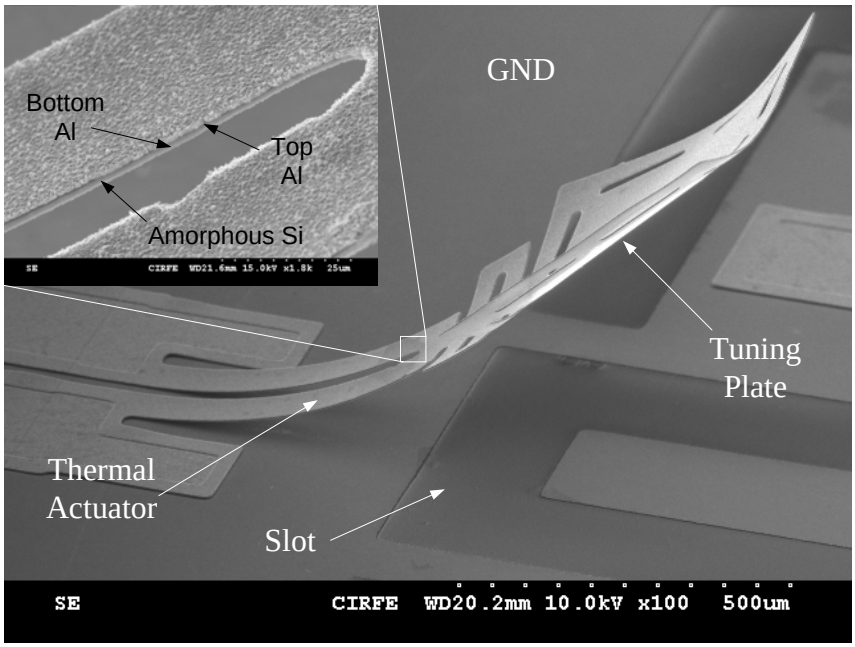

Figure 5-11: An SEM image of the fabricated tri-layer tuning element.

does not need such a long microstrip line as the input and output coupling. Fig. 5-12 (a) denotes a front view of the fabricated tunable bandstop filter. Fig. 5-12 (b) illustrates the tri-layer tuning elements and the slot resonators on the back of the alumina substrate. The white traces, surrounding the slot resonators and MEMS tuning elements, are the aluminum DC biasing circuits. The inset in Fig. 5-12 (b) exhibits the detail of a tri-layer tuning element.

The simulation results are in good agreement with the test results of the three-pole bandstop filter without actuating the tuning elements, as conveyed in Fig. 5-13. It is shown that the fabricated filter, with three cascaded zigzag slot resonators, rejects the signals at frequencies from 5.7 GHz to 6.5 GHz with more than 20-dB suppression. The slight deviation in the bandwidth of the measured result from the simulation result is attributed to the fabrication tolerance.

For the purpose of verifying the novel tuning concept, a tunable bandstop resonator with the proposed MEMS tuning element is tested first. Fig. 5-14 depicts the test setup for measuring the resonant frequency of the zigzag slot resonator with the proposed tuning element. To eliminate the impact of the DC probes on the resonant frequency of the resonator, two chip

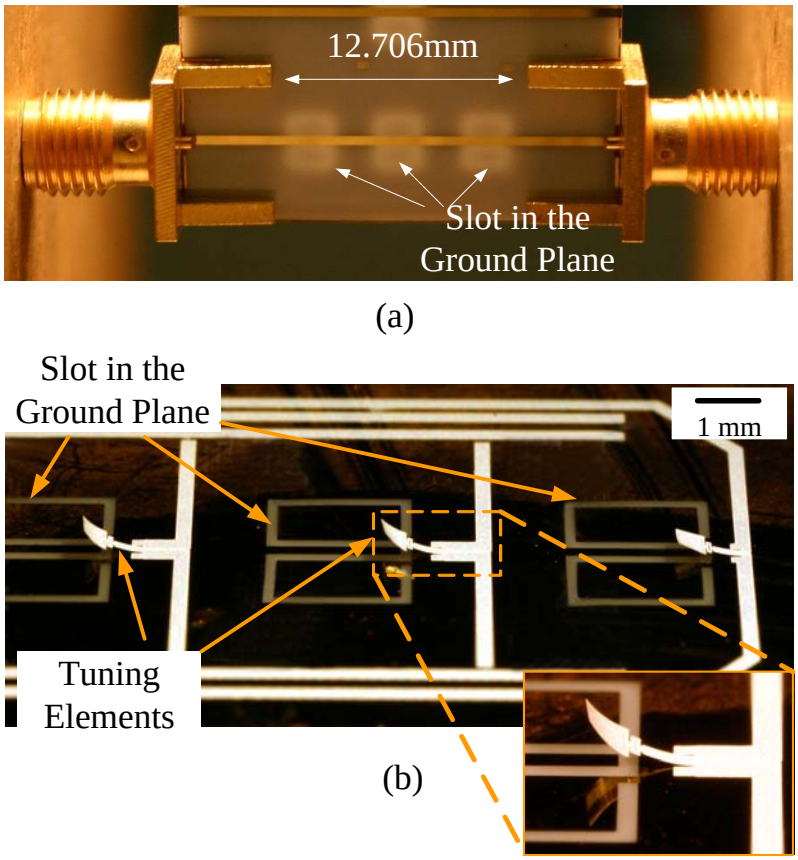

Figure 5-12: (a) A top view of the fabricated tunable bandstop filter and (b) a close view of the MEMS tuning elements.

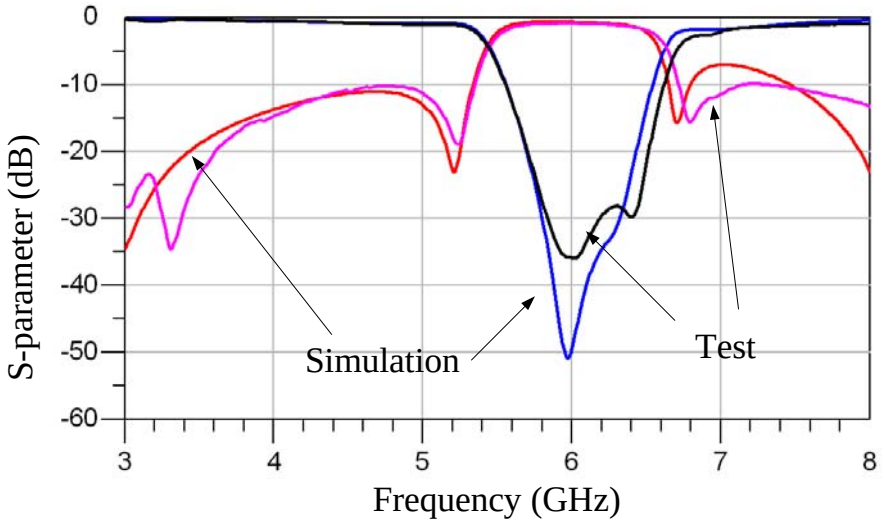

Figure 5-13: A comparison of the simulation and test results of the 3-pole MEMS tunable bandstop filter (without tuning).

capacitors are employed. After they are assembled on the ground by silver epoxy, the anchor pads of the thermal actuator are connected to the top surface of the chip capacitors by wire bonding. When DC voltage is applied to actuate the tuning element, DC probes are placed on top of the chip capacitors. The measured results in Fig. 5-15 demonstrate that the proposed tuning concept can continuously tune the resonant frequency of the slot resonator over a range of 1.5 GHz. The measured results for the fabricated three-pole tunable bandstop filter are illustrated in Fig. 5-16. The center frequency of the bandstop filter is tuned over a range from 6.09 GHz to 5.575 GHz. When the filter is tuned to the lower frequency, the insertion loss of the upper band of the tunable bandstop filter is increased due to the lowering of the tuning elements.

5.5 Summary

In this chapter, a novel approach to construct a tunable bandstop filter has been presented and discussed in detail. To the best of the authors' knowledge, this is the first time that tri-layer MEMS actuators have been applied to the design of a continuously tuned MEMS bandstop filters. A unique surface microfabrication process has been developed to facilitate the

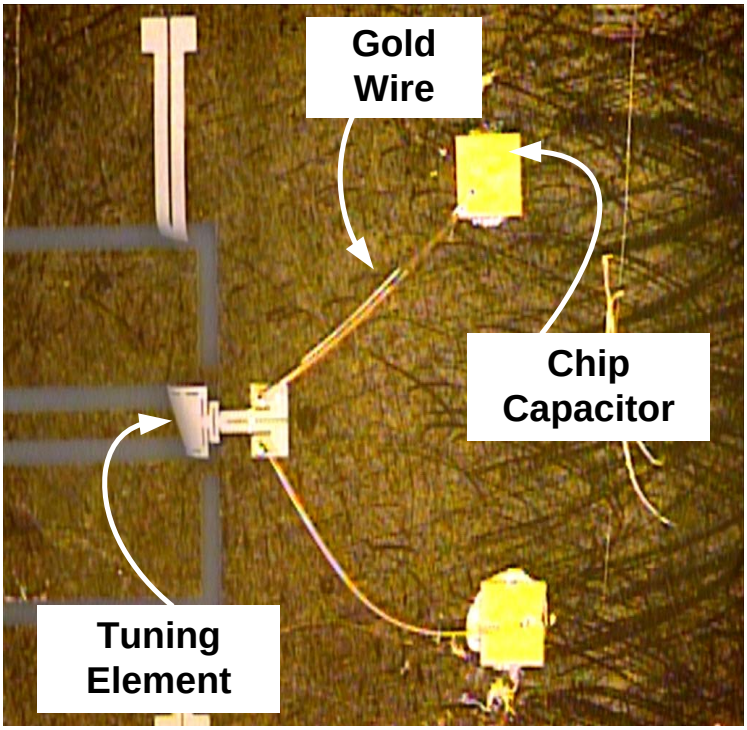

Figure 5-14: The test setup for measuring the resonant frequency of the zigzag slot resonator with tuning.

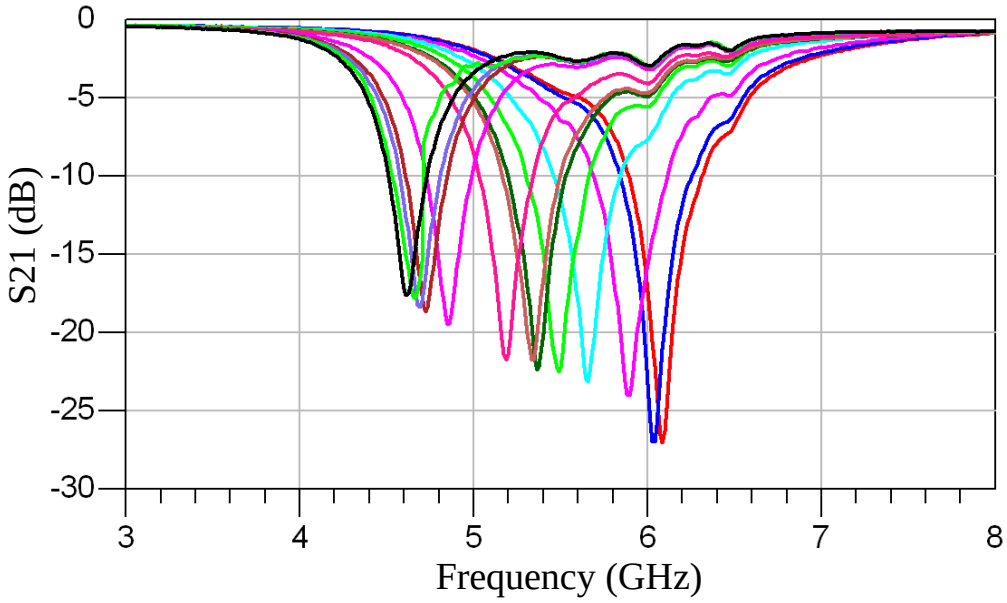

Figure 5-15: The measured results of the proposed tunable bandstop resonator when it is tuned at different frequencies.

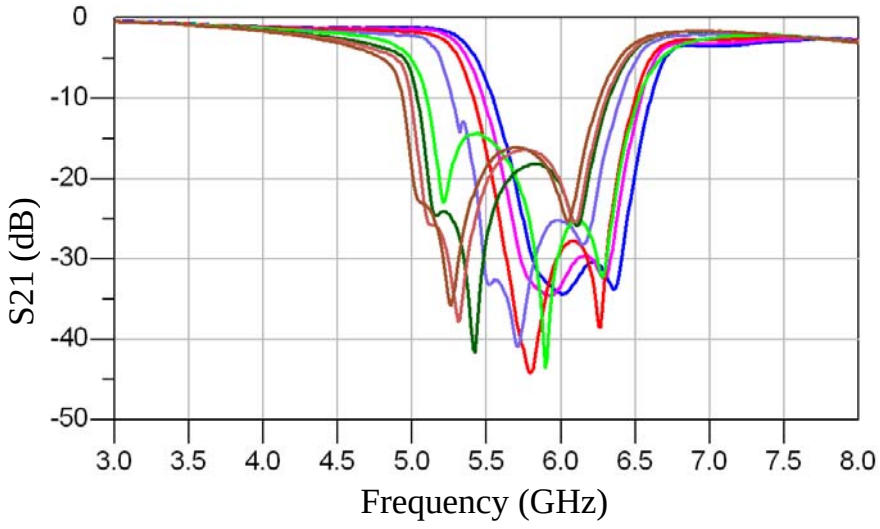

Figure 5-16: The measured results of the proposed three-pole tunable bandstop filter when it is tuned at different frequencies.

monolithic integration of MEMS tuning elements with the bandstop filter. This leads to the realization of miniaturized tunable bandstop filters with a compact size, a wide tuning range, low cost and reasonable tuning speed. A three-pole tunable bandstop filter has been designed, fabricated and tested. The measured results confirm the feasibility of the proposed concept.

Chapter 6

Micromachined Latching Mechanisms for MEMS Tunable Filters

6.1 Introduction

Reliable latching mechanisms are an integral part of microsystems for applications such as wireless communications [120, 20, 88], optical networks [121, 122, 123], and sensors [124, 125], where power consumption and heat dissipation must be mitigated. The need for employing latching mechanisms in this research is to secure the position of the tuning elements embedded in the MEMS tunable filters. No power input is required after the filters are fine tuned. Therefore, requirements of a latching mechanism based on this purpose are as follows:

- The fabrication process for the latching mechanism should be compatible with that of MEMS filters;
- The latching mechanism should require as few structure layers as possible to keep the entire process simple.
- It is desirable for the latching mechanism to have multi-stable positions, so that a wide tuning range can be achieved.

The latching mechanisms in the literature either have a limited number of stable states [23, 20, 78], or can secure only in-plane motions [85, 21, 22]. None of the latching mechanisms in the literature are suitable for the tunable filters that have been developed in this research. In this section, various out-of-plane latching mechanisms are examined. All the latching mechanisms are capable of securing out-of-plane motions, which are perfect candidates for tunable filters developed in this research. In addition, the fabrication processes are compatible with that for fabricating MEMS tuning elements.

6.2 Design Concept

The design concept of the out-of-plane latching mechanisms in this chapter is inspired by the self-assembly of the 3D microstructures, illustrated in [26, 27, 126]. For example, in [26], a magnetic actuation is employed to attain the out-of-plane rotations of hinged microstructures. The rotation angle is controlled by the type of hinged structures, the volume of Permalloy on the microstructures and the strength of the external magnetic field. The combination of the two hinged structures is used to assemble a 3D microstructure which remains stable after the external magnetic field is removed (Fig. 6-1). The sequence of lifting the two flaps is determined by the volume of the permalloy on each flap, as the external magnetic field is gradually increased.

To assemble the 3D microstructures, magnetic actuation offers the following advantages: (1) the assembly can be realized at the wafer level, and (2) the required space for actuation is minimum. However, this method needs an external magnetic field that is quite bulky and an accurate assembly with this technique is challenging. Besides utilizing magnetic actuation to assemble the 3D microstructures, the surface tension technique is also capable of building 3D microstructures in [27, 126]. Fig. 6-2 (a) portrays a general geometry of the surface tension powered, self-assembled 3D microstructure. It includes fixed and movable mechanical parts that are connected by meltable photoresist. The out-of-plane rotation of the movable part is produced by melting the thick photoresist. To achieve a precisely assembled position, a mechanical limiter, the inset in Fig. 6-2 (b), is incorporated in the design.

surface tension techniques incorporated with mechanical limiters can achieve accurately assembled 3D microstructures. Also, the required fabrication process is compatible with many

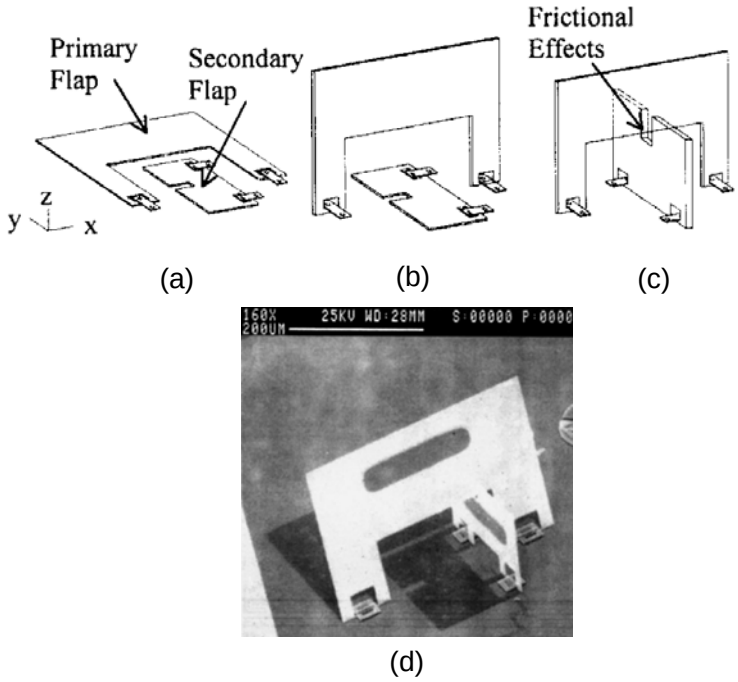

Figure 6-1: The assembly process for the two-flap 3D structure: (a) the original position when no external magneitc field is applied, (b) the primary flap rises to 90^0 when H_{ext}=H_1, (c) a full 3D assembly is achieved at H_{ext}=H_2 (H_2>H_1), and (d) the SEM of the assembled structure [26].

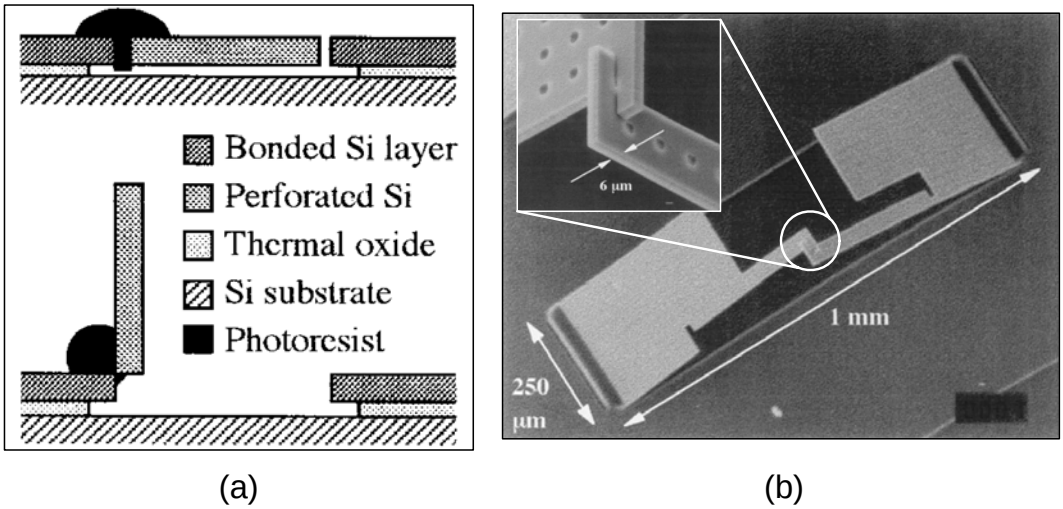

Figure 6-2: (a) A schematic of the surface tension powered self-assembly and (b) An SEM of the self-assembled structure with mechanical limiters [27].

micromachining processes. The assembly temperature is between 130 ^{0}C and 150 ^{0}C, which is considerably low. However, this assembly process is irreversible; that is, once the microstructure is assembled, it is almost impossible to disassemble the microstructure.

For tunable filter applications, it requires latching mechanisms embedded in tuning elements can be easily switched between stable states. Moreover, the fabrication process for latching mechanisms has to be compatible with that for MEMS tuning elements. None of the assembly techniques in the literature can meet the requirements for tunable filter applications, since their fabrication processes are not compatible with those for MEMS tuning elements or they cannot be easily disassembled. MEMS thermal actuators with large out-of-plane deflections and rotations have been successfully demonstrated [108, 127]. By replacing the magnetic actuators or meltable photoresist with such MEMS thermal actuators, the concept of self-assembly 3D microstructures can be adopted to design out-of-plane latching mechanisms with multi-stable states. The out-of-plane deflections or rotations, generated by MEMS thermal actuators, is reversible with the aid of DC control signals.

Fig. 6-3 (a) depicts a MEMS thermal actuator, connected to a mechanical limiter with an orientation orthogonal to the substrate. The MEMS thermal actuator is constructed by the Thermal Plastic Deformation Assembly (TPDA) method [108]. It consists of a number of bimorphs of gold and polysilicon that are cascaded through passive polysilicon beams. After the TPDA treatment, the gold layer of each bimorph is plastically deformed by large compressive stresses due to the different thermal expansion coefficients between the two materials. Therefore, each bimorph is bent slightly upward, and maintains the new shape at room temperature. The large out-of-plane rotation is accomplished by accumulating each bimorph's deflection. When a current is applied to the thermal actuator, each bimorph returns to its original position because of joule heating. A microstructure, similar to the one in Fig. 6-2 (b), is obtained by replacing the meltable photoresist with two MEMS thermal actuators, as seen in Fig. 6-3 (b). Unlike the surface tension powered assembly process, the thermal actuator powered assembly is reversible. The two mechanical limiters are readily unlatched from each other by applying DC currents to the MEMS thermal actuators.

Fig. 6-4 demonstrates a latching mechanism with multi-stable positions. It comprises two latching flaps (A and B) that are connected with MEMS thermal actuators to obtain an out-

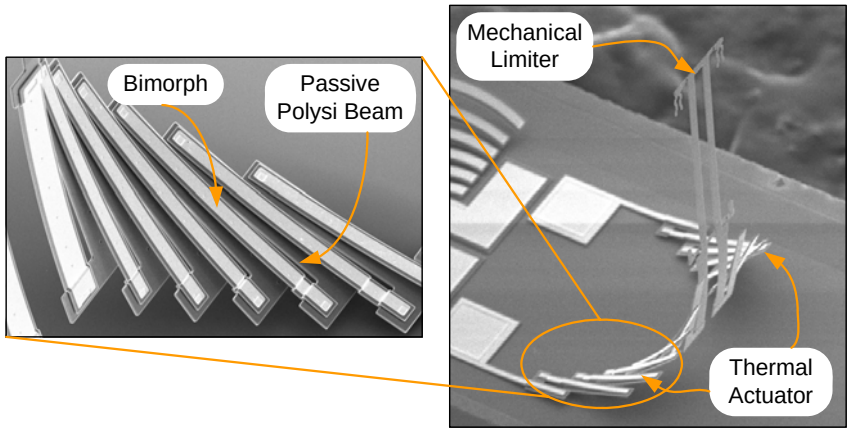

(a)

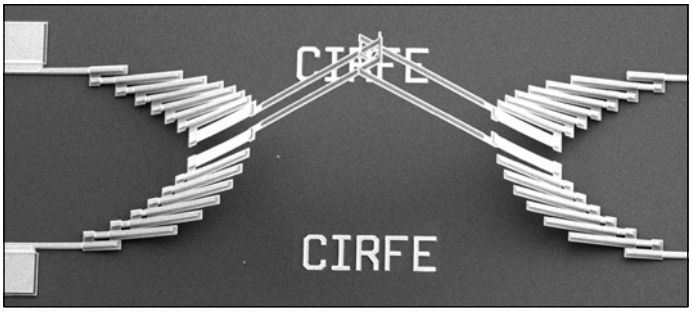

(b)

Figure 6-3: A thermal actuator incorporated with (a) a mechanical limiter after TPDA treatment and (b) a latch mechanism that comprises two such structures.

of-plane rotation. Tethers are used to hold the plates during the wet releasing process and to protect them from fluidic force. After the TPDA treatment, these tethers are removed by DC probes. To use flap B to hold flap A at a desirable position, flap B is first rotated towards the substrate by applying a DC current. After the path for flap A is cleared, a DC current is applied to flap A. Once flap A is moved to the desired position, the DC current is removed from flap B. Then, flap B is moved upwards, until it engages with flap A. Up to this point, all the DC currents can be removed and the latching mechanism retains a stable position. The slots are placed on flap B to increase the friction with flap A.

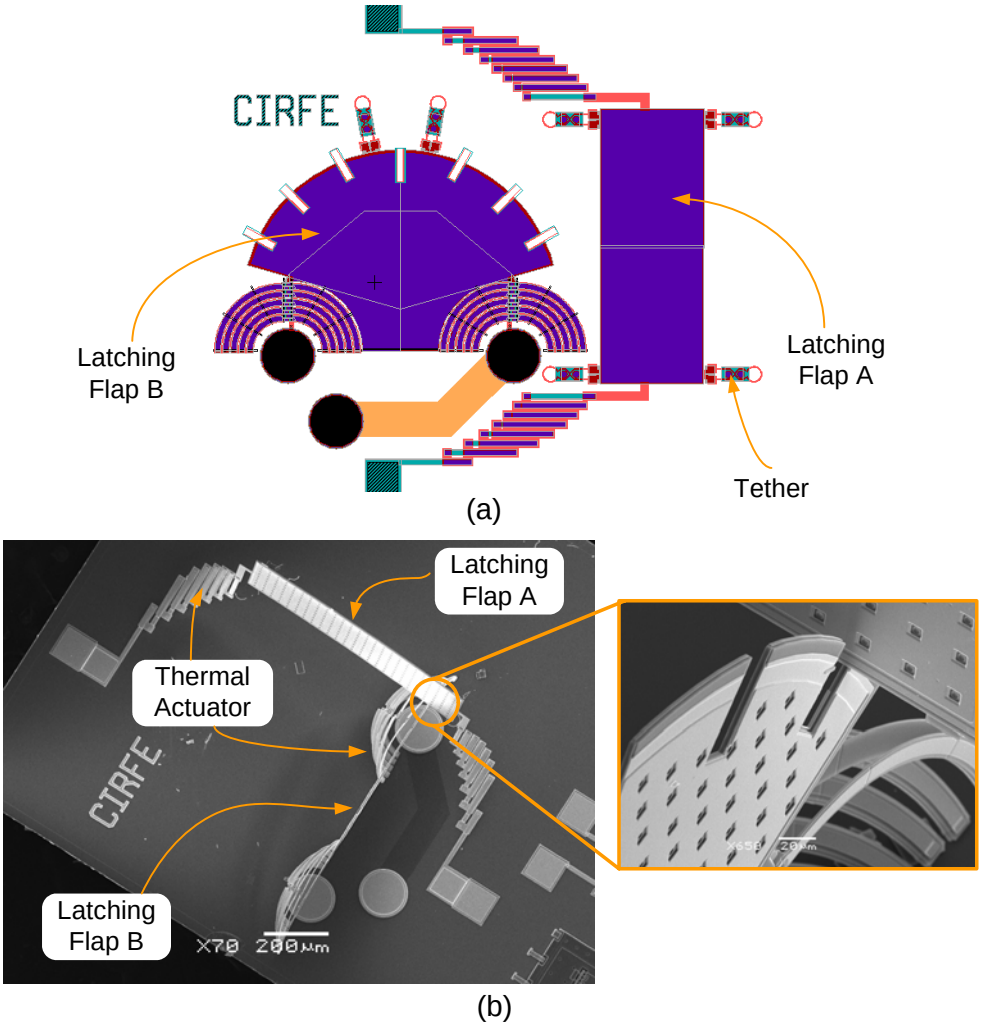

Figure 6-4: Thermally assembled latching mechanism: (a) layout and (b) SEM.

6.3 Latching Mechanism Design for Tunable Bandpass Filter

The purpose of integrating multi-stable latching mechanisms with MEMS tuning elements is to secure the tuned response of the tunable bandpass filter that are described in Chapter 4. The newly devised latching mechanism is designed according to the PolyMUMPs microfabrication process, since the process is also employed to fabricate the MEMS tuning elements for the tunable bandpass filters. PolyMUMPs is a surface micromachining process that consists of three polysilicon layers and one metal layer [28]. The top two polysilicon layers, poly1 and poly2, are released from the substrate to form free-standing mechanical structures. The poly0 layer and the metal layer are used for the electrical routing. Fig. 6-5 illustrates all the material layers available in the PolyMUMPs process. Openings (Vias) can be made on the second oxide layer to make connections between poly1 and poly2. Poly1 and poly2 can be anchored on the substrate through openings (anchors) on the first oxide.

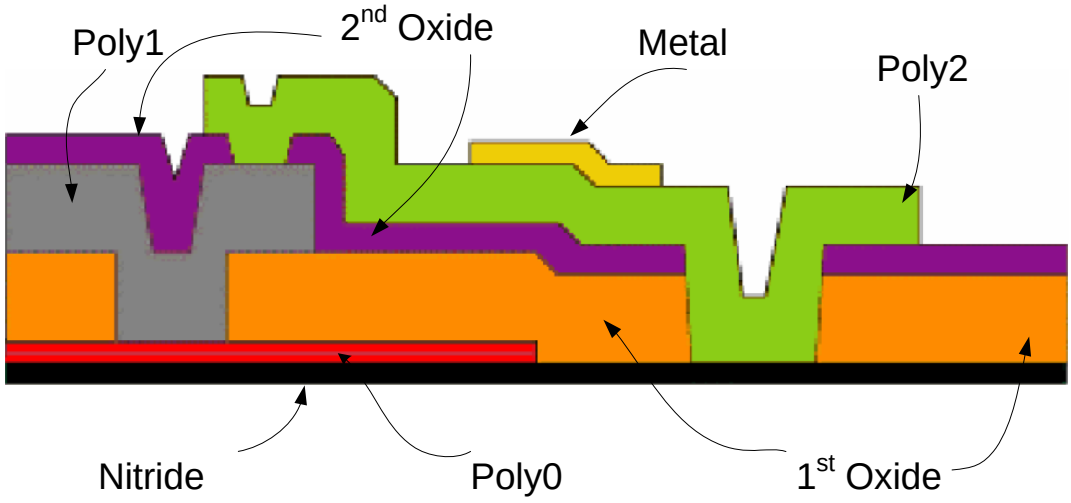

Figure 6-5: The cross sectional view of all the layers available in the PolyMUMPs process [28].

In this thesis, a novel MEMS latching mechanism with an out-of-plane motion and multi-stable positions is presented. A 2D schematic view of the proposed latching mechanism is shown in Fig. 6-6. The proposed latching mechanism contains two overlapped rectangle frames, A and B, that are attached to MEMS thermal actuators. Arched beams that are made of poly1 are placed along the inner side of frame A. frame B is attached to a U-shape beam that consists

of poly2. The width of the U-shape beam, w, is slightly wider than the gap between the arched beams, g. This ensures the U-shape beam cannot move freely, unless a force is applied. When a DC voltage is applied to the MEMS thermal actuators, the U-shape beam snaps through the narrow gap and moves between the wider openings. The resolution of the stable latching positions is determined by d, the distance between the two adjacent arched beams. The total travel range of this latching mechanism is related to L, the length of the rectangle frame. Fig. 6-7 depicts two stable positions of the proposed latching mechanism.

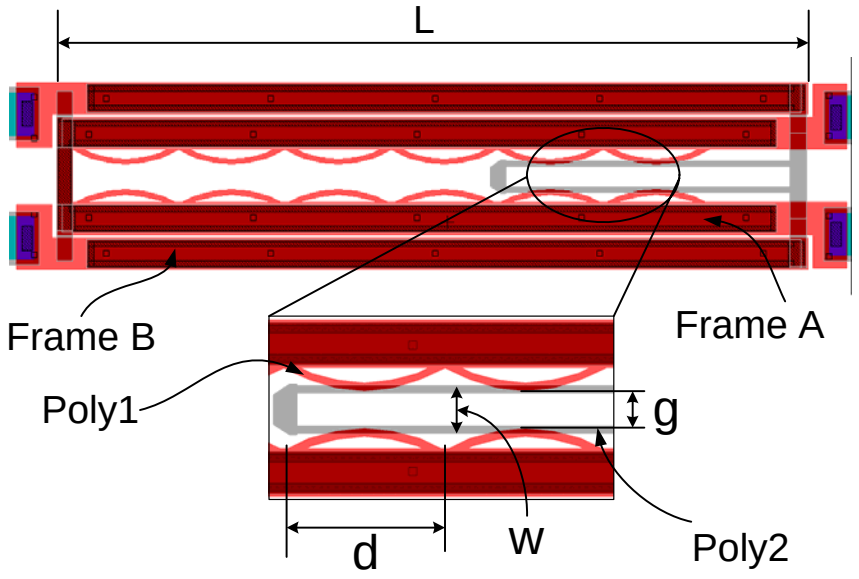

Figure 6-6: A schematic layout of the proposed latching mechanism.

Fig. 6-8 illustrates another proposed latching mechanism. Instead of attaching the arched beams to the frame as shown in Fig. 6-6, the newly proposed design contains two sets of cascaded arched beams that are attached to the short ends of frame A. Frame B includes a pair of clamped straight beams. The arched beams and the clamped straight beams are constructed out of poly1 and poly2, respectively. The distance between the two straight beams, a, is slightly wider than the gap between the two sets of arched beams, b, to secure the engagement of the two overlapping rectangle frames after they are moved to the desired position by MEMS thermal actuators. The resolution of the stable latching positions is determined by c, the distance between the two adjacent arched beams. The total travel range of this latching mechanism

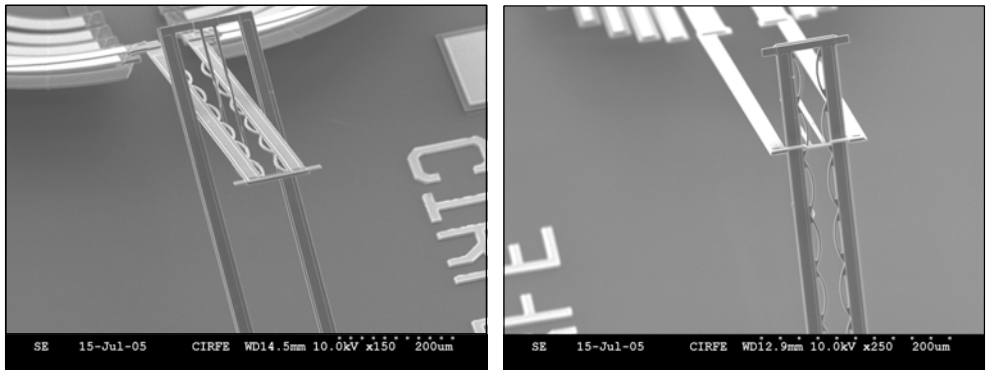

Figure 6-7: An SEM of the proposed latching mechanism with multi-stable positions.

is related to L, the length of the rectangle frame. Fig. 6-9 depicts an SEM of the proposed latching mechanism at one of the stable positions. The novel design results in a number of stable latching positions.

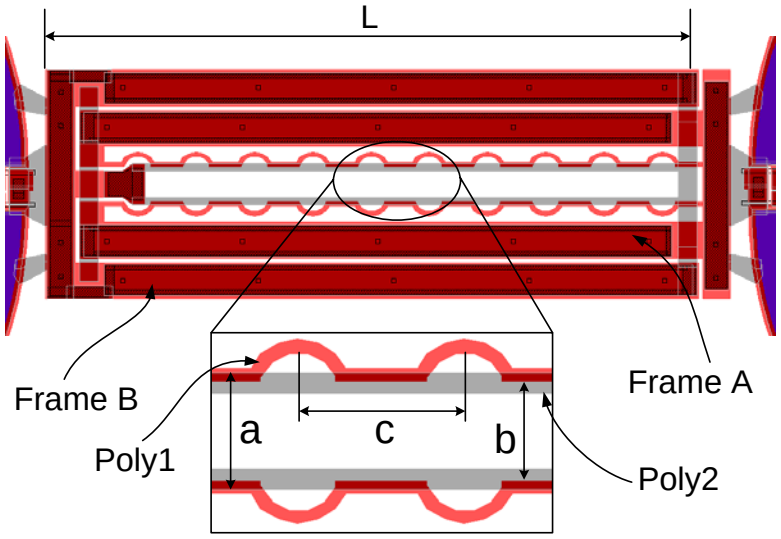

Figure 6-8: A schematic layout of the proposed latching mechanism.

To move the latching mechanism from one stable position to another, a DC current is applied to the thermal actuator that is attached to frame B. The force produced by the thermal actuator helps the flexible beams to snap through the gap between the two sets of arched beams. Once

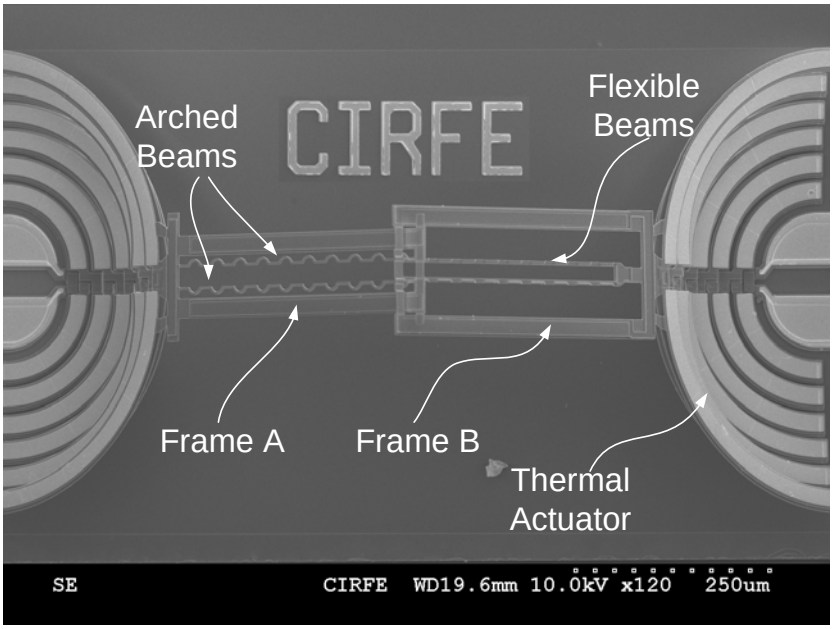

Figure 6-9: An SEM of the proposed multi-stable latching mechanism.

the DC current is removed, the latching mechanism remains at the new position. Since the space between the two flexible beams is wider than that of the arched beams, frame B cannot move along the gap between the two sets of arched beams. Fig. 6-10 shows the two latched positions of the proposed latching mechanism.

Fig. 6-11 portrays a MEMS tuning element, embedded with two proposed latching mechanisms. Instead of being attached to a MEMS thermal actuator, frame B is connected to the side of the tuning plate. When a DC current is applied to the MEMS tuning element, the tuning plate travels along the direction, orthogornal to the substrate, due to the large force generated by the MEMS thermal actuators. Once the current is removed, the two latching mechanisms hold the tuning plate in the new position.

To move the tuning plate along a direction that is perpendicular to the substrate, the MEMS tuning element must overcome friction induced by the proposed latching mechanism from each side. This is not desirable, since the mechanical parts wear out quickly due to the friction. Fig. 6-12 depicts an improved design. The two sets of arched beams and flexible beams are removed from frame A and B, respectively. A number of stoppers, made of poly2 and metal, are placed

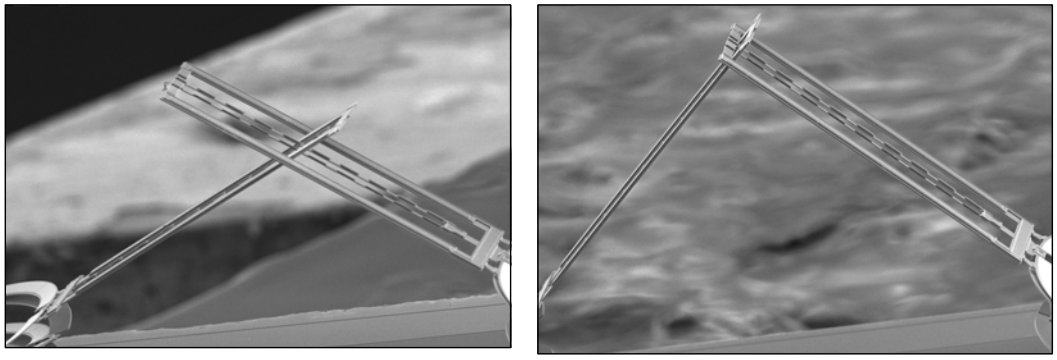

Figure 6-10: Two stable latching positions of the proposed latching mechanism.

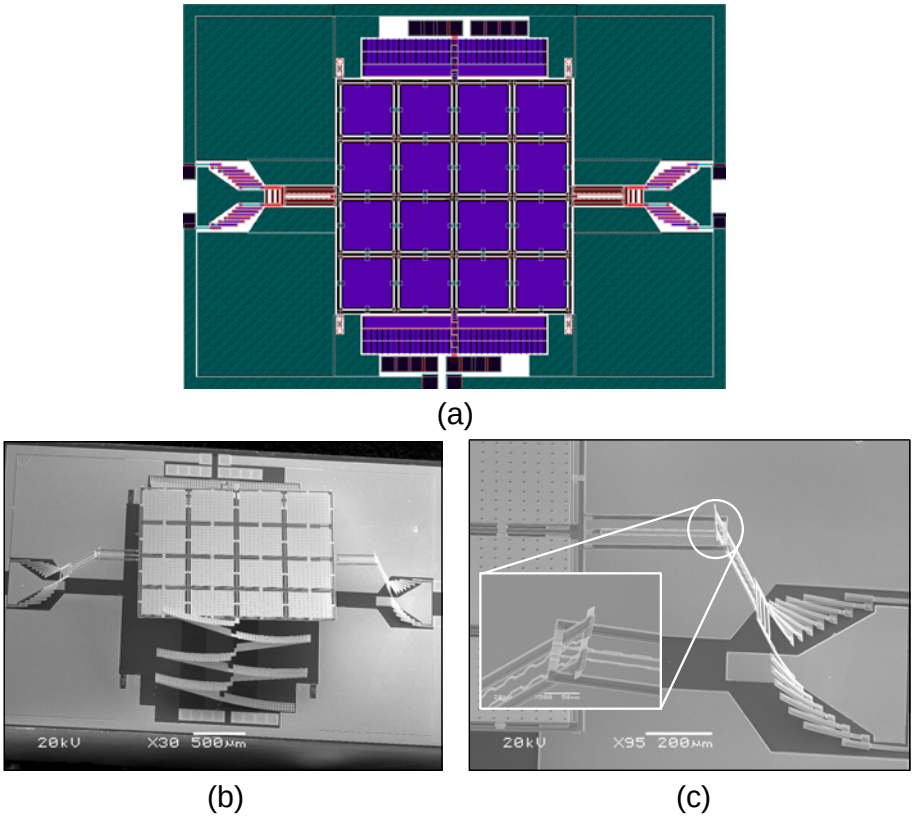

Figure 6-11: (a) A device layout of the MEMS tuning element embedded with latching mechanisms, (b) An SEM of the proposed design, and (c) a close view of the proposed latching mechanism.

on frame B as the primary latching mechanism. When the tuning plate is moved to its desired position, a DC current is applied to the thermal actuator that is connected to frame A. Once the frame A is engaged with the frame B, the DC current is removed . The stoppers block frame A from slipping back to its original position; therefore, the tuning plate remains at the tuned position. Fig. 6-13 shows micrographs of the improved design tuned at various positions.

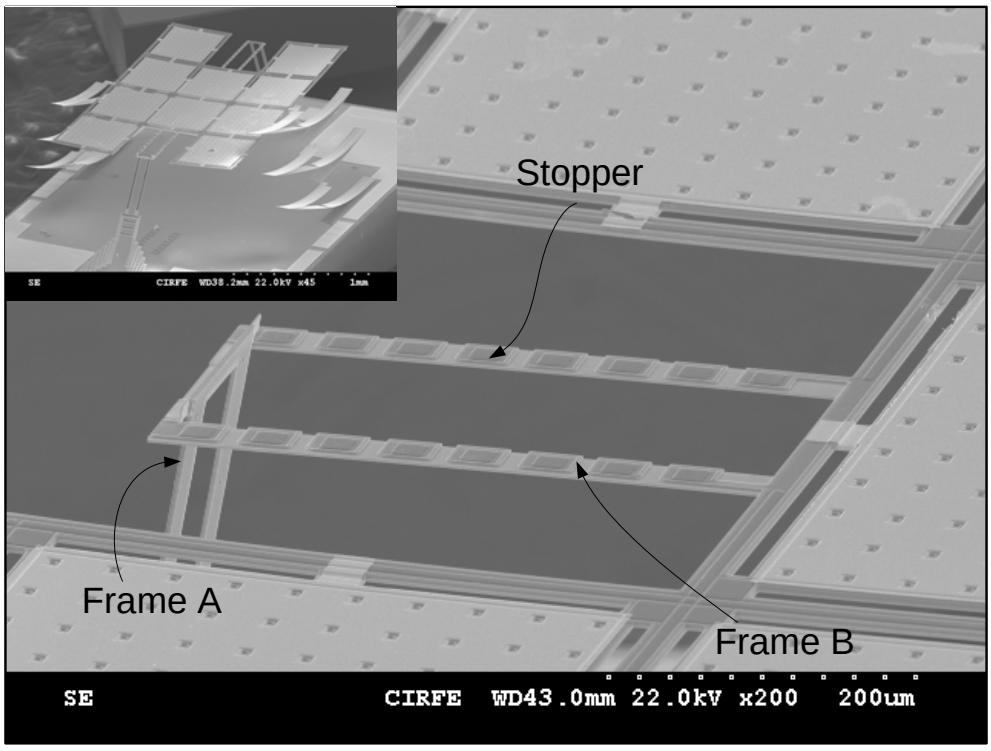

Figure 6-12: An SEM of the improved latching mechanism.

6.4 Latching Mechanism Design for Tunable Bandstop Filter

The objective of designing a latching mechanism for the tunable bandstop filter, described in Chapter 5, is to short circuit over the slot in the ground plane. The resonant frequency of a slot resonator depends on the length of the slot. Making short circuit over the slot can effectively change the length of the slot resonator, and therefore, change the resonant frequency. A tunable lowpass filter, based on this concept, is demonstrated by using off-chip switches [116].

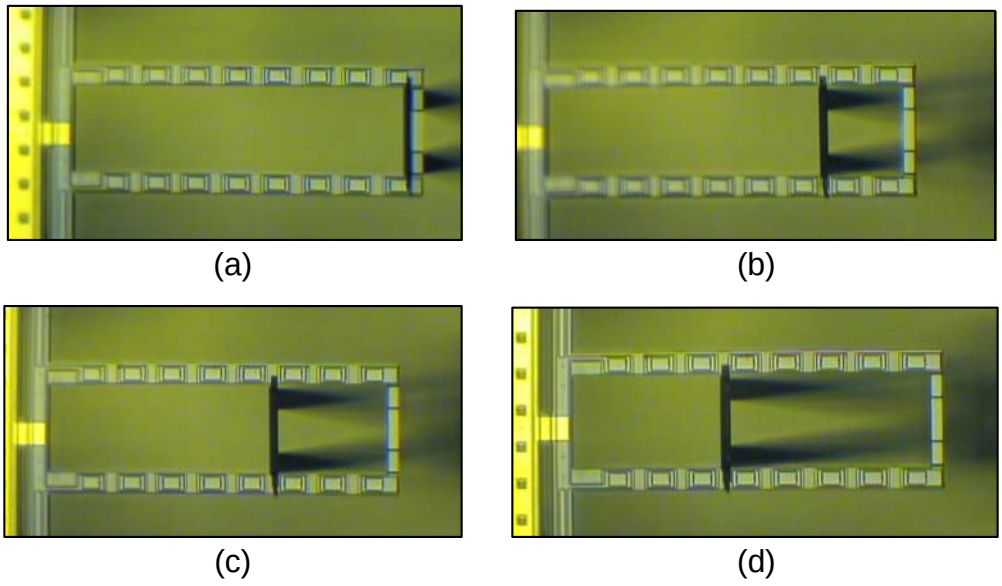

Figure 6-13: Micrographs of the improved latching mecahnism at various stable states.

Instead of post-assembling the off-chip switches, a surface micromachining process is developed to accommodate monolithically integrated latching mechanisms for the bandstop filter. The detail of the surface micromachining process is found in Chapter 5.

Fig. 6-14 (a) illustrates the layout of the proposed design. It consists of two thermal actuators anchored on the substrate. The actuator is made of two metal layers and one dielectric layer that is sandwiched between the two metal layers. Each thermal actuator has a built-in mechanical limiter that is across the centre line. During the releasing step, the two thermal actuators rotate simultaneously: one in a clockwise direction and the other one in an anticlockwise direction. The out-of-plane rotation of each thermal actuator is caused by the intrinsic stress of each layer and the stress mismatch between the metal and dielectric layers. The mechanical limiters on the thermal actuators engage during the rotation, since both of them are slightly across the centre line. Fig. 6-14 (b) shows an SEM of the fabricated device with more than one mechanical limiter on the thermal actuators to achieve the multi-stable positions.

As shown in Fig. 6-14 (b), the proposed design forms a short circuit across the slot, that is, the two thermal actuators stay at the latching state after release. To unlatch the two thermal actuators, two DC currents are applied to the two thermal actuators at the same time. Until

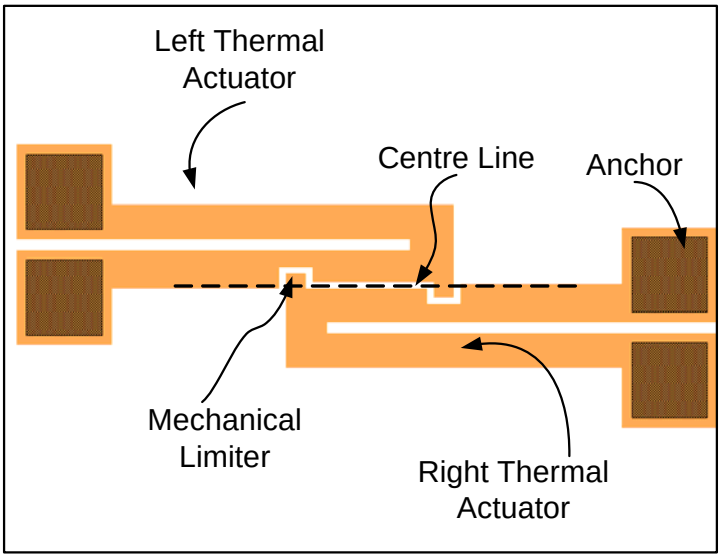

(a)

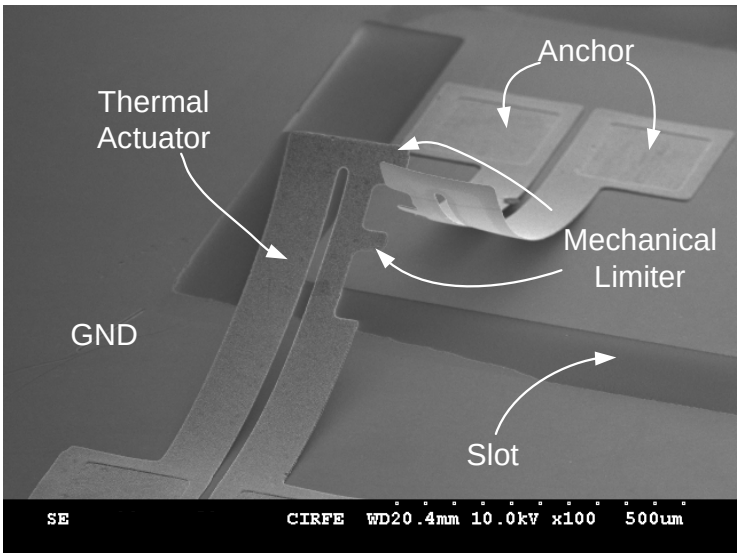

(b)

Figure 6-14: (a) the layout of the proposed latching mechanism and (b) an SEM of the fabricated latching mechanism over a slot resonator.

they are fully disengaged from each other (Fig. 6-15 (b)), the DC current is removed from one of the thermal actuators. As observed in Fig. 6-15 (c), the DC current is removed from the left actuator, whereas the other DC current is still applied to the right thermal actuator to hold it in the down position (Fig. 6-15 (c)). After the left actuator reaches its relaxation state, which crosses the centre dashed line, the remaining DC current is removed from the right actuator and the two thermal actuators are unlatched, as signified in Fig. 6-15 (d).

The device can be re-latched by following the reverse sequence of the latching steps. First, one of the two thermal actuators is actuated by a DC current, and held down along the substrate, as seen in Fig. 6-15 (c). Then, a DC current is applied to the other actuator. After both actuators are held down along the substrate, DC currents are removed and the two thermal actuators start to rotate in the opposite direction until the built-in mechanical limiters are engaged with each other and cease the rotation.

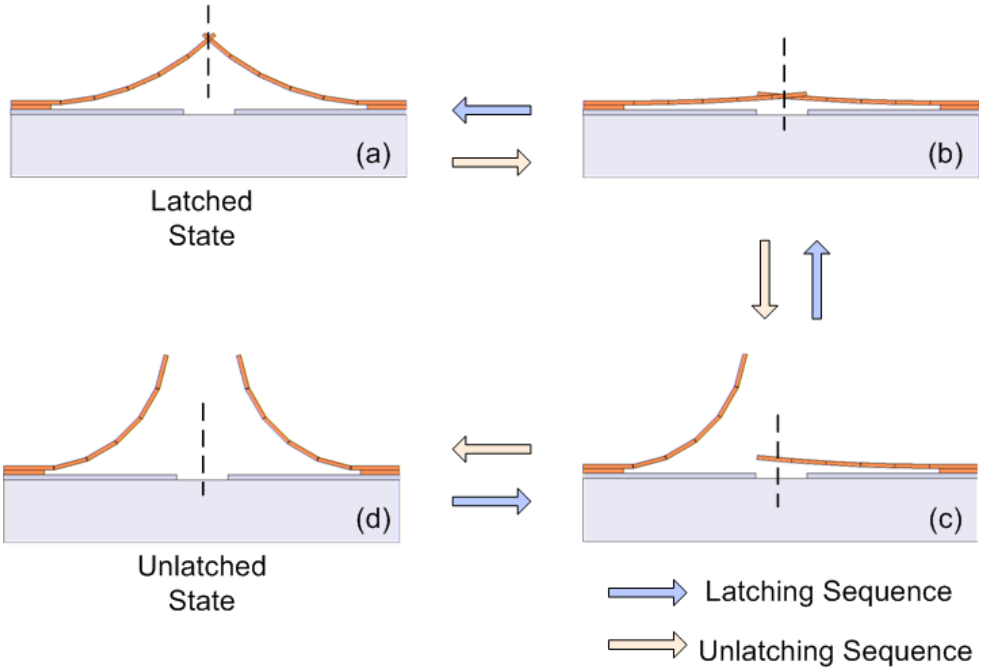

Figure 6-15: A schematic of the latching and unlatching sequencies of the proposed design.

6.5 Summary

In this chapter, a novel concept to construct reversible out-of-plane latching mechanisms with multi-stable states has been introduced. Thermal actuators with large out-of-plane deflections are employed in these newly developed latching mechanisms. The thermal plastic deformation assembly treatment and intrinsic stress mismatch are utilized to facilitate the thermal actuators to achieve large deflections. The unique latching mechanisms are applied not only for tunable filter applications, but also for applications such as switches and phase shifters, where a low power consumption is required and a moderate speed is acceptable.

Chapter 7

Conclusions

To conclude this thesis, the contributions of this research are summarized, a few suggestions are given for future research based on the results achieved in this research.

7.1 Contributions

The primary contributions of this research work are outlined as follows.

- The feasibility of employing MEMS actuators as tuning elements for micromachined filters is demonstrated. Both planar and 3D micromachined filters with embedded MEMS tuning elements are constructed to prove the concept. The test results of the micromachined ridge waveguide filter reveal a 200-MHz tuning range at a centre frequency of 23 GHz. When the micromachining process capability is fully extended, the simulation results indicate that the size of the micromachined ridge waveguide filter can be further decreased and the unloaded quality factor can be improved to as high as 600.

- A high quality factor tunable dielectric resonator bandpass filter with embedded MEMS tuning elements is proposed. The tunability of the novel design is achieved by using large deflected MEMS actuators to move the micromachined tuning disks to disturb the electromagnetic field of the dielectric resonators. The experimental filter has a centre frequency of 15.6 GHz with a relative bandwidth of 1%. The tuning range is between 15.6 GHz and 16 GHz, and the insertion loss is increased from 1.5 dB to 4.5 dB. The extracted

unloaded quality factor varies between 1638 and 421 when a single dielectric resonator is tuned from 15.62 GHz to 15.86 GHz.

- A novel approach to construct a compact tunable bandstop filter is also presented. MEMS tuning elements are monolithically integrated into a bandstop filter by surface micromachining techniques. The configuration of the microstrip line with zigzag slots etched in the ground plane is employed to form the bandstop filter. The MEMS tuning elements are built on the ground plane and above the slots. A single resonator is tuned over a bandwidth of 1.5 GHz by using the proposed approach. A three-pole tunable bandstop filter is tuned from 6.09 GHz to 5.575 GHz.

- A 4-mask surface micromachining process is developed to construct a compact tunable bandstop filter. The structure layer contains two metal films and one dielectric film that is sandwiched between the two metal films. This combination allows the RF circuit to separate from the DC biasing circuit, which simplifies the RF design. In addition, due to the stress mismatch between the metal and dielectric films, the MEMS actuators, fabricated in this process, obtain an initial deflection of a few hundred microns.

- Various out-of-plane latching mechanisms with multi-stable states are created to secure the tuned performance of the MEMS tunable filters. The fabrication processes of the latching mechanisms are all compatible with that of the MEMS tuning elements. The latching structures can be seamless integrated into MEMS tuning elements.

7.2 Future Work

A wide range of subjects are investigated in this research to advance tunable filter techniques using MEMS technologies. For researchers who want to further explore this field, a few suggestions are offered.

- Typically, RF MEMS tunable filters have a high insertion loss and low power handling capability, since the filters are often realized by planar filters. The ability to integrate MEMS tuning elements with dielectric resonators opens the door for the realization of MEMS-based high quality factor tunable filters. The feasibility of integrating MEMS

devices with other high quality factor and high power handling filters such as cavity filters can be investigated. With the assistance of advanced 3D micromachining technologies, the realization of monolithically integrated RF MEMS tunable filters with high quality factor, wide tuning range and high power handling capability is possible.

- Many commercially available MEMS fabrication processes are not designed for RF applications. The processes either use low resistivity silicon wafers as substrates or comprise structural materials such as polysilicon, which are very lossy at RF and microwave frequencies. This research introduces a surface micromachining process that is very attractive for RF applications. Besides tunable bandstop filters, many other RF devices such as switches and phase shifters can be fabricated by the same process. To further improve this process, aluminum films can be replaced by high conductivity metal films such as gold or copper. Developing a packaging technique for the devices, fabricated by this process, can be a challenging task since some devices have deflections as high as a few hundreds microns.

- Latching mechanisms are critical components for applications, where power consumption needs be limited. Various latching mechanisms have been created by using surface micromachining processes in this research. MEMS thermal actuators are limited for RF applications due to their high power consumption. These latching mechanism have broaden the applications of MEMS thermal actuators. RF switches and multi-bit phase shifters can be potentially realized by using these latching mechanisms incorporated with thermal actuators.

Appendix A

Fabrication Process of Tunable Bandstop Filters with Tri-layer MEMS Actuators

A.1 Introduction

This appendix presents the fabrication steps for tunable bandstop filters with tri-layer MEMS actuators in Chapter 5. The recipes for each step and problems encountered during the process development are detailed. The entire fabrication process is carried out in the clean room at the Centre for Integrated RF Engineering (CIRFE), University of Waterloo, Waterloo, ON.

A.2 Fabrication Steps

A.2.1 Wafer Preparation

The wafers used in this process are 25-mil thick with double-sided polished alumina wafers from CroosTech. Prior to the deposition of the gold layer on the front and back of the wafers, a cleaning process, RCA-1 (also known as Standard Clean-1, SC-1), is performed to remove the organic residue and films from the alumina wafers. The decontamination is based on the sequential oxidation steps in an H_2O:NH_4OH:H_2O_2 solution with a 5:1:1 ratio by volume. The

wafers are soaked in this solution at 70C for 15 min, rinsed in the DI water flow, and blown dry with N_2.

A.2.2 Microstrip Line and Ground Slots Patterning

After the RCA-1 cleaning, 1-μm gold is evaporated on the front and back of alumina wafers. 0.04-μm Cr is evaporated first as an adhesion layer. The gold layer can also be sputtered (Power = 300 W, Ar = 10 cc, Pressure = 0.78 mTorr, Rate = 0.03 μm/min) with a slightly higher stress.

Positive photoresist (Clariants, AZ3312) is used to pattern the front gold layer (microstrip line). The wafer is spin coated with AZ3312 at a spin speed of 300 rpm for 30 second, which gives about 1 μm thick coating. After the wafer is baked at 90 ^{0}C for 1 minute, it is exposed to a UV source of 41 mW/cm^2 for 12 second. After the post-exposure bake is performed at 110 ^{0}C for 1 minute, the wafer is soaked in the developer (Clariant's AZ MIF 300) for about 1 minute. A longer time might be required if the developer is old. Before the gold etching, the back of the wafer is blank coated with photoresist and baked at 110 ^{0}C for 1 minute to protect the gold layer during the gold etching for the front of the wafers. The etch rate for the gold etchant (Transene Inc.) is about 37A/sec with agitation. After the gold etching, the wafer is dipped into the Cr etchant (Transene Inc.) for about 10 sec to remove the 400 A Cr.

Up to now, the gold layer of the front of the wafers is patterned. Before the gold layer on the back is patterned, the wafer is soaked in stripper (Kwik strip) at 65 ^{0}C for 30 minutes to remove the photoresist on the frond and back of the wafers. Then, The same procedure is repeated for patterning the gold layer on the back of the wafers (ground slots). Since double side alignment is required for patterning the slots on the back, alignment markers are placed along the edge of the wafer and the corners to facilitate the alignment.

A.2.3 Sacrificial Layer Patterning

LOR 15A (Microchem Corp.) is used as the sacrificial layer. After the substrate is cleaned, (depending on the wafer condition, RCA-1 clean is recommended), the wafer is baked at 160 ^{0}C for 2 minutes for dehydration purpose. LOR 15A is spin-coated at a speed of 2000 rpm with an acceleration of 10 for 30 seconds to reach a thickness of 2 μm. Note that the spinner for

coating LOR 15A resist should not be the same as the one for photoresist since PG remover, not accetone is used to remove the LOR 15A from the spinner. After a uniform film is spin-coated on the wafer, it is baked on a vacuum hot plate at 160°C for 2 minutes, and then left in a convection oven at a temperature of 190 ^{0}C for 30 minutes. The baking temperature and time controls the undercut of the resist.

In the second spinner, the patterning resist (AZ 3312) is spin-coated at a speed of 3000 rpm for 30 seconds for a thickness of about 1 μm. After the resist is soft baked at 90°C on a vacuum hot plate for 1 minute, the wafer is exposed by UV light at 40 mW/cm2 for 12 seconds. The post-exposure baking step is 110°C for 1 minute. Both the LOR and AZ3312 are developed by using AZ 300 MIF. The wafer is dipped into the developer solution for 4 minutes (longer for an old developer solution). The next step is to remove the AZ 3312 layer in the reactive ion etching (RIE) system. The recipe used is: pressure = 50 mT, RF power = 100 W, O_2 = 50 sccm, and time = 150 seconds. An alternative recipe, with IPC power, can be used to accelerate the etching speed: pressure = 50 mT, ICP power = 250 W, RF power = 100 W, O_2 = 48 sccm, CF_4 = 2 sccm, and time = 40 seconds.

After removing the patterning resist, the wafer is dekteked to ensure that the LOR 15A is fully etched through and the bottom gold layer is exposed. It is also a good idea to take SEM pictures of the anchor's side wall profile. A positive side wall angle should be observed.

A.2.4 MEMS Structure Layer Patterning

The structure layer is a combination of 1-μm aluminum, 1-μm amorphous silicon, and another 2-μm aluminum. The aluminum layers are deposited by sputtering with the following settings: power = 50 W, Ar = 50 sccm, and a deposition rate = 180 Å/min. The amorphous silicon film is deposited by a plasma enhanced chemical vapor deposition (PECVD) system. The recipe developed by Chang requires that [128]: Pressure = 750 mT; RF power = 100 W; Temperature = 150 C; SiH4 flow = 10 sccm; Ar flow = 7 sccm; Time = 2000 seconds. The PECVD chamber should be cleaned before amorphous silicon deposition to ensure a good film quality.

The positive photoresist (AZ3312) is used to pattern the top Al layer. The same process parameters for patterning gold can be used for patterning the top Al layer except for the exposure time, since the Al film can reflect more light than the gold film. The exposure time

has to be adjusted in terms of the feature size, but 10 seconds is a good starting point. The Al layer is etched by using PAN etch solution. PAN stands for "Phosphoric - Acetic - Nitric". This etchant is mixed by Water:Phosperic Acid:Acetic Acid:Nitric Acid with a ratio of 2:16:1:1 by volume. When the PAN etch solution is heated precisely to 37°C, the etch rate is 250 nm/min. For an Al thickness of 2 μm, 8 minutes is required. A higher solution temperature can result in higher etch rate. The amorphous silicon film is etched by the RIE system with the following recipe: Pressure = 50 mT; RF power = 50 W; SF_6 = 30 sccm; and time = 150 sec for 1 μm thick film. The patterned top 2-μm Al layer is used as a mask for the amorphous silicon etching.

Besides the Al film, a gold film (sputtered and evaporated) is attempted for a more superior RF performance since gold has higher conductivity than Al. An adhesion layer is required for depositing the gold on the top of amorphous silicon. Evaporated Cr has been tried as an adhesion layer, but due to the diffusion of Cr in amorphours silicon, a new compound film is formed and cannot be etched by using the standard amorphous silicon etch recipe [129].

A.2.5 Final Release

After etching the second Al layer, the wafer is cleaned in a DI wafer for 5 minutes to remove the PAN etch solution. The chemicals for releasing the MEMS devices are the PG remover (Microchem Corp.), acetone, and isopropanol. The wafer is soaked in PG remover at 60 ^{0}C for 5 minutes. This step is repeated three times and each time a fresh PG remover is employed. Then the wafer is quickly immersed in acetone for 5 minutes. Up to now, it can be seen that the MEMS devices peels off from the substrate due to the stress. To remove the acetone and other organic material, the wafer is soaked in isopropanol three times and each time is 5 minutes. Finally, the wafer is left in a convectional oven for 15 minutes at 120 ^{0}C to dry out.

Bibliography

[1] I. Reines, C. Goldsmith, and C. Nordquist et al., "A low loss rf mems ku-band integrated switched filter bank", *IEEE Microwave and Wireless Component Letters*, vol. 15, pp. 74–76, 2005.

[2] A. Pothier, J. Orlianges, , and G. Zheng et al., "Low-loss 2-bit tunable bandpass filters using mems dc contact switches", *IEEE Trans. Microwave Theory Tech.*, vol. 53, pp. 354–360, 2005.

[3] K. Entesari and G. Rebeiz, "A 12 - 18-ghz three-pole rf mems tunable filter", *IEEE Trans. Microwave Theory Tech.*, vol. 53, pp. 2566–2571, 2005.

[4] J. Brank, J. Yao, and M. Eberly et al., "Rf mems-based tunable filters", *Int J RF and Microwave CAE.*, vol. 11, pp. 276–284, 2001.

[5] R. Borwick, P. Stupar, and J. DeNatale et al., "Variable mems capacitors implemented into rf filter systems", *IEEE Trans. Microwave Theory Tech.*, vol. 51, pp. 315–319, 2003.

[6] A. Vasani, *Design of Frequency Agile Circuits Using Barium Strontium Titanate Varactor*, Master Thesis, Department of Electrical Engineering, North Caroline State University, NC, US, 2006.

[7] S. Chen, K. Zaki, and R. West, "Tunable, temperature-compensated dielectric resonators and filters", *IEEE Trans. Microwave Theory Tech.*, vol. 38, pp. 1046–1052, 1990.

[8] G. Panaitov, R. Ott, and N. Klein, "Dielectric resonator with discrete electromechanical frequency tuning", *IEEE Trans. Microwave Theory Tech.*, vol. 53, pp. 3371–3377, 2005.

[9] T. Yun and K. Chang, "Piezoelectric-transducer-controlled tunable microwave circuits", *IEEE Trans. Microwave Theory Tech.*, vol. 50, pp. 1303–1310, 2002.

[10] J. Krupka, A. Abramowicz, and K. Derzakowski, "Magnetically tunable filters for cellular communication terminals", in *Proc. 34th European Microwave Conference*, pp. 1121–1124. 2004.

[11] C. S. Tsai, "Wideband tunable microwave devices using ferromagnetic film-gallium arsenide material structures", *Journal of Magnetism and Magnetic Materials*, vol. 209, pp. 10–14, 2000.

[12] R. Zhang, *Novel Planar Microstrip and Dielectric Resonator Filters*, PhD Thesis, Department of Electrical Engineering, University of Waterloo, ON, Canada, 2007.

[13] A. M. E. Safwat, F. Podevin, P. Ferrari, and A. Vilcot, "Tunable bandstop defected ground structure resonator using reconfigurable dumbbell-shaped coplanar waveguide", *IEEE Trans. Microwave Theory Tech.*, vol. 54, pp. 3559–3564, 2006.

[14] M. F. Karim, A. Q. Liu, A. Alphones, and A. B. Yu, "A tunable bandstop filter via the capacitance change of micromachined switches", *J. Micromech. Microeng.*, vol. 16, pp. 851–861, 2006.

[15] C. Siegel, V. Ziegler, U. Prechtel, B. Schonlinner, and H. Schumacher, "Very low complexity rf-mems technology for wide range tunable microwave filters", in *European Microwave Conference*, pp. 1–4. 2005.

[16] N. Jahedi, I. G. Foulds, and M. Parameswaran (Ash), "A novel bistable microelectromechanical mechanism utilizing socket joints", in *Conference on Electrical and Computer Engineering*, pp. 433–436. 2005.

[17] B. D. Jensen, M. B. Parkinson, and K. Kurabayashi et al., "Design and optimization of a full-compliant bistable micro-mechanism", in *ASME International Mechanical Engineering Congress and Exposition*, pp. 1–7. 2001.

[18] J. Qiu, J. H. Lang, and A. H. Slocum, "A curved-beam bistable mechanism", *J. of Microelectromechanical Systems*, vol. 13, pp. 137–146, 2004.

[19] X. Sun, K. R. Farmer, and W. N. Carr, "a bistable microrelay based on two-segment multimorph cantilever actuators", in *IEEE workshop on MEMS*, pp. 154–159. 1998.

[20] J. Oberhammer, M. Tang, A-Q. Liu, and G. Stemme, "Mechanically tri-stabl, true single-pole-double-throw (spdt) switches", *J. of Micromech. Microeng.*, vol. 16, pp. 2251–2258, 2006.

[21] R. R. A. Syms, H. Zhou, J. Stagg, and D. F. Moore, "Mems variable optical attentuator with a compound latch", *Microelectronic Engineering*, vol. 73-74, pp. 423–428, 2004.

[22] N. Sarkar, *MEMS actuation and self-assembly applied to RF and optical devices*, Master Thesis, Department of Electrical Engineering, University of Waterloo, ON, Canada, 2004.

[23] M. Ruan, J. Shen, and C. B. Wheeler, "Latching micromagnetic relays", *J. of Microelectromechanical Systems*, vol. 10, pp. 511–517, 2001.

[24] I-J. Cho, T. Song, S-H. Baek, and E. Yoon, "A low-voltage and low-power rf mems series and shunt switches actuated by combination of electromagnetic and electrostatic forces", *IEEE Trans. Microwave Theory Tech.*, vol. 53, pp. 2450–2457, 2005.

[25] "Efab access design guide v1.2", in *Microfabrica Inc., Burbank, CA*. 2005.

[26] Y. W. Yi and C. Liu, "Magnetic actuation of hinged microstructures", *J. of Microelectromechanical Systems*, vol. 8, pp. 10–17, 1999.

[27] R. R. A. Syms, "Surface tension powered self-assembly of 3-d micro-optomechanical structures", *J. of Microelectromechanical Systems*, vol. 8, pp. 448–455, 1999.

[28] J. Carter, A. Cowen, B. Hardy, R. Mahadevan, M. Stonefield, and S. Wilcenski, "Polymumps design handbooks v11", *MEMS CAP Inc.*, www.memsrus.com.

[29] S. Sarraf and L. Rulli, "Low cost, broadband tunable ferroelectric filters for jtrs cluster 5 applications", *Ferroelectrics*, vol. 342, pp. 129–140, 2006.

[30] J. Uher and W.J.R. Hoefer, "Tunable microwave and millimeter-wave bandpass filters", *IEEE Trans. Microwave Theory Tech.*, vol. 39, pp. 643–653, 1991.

[31] C. E. Saavedra, "Reconfigurable bandpass filter structure using an spdt mems switch", in *European Microwave Conference*, pp. 1–4. 4-6,Oct., 2005.

[32] E. Fourn, A. pothier, and C. Champeaux et al., "Mems switchable interdigital coplanar filter", *IEEE Trans. Microwave Theory Tech.*, vol. 51, pp. 320–324, 2003.

[33] C. Hall, R. Luetzelschwab, R. Streeter, and J. VanPatten, "A 25 watt rf mem-tuned vhf banpass filter", in *IEEE MTT-S Digest*, pp. 503–506. 2003.

[34] J. Park, H. Kim, Y. Kwon, and Y. Kim, "Tunable millimeter-wave filters using a coplanar waveguide and micromachined variable capacitors", *J. of Micromech. Microeng.*, vol. 11, pp. 706–712, 2001.

[35] J. Kim, S. Lee, and J. Park et al., "Digitally frequency-controllable dual-band wlan filters using micromachined frequency-tuning elements", in *IEEE MEMS*, pp. 158–161. 2006.

[36] R. Streeter, C. Hall, R. Wood, and R. Mahadevan, "Vhf high-power tunable rf bandpass filter using microelectromechanical(mem)microrelays", *Int J RF and Microwave CAE.*, vol. 11, pp. 261–275, 2001.

[37] K. Entesari and G. Rebeiz, "A differential 4-bit 6.5-10 ghz rf mems tunable filter", *IEEE Trans. Microwave Theory Tech.*, vol. 53, pp. 1103–1110, 2005.

[38] E. Prophet, j. Musolf, and B. Zuck et al., "Highly-selective electronically-tunable cryogenic filters using monolithic, discretely-switchable mems capacitor arrays", *IEEE Trans. Applied Superconductivity*, vol. 15, pp. 956–959, 2005.

[39] A. Abbaspour-Tamijani, L. Dussopt, and G. Rebeiz, "Miniature and tunable filters using mems capacitors", *IEEE Trans. Microwave Theory Tech.*, vol. 51, pp. 1878–1885, 2003.

[40] H. Kim, J. Park, Y. Kim, and Y. Kwon, "Low-loss and compact v-band mems-based analog tunable bandpass filters", *IEEE Microwave and Wireless Components Letters*, vol. 12, pp. 432–434, 2002.

[41] G. L. Matthaei, "Narrow-band fixed-tuned and tunable bandpass filters with zig-zag hairpin-comb resonators", *IEEE Trans. Microwave Theory Tech.*, vol. 51, pp. 1214–1219, 2003.

[42] A. Brown and G. Rebeiz, "Micromachined micropackaged filter banks and tunable bandpass filters", in *Wireless Communication Conference*, pp. 193–197. 1997.

[43] A. Brown and G. Rebeiz, "A varactor-tuned rf filter", *IEEE Trans. Microwave Theory Tech.*, vol. 48, pp. 1157–1160, 2000.

[44] J. Xu, X. Liang, and K. Shamsaifar, "Full wave analysis and design of rf tunable filters", in *IEEE MTT-S Digest*, pp. 1449–1452. 2000.

[45] B. Kim and S. Yun, "Varactor-tuned combline bandpass filter using step-impedance microstrip lines", *IEEE Trans. Microwave Theory Tech.*, vol. 52, pp. 1279–1283, 2004.

[46] B. Kapilevich and R. Lukjanets, "Designing tunable resonators and filters with constant bandwidth", in *www.rfdesign.com*. 2001.

[47] B. Virdee, "Effective technique for electronically tuning a dielectric resonator", *Electronics Letters*, vol. 33, pp. 301–302, 1997.

[48] B. Virdee, A. Virdee, and I. Trinogga, "Novel invasive electronic tuning of dielectric resonators", in *IEEE MTT-S Digest*, pp. 51–54. 2003.

[49] J. Nath, D. Ghosh, and J. Maria et al., "An electronically tunable microstrip bandpass filter using thin-film barium-strontium-titanate", *IEEE Trans. Microwave Theory Tech.*, vol. 53, pp. 2707–2712, 2005.

[50] A. Tombak, J. Maria, and F. Ayguavives et al., "Voltage-controlled rf filters employing thin-film barium-strontium-titanate tunable capacitors", *IEEE Trans. Microwave Theory Tech.*, vol. 51, pp. 462–467, 2003.

[51] Paratek Microwave Inc., "Thin film electronically tunable pre-selectors for software defined radios", *Microwave Journal*, pp. 138–144, 2004.

[52] D. Kuylenstierna, A. Vorobiew, and S. Gevorgian, "40 ghz lumped element tunable bandpass filters with transmission zeros based on thin bst film varactors", in *Topic Meeting on Silicon Monolithic Integrated Circuits in RF Systems*, pp. 342–345. 2006.

[53] T. Shen, K. Zaki, and C. Wang, "Tunable dielectric resonators with dielectric tuning disks", *IEEE Trans. Microwave Theory Tech.*, vol. 48, pp. 2439–2445, 2000.

[54] M. Al-Ahmad, R. Matz, and P. Russer, "Piezoelectric tuned ltcc bandpass filters", in *IEEE MTT-S Digest*, pp. 764–767. 2006.

[55] S. Hontsu, K. Iguchi, and K. Agemura et al., "Mechanical tuning of superconducting lumped element filter", *IEEE Trans. Applied Superconductivity*, vol. 15, pp. 972–975, 2005.

[56] A. Takacs, D. Neculoiu, and D. Vasilache et al., "Tunable mems filters for millimeter wave applications", in *International Semiconductor Conference*, pp. 115–118. 2006.

[57] L-H. Hsieh and K. Chang, "Piezoelectric transducer tuned bandstop filter", *Electronics Letters*, vol. 38, pp. 970–971, 2002.

[58] B. Carey-Smith and P. A. Warr, "Broadband configurable bandstop filter with composite tuning mechanism", *Electronics Letters*, vol. 40, pp. 1–2, 2004.

[59] C. S. Tsai, G. Qiu, and H. Gao et al., "Tunable wideband microwave band-stop and band-pass filters yig/ggg-gaas layer structures", *IEEE Trans. Magnetics.*, vol. 41, pp. 3568–3570, 2005.

[60] H. J. Yoo, S.-H. Tseng, and C. S. Tsai, "Magnetic/semiconductor multilayer flip-chip-type tunable bandstop filter", in *Electronic Components and Technology Conference*, pp. 1681–1683. 2003.

[61] V.S. Liau, T. Wong, W. Stacey, S. Ali, and E. Schloemann, "Tunable bandstop filter based on epitaxial fe film on gaas", in *IEEE MTT-S Digest*, pp. 957–960. 1991.

[62] S. Lucyszyn and I. D. Robertson, "Mmic tunable active notch filter", *Electronics Letters*, vol. 32, pp. 980–981, 1996.

[63] F. Giannini, E. Limiti, G. Orengo, and P. Sanzi, "High q gyrator-based monolithic active tunable bandstop filter", *IEE Proc. Circuits Devices Syst.*, vol. 145, pp. 243–246, 1998.

[64] R. A. Baki and M. N. El-Gamal, "A 1.5v multigigahertz cmos tunable image reject notch filter", in *International Conference on Microelectronics*, pp. 144–147. 2002.

[65] D. Auffray and J. L. Lacombe, "Electronically tunable bandstop filter", in *IEEE MTT-S Digest*, pp. 439–442. 1988.

[66] I. C. Hunter and J. D. Rhodes, "Electronically tunable microwave bandstop filters", *IEEE Trans. Microwave Theory Tech.*, vol. MTT-30, pp. 1361–1367, 1982.

[67] J. D. Park, Y. J. Sung, S. H. Lee, and Y. S. Kim, "Tunable bandstop filters using defected ground structure with active devices", in *Asia-pacific Microwave Conference*, pp. 1–4. 2005.

[68] B. Carey-Smith and P. A. Warr, "Distortion mechanisms in varactor diode-tuned microwave filters", *IEEE Trans. Microwave Theory Tech.*, vol. 54, pp. 3492–3500, 2006.

[69] G. Zheng and J. Papapolymerou, "Monolithic reconfigurable bandstop filter using rf mems switches", *Int J RF and Microwave CAE*, vol. 14, pp. 373–382, 2004.

[70] R. R. A. Syms, E. M. Yeatman, V. M. Bright, and G. M. Whitesides, "Surface tension powered self-assembly of microstructures-the state-of-the-art", *J. of Microelectromechanical Systems*, vol. 12, pp. 387–417, 2003.

[71] T. Gomm, L. L. Howell, and R. H. Selfridge, "In-plane linear displacement bistable microrelay", *J. of Microelectromechanical Systems*, vol. 12, pp. 257–264, 2002.

[72] M. S. Baker and L. L. Howell, "On-chip actuation of an in-plane compliant bistable micromechanism", *J. of Microelectromechanical Systems*, vol. 11, pp. 566–573, 2002.

[73] P. G. Opdahl, B. D. Jensen, and L. L. Howell, "An investigation into compliant bistable mechanisms", in *ASME Design Engineering Technical Conference*, pp. 1–10. 1998.

[74] I-H. Hwang, Y-S. Shim, H-N. Kwon, and J-H. Lee, "Design and experimental characterization of the chevron-type bi-stable actuator for optical switch applications", in *IEEE/LEOS International Conference on Optical MEMS*, pp. 135–136. 2003.

[75] W-C. Chen, C. Lee, C-Y. Wu, and W. Fang, "A new latched 2x2 optical switch using bi-directional movable electrothermal h-beam actuators", *Sensors and Actuators*, vol. 123-124, pp. 563–569, 2005.

[76] W. Noell, P. A. Clerc, F. Duport, C. Marxer, and N. De Rooij, "Novel process-insensitive latchable 2x2 optical cross connector for single and multimode optical mems filter switches", in *IEEE/LEOS International Conference on Optical MEMS*, pp. 49–50. 2003.

[77] N. D. Masters and L. L. Howell, "A self-retracting fully compliant bistable micromechanism", *J. of Microelectromechanical Systems*, vol. 12, pp. 273–280, 2003.

[78] D. L. Wilcox and L. L. Howell, "Fully compliant tensural bistable micromechanisms", *J. of Microelectromechanical Systems*, vol. 14, pp. 1223–1235, 2005.

[79] K. German, J. Kubby, and J. Chen et al., "Optical mems platform for low cost on-chip integration of planar light circuits and optical switching", in *Optoelectronic Integration on Silicon, Proc. of SPIE vol. 5357*, G. E. Jabbour D. J. Robbins, Ed., pp. 87–95. 2004.

[80] R. W. Moseley, E. M. Yeatman, and A. S. Holmes et al., "Laterally actuated, low voltage, 3-port rf mems switch", in *IEEE MEMS 2006, Istanbul, Turkey*, pp. 878–881. Jan. 22-26, 2006.

[81] Vivek Agrawal, "A latching mems relay for dc and rf applications", in *Proceedings of the 50th IEEE Holm Conference on Electrical Contacts and the 22nd International Conference on Electrical Contacts*, pp. 222–225. 2004.

[82] R. R. A. Syms, H. Zhou, and P. Boyle, "Mechanical stability of a latching mems variable optical attentuator", *J. of Microelectromechanical Systems*, vol. 14, pp. 529–538, 2005.

[83] R. R. A. Syms, H. Zhou, and Stagg, "Robust latching mems translation stages for micro-optical systems", *J. of Micromech. Microeng.*, vol. 14, pp. 667–674, 2004.

[84] R. R. A. Syms, H. Zhou, and Stagg, "Micro-opto-electro-mechanical systems alignment stages with vernier latch mechanisms", *J. of Opt. A: Pure Appl. Opt.*, vol. 8, pp. 305–312, 2006.

[85] A. Unamuno and D. Uttamchandani, "Mems variable optical attenuator with vernier latching mechanism", *IEEE Photonics Technology Letters*, vol. 18, pp. 88–90, 2006.

[86] G. D. Gray, E. M. Propher, L. Zhu, and P. A. Kohl, "Magnetically bistable actuator part. fabrication and performance", *Sensors and Actuators*, vol. 119, pp. 502–511, 2005.

[87] J. Sutanto, P. J. Hesketh, and Y. H. Berthelot, "Design, microfabrication and testing of a cmos compatible bistable electromagnetic microvavle with latching/unlatching mechanism on a single wafer", *J. of Micromech. Microeng*, vol. 16, pp. 266–275, 2006.

[88] Ph. Robert, D. Saias, and C. Billard et al., "Integrated rf-mems switch based on a combination of thermal and electrostatic actuation", in *Transducers '03, the 12th International Conference on Solid State Sensors, Actuators and Microsystems*, pp. 1714–1717. 2003.

[89] Y. Choi, K. Kim, and M. G. Allen, "A magnetically actuated, electrostatically clamped high current mems switch", in *2001 ASME International Mechanical Engineering Congress and Exposition*, pp. 1–5. Nov. 11-16, 2001.

[90] L. P. Katehi, J. F. Harvey, and E. Brown, "Mems and si micromachined circuits for high-frequency applications", *IEEE Trans. Microwave Theory Tech.*, vol. 50, pp. 858–866, 2002.

[91] J. Bouchaud and H. Wicht, "Rf mems not only for telecom! interesting opportunities in higher frequency applications", in *MSTNews, international newsletter on microsystem and MEMS*, pp. 43–44. September, 2003.

[92] R. F. Drayton, S. P. Pacheco, J-G. Yook, and L. P. Katehi, "Micromachined filters on synthesized substrates", in *IEEE MTT-S Microwave Symposium Digest*, pp. 1185–1188. 1998.

[93] G. M. Rebeiz, L. P. Katehi, T. M. Weller, C-Y. Chi, and S. V. Robertson, "Micromachined membrane filters for microwave and millimeter-wave applications (invited article)", *Int. J. Microwave Millimeter-Wave CAE*, vol. 7, pp. 149–166, 1997.

[94] K-Y. Park, J-C. Lee, and et al. J-H. Kim, "A new three-dimensional 30 ghz bandpass filter using liga micromachined process", *Microwave and Optical Technology Letters*, vol. 30, pp. 199–201, August, 2001.

[95] R. T. Chen, E. R. Brown, and C. A. Band, "A compact low-loss ka-band filter using three-dimensional micromachined integrated coax", in *17th IEEE International Conference on MEMS*, pp. 801–804. 2004.

[96] X. Gong, A. Margomenos, and B. Liu et al., "Precision fabrication techniques and analysis on high-q evanescent-mode resonators and filters of different geometries", *IEEE Trans. Microwave Theory Tech.*, vol. 52, pp. 2557–2566, 2004.

[97] W. D. Yan, R. Mansour, and A. Khajepour, "A mems variable capacitor with high self-resonance frequency", in *34th European Microwave Conference*, pp. 1153–1156. 2004.

[98] S. B. Cohn, "Design considerations for high-power microwave filters", *IRE Trans. Microwave Theory Tech.*, pp. 149–153, 1959.

[99] C. Ernst, V. Postoyalko, and N. G. Khan, "Relationship between group delay and stored energy in microwave filters", *IEEE Trans. Microwave Theory Tech.*, vol. 49, pp. 192–196, 2001.

[100] R. J. Cameron, C. M. Kudsia, and R. R. Mansour, *Microwave Filters for Communication Systems: Fundamentals, Design, and Applications*, John Wiley and Son Inc., 2007.

[101] G. M. Rebeiz, *RF MEMS: Theory, Design and Technology*, John Wiley and Son Inc., 2003.

[102] K. Entesari and G.M. Rebeiz, "A differential 4-bit 6.5Íc10-ghz rf mems tunable filter", *IEEE Trans. Microwave Theory Tech.*, vol. 53, pp. 1103–1110, 2005.

[103] I.C. Hunter and J.D. Rhodes, "Electronically tunable microwave bandpass filters", *IEEE Trans. Microwave Theory Tech.*, vol. 30, pp. 1354–1360, 1982.

[104] M. Makimoto and M. Sagawa, "Varactor tuned bandpass filters using microstrip line ring resonators", in *IEEE MTT-S Microwave Symposium Digest*, pp. 411–414. May, 2001.

[105] S-W Chen, K.A. Zaki, and R.G. West, "Tunable, temperature-compensated dielectric resonators and filters", *IEEE Trans. Microwave Theory Tech.*, vol. 38, pp. 1046–1052, 1990.

[106] G. L. Matthaei, L. Young, and E. M. T. Jones, *Microwave Filters, Impedance Matching Networks, and Coupling Structures*, New York: McGraw-Hill, ch. 17, 1964.

[107] M. Daneshmand, R. Mansour, and N. Sarkar, "Rf mems waveguide switch", in *IEEE MTT-S Microwave Symposium Digest*, pp. 589–592. June, 2004.

[108] A. Geisberger, N. Sarkar, M. Ellis, and G. Skidomre, "Modeling electrothermal plastic deformation self-assembly", *Nanotech*, vol. 1, pp. 482–485, Feb. 2003.

[109] D. Kajfez, *Q Factor*, Oxford, MS: Vector Forum, 1994.

[110] A. E. Atia and A. E. Williams, "Narrow-bandpass waveguide filters", *IEEE Trans. Microwave Theory Tech.*, vol. MTT-20, pp. 258–265, 1972.

[111] P. Laforge, *Tunable microwave bandpass filters*, Masters degree, Department of Electrical Engineering, University of Waterloo, ON, Canada, 2003.

[112] S. Chang and S. Sivoththaman, "Development of a low temperature mems process with a pecvd amorphous silicon structural layer", *J. Micromech. Microeng*, vol. 16, pp. 1307–1313, 2006.

[113] L. Zhu, B. Taylor, and P. Jarmuszewski, "Rf lumped-notch filter design for fcc compliance testing of wireless radio modems", *RF Design*, vol. 19, pp. 36–45, 1996.

[114] C. Rauscher, "Varactor-tuned active notch filter with low passband noise and signal distortion", *IEEE Trans. Microwave Theory Tech.*, vol. 49, pp. 1431–1437, 2001.

[115] D. R. Jachowski, "Compact, frequency-agile, absorptive bandstop filter", in *IEEE MTT-S Microwave Symposium Digest*, pp. 513–516. June, 2005.

[116] R. Zhang and R. Mansour, "Novel tunable lowpass filters using folded slots etched in the ground plane", in *IEEE MTT-S Microwave Symposium Digest*, pp. 775–778. June, 2005.

[117] K. Entesari and G. Reibeiz, "A differential 4-bit 6.5-10 ghz rf mems tunable filter", *IEEE Trans. Microwave Theory Tech.*, vol. 53, pp. 1103–1110, 2005.

[118] M. F. Karim, A. Q. Liu, A. B. Yu, and A. Alphones, "Micromachined tunable bandstop filters for wireless sensor networks", in *IEEE sensors*, pp. 151–154. October, 2005.

[119] D-J. Woo, T-K. Lee, and J-W. Lee et al., "Novel u-slot and v-slot dgss for bandstop filter with improved q factor", *IEEE Trans. Microwave Theory Tech.*, vol. 54, pp. 2840–2847, 2006.

[120] A. Oz and G. K. Fedder, "Cmos-compatible rf-mems tunable capacitor", in *IEEE Radio Frequency Integrated Circuits Symposium*, pp. 611–614. 2003.

[121] M. C. Wu, "Micromachining for optical and optoelectronic systems", *Proceedings of the IEEE*, vol. 85, pp. 1833–1856, 1997.

[122] D. J. Dagel, O. B. Spahn, and J. J. Allen et al., "Out-of-plane, rotary micromirrors for reconfigurable phonic applications", in *MOEMS and Miniaturized Systems III, Proc. of SPIE vol. 4983*, J. H. Smith, Ed., pp. 114–121. 2003.

[123] L. Li, J. Zawadzka, and D. Uttamchandani, "Integrated self-assembling and holding technique applied to a 3-d mems variable optical attenuator", *J. of Microelectromechanical Systems*, vol. 13, pp. 83–90, 2004.

[124] M. R. Whitley, M. Kranz, R. Kesmodel, and S. Burgett, "Latching shock sensors for health monitoring and quality control", in *MEMS/MOEMS Components and Their Applications, Proc. of SPIE vol. 5717*, A. K. Henning, Ed., pp. 185–194. 2004.

[125] R. Prasad, K-F. Bohringer, and N. C. MacDonald, "Design, fabrication and characterization of single crystal silicon latching snap fasterers for micro assembly", in *1995 ASME International Mechanical Engineering Congress and Exposition*, pp. 1–5. Nov. 1995.

[126] R. R. A. Syms, "Improving yield, accuracy and complexity in surface tension self-assembled moems", *Sensors and Actuators*, vol. A88, pp. 273–283, 2001.

[127] W. D. Yan and R. Mansour, "Tunable dielectric resonator bandpass filter with embedded mems tuning elements", *IEEE Trans. Microwave Theory Tech.*, vol. 55, pp. 154–160, 2007.

[128] S. Chang, *Design, Optimization and Fabrication of Amorphous Silicon Tunable RF MEMS Inductors and Transformers*, Ph.D. Thesis, Department of Electrical Engineering, University of Waterloo, ON, Canada, 2006.

[129] S. K. Persheyev, P. R. Drapacz, M. J. Rose, and A. G. Fitzgerald, "Diffusion of chromium in thin hydrogenated amorphous silicon films", *Semiconductors*, vol. 38, pp. 344–346, 2004.